

DISSERTATION

EMERGENT TOPOLOGICAL PHENOMENA IN LOW-DIMENSIONAL SYSTEMS INDUCED BY  
GAUGE POTENTIALS

Submitted by

Aidan Winblad

Department of Physics

In partial fulfillment of the requirements

For the Degree of Doctor of Philosophy

Colorado State University

Fort Collins, Colorado

Spring 2025

Doctoral Committee:

Advisor: Hua Chen

Richard Eykholt

Martin Gelfand

Olivier Pinaud

Copyright by Aidan Winblad 2025

All Rights Reserved

## ABSTRACT

### EMERGENT TOPOLOGICAL PHENOMENA IN LOW-DIMENSIONAL SYSTEMS INDUCED BY GAUGE POTENTIALS

In this dissertation we discuss how gauge potentials can be used as a key ingredient for inducing topological phase transitions in condensed matter systems, such as conductors, insulators, and superconductors. The first chapter covers some important background physics: Maxwell's equations, gauge invariance, minimal coupling, and Peierls phase, etc. It then presents a review of how one can realize Majorana fermions (MFs) in superconductors and their importance to topological quantum computing. In the end of chapter 1, we give an overview of the basics of Landau levels (LLs) and their relation to the Chern number. Chapter 2 presents a theoretical proposal for inducing topological phase transitions that allow for MFs to be hosted and rotated along the corners of a hollow equilateral triangle, which can serve as a basic building block for topological quantum logic gates. This provides a potential new avenue for achieving a topological quantum computation where a network of interconnected triangular islands allows for braiding of MFs. Chapter 3 we show using Floquet theory and high-frequency expansion, that oblique incident, circularly polarized light can give rise to spectral features analogous to Landau levels in the quantum Hall effect (QHE), where the effective magnetic field is related to the electric field of the laser light. Outside of having the electric field as a useful parameter for achieving a QHE device, this finding enables us to explore non-equilibrium systems exhibiting topological phenomena in the absence of spatial periodicity. Chapter 4 concludes and discusses further implications of the work in this dissertation.

## ACKNOWLEDGEMENTS

## DEDICATION

*I would like to dedicate this dissertation to my dog, Zeta.*

# TABLE OF CONTENTS

ABSTRACT . . . . .	ii
ACKNOWLEDGEMENTS . . . . .	iii
DEDICATION . . . . .	iv
LIST OF TABLES . . . . .	vii
LIST OF FIGURES . . . . .	viii
Chapter 1      Introduction . . . . .	1
1.1          Maxwell's equations and gauge transformations . . . . .	1
1.2          Minimal coupling and canonical momentum . . . . .	2
1.3          Peierls phase in tight-binding models . . . . .	5
1.4          Majorana fermions and topological superconductors . . . . .	7
1.4.1      Kitaev chain . . . . .	8
1.4.2      Half-quantum vortices in $p$ -wave superconductors . . . . .	11
1.4.3      Braiding . . . . .	14
1.4.4      T-junction qubit . . . . .	16
1.4.5      Effective $p$ -wave superconductors . . . . .	17
1.5          Landau levels and quantum Hall effect . . . . .	19
1.5.1      Landau levels in condensed matter systems . . . . .	19
1.5.2      Quantized Hall conductivity and Chern number . . . . .	22
1.5.3      Laughlin pump on a Hall cylinder . . . . .	23
Chapter 2      Superconducting Triangular Islands as a Platform for Manipulating Majorana Zero Modes . . . . .	25
2.1          Context . . . . .	25
2.2          Paper abstract . . . . .	25
2.3          Research article . . . . .	26
2.4          Supplemental material . . . . .	36
Chapter 3      Landau Level-Like Topological Floquet Hamiltonians . . . . .	49
3.1          Introduction . . . . .	49
3.2          Floquet Landau level-like bands in Dirac systems . . . . .	50
3.3          Floquet Landau level-like bands in 2DEG systems . . . . .	53
3.4          Conclusion . . . . .	56
Chapter 4      Conclusion . . . . .	60
Appendices . . . . .	62
Appendix Chapter A      Superconducting Triangular Islands . . . . .	62
A.1          Kitaev chain . . . . .	62
A.2          Gauge potential and gauge invariance . . . . .	77
A.3          Kitaev Triangle and Peierls substitution . . . . .	79

A.4	Effective $p$ -wave superconductors . . . . .	81
Appendix Chapter B	Landau Level-Like Topological Floquet Hamiltonians . . . . .	86
B.1	Quantum harmonic oscillator . . . . .	86
B.2	Dirac equation in the presence of a magnetic field . . . . .	89
B.3	General framework of Floquet theory . . . . .	91
B.4	High Frequency (Van Vleck) expansion from degenerate perturbation theory . . . . .	97
B.4.1	Non-uniform circularly polarized light on Dirac . . . . .	99
B.4.2	Non-uniform circularly polarized light on 2DEG . . . . .	101
B.5	Tight-binding model Dirac . . . . .	103
B.6	Tight-binding model 2DEG . . . . .	107
B.7	Chern number of Landau levels . . . . .	111
Bibliography	. . . . .	120

## LIST OF TABLES



## LIST OF FIGURES

1.1	The top chain represents the system in a trivial topology where each complex fermion $c_j = \frac{1}{2}(a_j + ib_j)$ is a linear combination of intraconnected MFs. The bottom chain represents the system in a non-trivial topology where each complex fermion $\tilde{c}_j = \frac{1}{2}(a_j + ib_{j+1})$ is a linear combination of interconnected MFs, leaving the non-localized complex fermion $f = \frac{1}{2}(a_0 + ib_N)$ , and thus leaving one MF located at each end of the chain. . . . .	9
1.2	The order phase $\varphi$ and angle $\alpha$ of $\mathbf{d}$ rotate by $\pi$ : $(\varphi, \mathbf{d}) \rightarrow (\varphi + \pi, -\mathbf{d})$ . The order parameter $\theta$ maps to itself, $(0, 2\pi)$ , under simultaneous change of both $\mathbf{d}$ and $\varphi$ : $\theta = \varphi + \alpha$ . . . . .	13
1.3	Two vortices in an elementary braid exchange. . . . .	14
1.4	Braid group relation for $T_i T_{i+1} T_i = T_{i+1} T_i T_{i+1}$ . . . . .	15
1.5	(Left) Braiding two MFs on a T-junction. (Right) Ladder junction schematic for hosting and braiding multiple MFs. . . . .	16
2.1	Schematics of two triangle structures proposed in this work. (a) Three-site Kitaev triangle with bond-dependent Peierls phases. (b) Hollow triangular island with a uniform vector potential. . . . .	28
2.2	(a) Evolution of the eigenvalues of the 3-site Kitaev triangle along the closed parameter path for $\phi$ on the three edges. (b) MZM wavefunctions at different points of the parameter path. Clockwise from the upper left panel: $\phi_1 \rightarrow \frac{1}{2}(\phi_1 + \phi_2) \rightarrow \phi_2 \rightarrow \phi_3$ . . . . .	31
2.3	(a) Schematic illustration of a finite-width ( $W = 3$ here) ribbon based on the triangular lattice in the presence of a vector potential $\mathbf{A} = A(-\sin\varphi\hat{\mathbf{x}} + \cos\varphi\hat{\mathbf{y}})$ . (b) Topological phase diagram for a $W = 1$ triangular chain obtained by superimposing the $\mathcal{M}_{b,t}(A, \mu)$ ( $b$ -bottom edge, $t$ -top edges) plots of 1D chains with $\mathbf{A} = A\hat{\mathbf{y}}$ (bottom edge) and $\mathbf{A} = A(\frac{\sqrt{3}}{2}\hat{\mathbf{x}} + \frac{1}{2}\hat{\mathbf{y}})$ (top edges). Color scheme: black— $[\mathcal{M}_b, \mathcal{M}_t] = [1, 1]$ , yellow— $[-1, -1]$ , purple— $[-1, 1]$ , orange— $[1, -1]$ (not present in this case) (b) Near-gap BdG eigen-energies vs $A$ for a finite triangle with edge length $L = 50$ , $W = 1$ , and $\mu = 1.6$ . $t = \Delta = 1$ in all calculations. . . . .	32
2.4	(a) Topological phase diagram for a $W = 1$ triangle by superimposing the $\mathcal{M}_{b,r,l}(A, \varphi)$ plots of 1D chains ( $b$ -bottom, $r$ -right, $l$ -left, $\mu = 1.1$ ). $\varphi_{r,l}$ are equal to $\varphi_b + \pi/3$ and $\varphi_b - \pi/3$ , respectively. The colors are coded by which edges have non-trivial topology. For example, Black— $[\mathcal{M}_b, \mathcal{M}_r, \mathcal{M}_l] = [1, 1, 1]$ means all edges are trivial. The behavior depicted in panels (b-f) is representative of that when $A$ is in the range of $(2.25, 2.5)$ , for which the $\mathcal{M} = -1$ phase “crawls” through the three edges counter-clockwise as $\varphi$ increases. (b) Spectral flow of a triangle with $W = 1$ , $L = 50$ , $\mu = 1.1$ , and $A = 2.35$ with increasing $\varphi$ . (c-f) BdG eigenfunction $ \Psi ^2$ summed over the two zero modes at $\varphi = 0, \frac{\pi}{12}, \frac{\pi}{6}$ , and $\frac{\pi}{3}$ , respectively. The bottom edge is parallel with $\hat{\mathbf{x}}$ in the coordinates illustrated in Fig. 2.3 (a). . . . .	33

2.5	Representative steps for braiding four MZM in four triangles sharing corners. (a) Initialization of four MZM $\gamma_1, \gamma_2, \gamma_3, \gamma_4$ . All three edges of the bottom-middle and the top triangles are in the trivial phase by e.g. controlling the chemical potential. The bottom-left and bottom-right triangles have $\varphi = 0$ so that their bottom edges are nontrivial. (b) Moving $\gamma_3$ by “switching on” the middle triangle by changing the chemical potential under a fixed vector potential at $\varphi = \frac{\pi}{6}$ , and then turning on the top triangle with similar means except $\varphi = 0$ . (c) Transporting $\gamma_2$ to the right triangle through rotating the vector potential in the middle triangle counterclockwise by $\pi/6$ . (d) Moving $\gamma_3$ to the left triangle by “switching off” the top triangle followed by the middle triangle. . . . .	35
2.6	(a) Topological phase diagram for a $W = 3$ hollow triangle obtained by overlapping the $\mathcal{M}_{b,t}(A, \mu)$ plots of 1D chains with $\mathbf{A} = A\hat{\mathbf{y}}$ and $\mathbf{A} = A(\frac{\sqrt{3}}{2}\hat{\mathbf{x}} + \frac{1}{2}\hat{\mathbf{y}})$ . Color scheme: purple— $[\mathcal{M}_b, \mathcal{M}_t] = [1, 1]$ , yellow— $[\mathcal{M}_b, \mathcal{M}_t] = [-1, -1]$ , red— $[\mathcal{M}_b, \mathcal{M}_t] = [-1, 1]$ , orange— $[\mathcal{M}_b, \mathcal{M}_t] = [1, -1]$ (b) Near-gap BdG eigen-energies vs $A$ for a finite triangle with edge length $L = 80$ , $W = 3$ , and $\mu = 1.6$ . . . . .	45
2.7	(a) Topological phase diagram for three $W = 3$ ribbons corresponding to the three edges of a hollow triangle. ( $\mu = 1.6$ in all panels.) (b) Minimum of the bulk gaps of the three ribbons plotted on the $(A, \varphi)$ plane. (c) Spectral flow of a hollow triangle with $W = 3$ , $L = 80$ , and the parameter path given in Eq. (2.37). (d-g) BdG eigenfunction $ \Psi ^2$ summed over the two zero modes at $\varphi = 0, \frac{\pi}{6}, \frac{\pi}{3}, \frac{\pi}{2}$ , respectively. . . . .	47
2.8	(a) Spectral flow for the critical step of swapping $\gamma_2$ and $\gamma_3$ in the example of Fig. 5 in the main text, calculated using four corner-sharing triangles of $W = 1$ and $L = 50$ , with $\mu = 1.6$ and $A = 2.6$ . Vector potential for the middle triangle in the bottom row can rotate according to $\mathbf{A} = A(-\sin\varphi\hat{\mathbf{x}} + \cos\varphi\hat{\mathbf{y}})$ from $\varphi = \frac{\pi}{6}$ to $\frac{\pi}{3}$ , while the other three have fixed $\varphi = 0$ . (b)-(g) BdG eigenfunction $ \Psi ^2$ summed over the four zero modes at equally-spaced points along the rotation path. The black arrow indicates the direction of the vector potential for the bottom middle triangle. . . . .	48
3.1	Schematic of two oblique (forward and backward) and one normally incident light on graphene or a 2DEG substrate with high refractive index material on top. Oblique lasers have polarization in $y$ -axis and travel in $xz$ -plane and normally incident laser has polarization in the $x$ -axis and travel in $yz$ -plane. With beam width large enough to cover the device fully. . . . .	51
3.2	Effective magnetic field (cyan) and first quasienergy (red) as a function of photon energy for various refractive materials: vacuum (triangles), germanium (squares), and Al-composite metamaterial (circles). . . . .	57
3.3	Effective magnetic field (cyan) and first quasienergy (red) as a function of photon energy for 2DEGs for various refractive materials: vacuum (triangles) scaled by a factor of 50, germanium (squares) scaled by a factor of 10, and Al-composite metamaterials. The 2DEG materials used are (a) GaAs and (b) InSb. . . . .	58
B.1	Unit cell for dirac system with gauge potential with translation symmetry in the $y$ – $axis$ described by Eq. (B.82). . . . .	104



# Chapter 1

## Introduction

In this chapter we will review some key concepts that will be frequently be encountered in the remaining chapters. We will review Maxwell's equations, gauge invariance, minimal coupling, and Peierls phase. Then we move onto MFs in superconductors and their connection to topological quantum computing, and how one can achieve them in a lab setting. Finally, we will cover the basics of LLs and their relation to the Chern number.

### 1.1 Maxwell's equations and gauge transformations

Here we give an overview of Maxwell's equations in relation to gauge potentials and transformations. The electric and magnetic fields,  $\mathbf{E}$  and  $\mathbf{B}$ , respectively, are physical observables. While different scalar potentials  $V$  and gauge potentials  $\mathbf{A}$  are not directly observable, they produce the same electric and magnetic fields, reflecting the principle of gauge invariance. The following derivation can be found in many textbooks, we follow the following textbook [1]. To show this, we start with Maxwell's equations and aim to rewrite them in terms of potential fields.

$$\nabla \cdot \mathbf{E} = \frac{1}{\epsilon_0} \rho, \quad (1.1)$$

$$\nabla \cdot \mathbf{B} = 0, \quad (1.2)$$

$$\nabla \times \mathbf{E} = -\partial_t \mathbf{B}, \quad (1.3)$$

$$\nabla \times \mathbf{B} = \mu_0 \mathbf{J} + \mu_0 \epsilon_0 \partial_t \mathbf{E}, \quad (1.4)$$

One can write Maxwell's equations as a function of potentials,  $V$  and  $\mathbf{A}$ . Recall the magnetic field,  $\mathbf{B} = \nabla \times \mathbf{A}$ , and electric field,  $\mathbf{E} = -\nabla V - \partial_t \mathbf{A}$ . Eq. (1.1) and (1.4) provide the most informa-

tion, which become

$$\frac{1}{\epsilon_0} \rho = -\nabla^2 V - \partial_t \nabla \cdot \mathbf{A}, \quad (1.5)$$

$$-\mu_0 \mathbf{J} = \nabla^2 \mathbf{A} - \mu_0 \epsilon_0 \partial_t^2 \mathbf{A} - \nabla (\nabla \cdot \mathbf{A} + \mu_0 \epsilon_0 \partial_t V). \quad (1.6)$$

We now transition to gauge transformations. Suppose  $\mathbf{A}' = \mathbf{A} + \boldsymbol{\alpha}$  and  $V' = V + \beta$ . Both vector potentials give the same magnetic field,

$$\mathbf{B} = \nabla \times \mathbf{A} = \nabla \times \mathbf{A}' = \nabla \times (\mathbf{A} + \boldsymbol{\alpha}),$$

which leads to  $\boldsymbol{\alpha} = \nabla \lambda$ . The two potentials should also give the same electric field,

$$\mathbf{E} = -\nabla V - \partial_t \mathbf{A} = -\nabla V' - \partial_t \mathbf{A}',$$

then  $\beta = -\partial_t \lambda + k(t)$  and

$$\mathbf{A}' = \mathbf{A} + \nabla \lambda \quad (1.7)$$

$$V' = V - \partial_t \lambda + k(t), \quad (1.8)$$

which is a general gauge transformation of potentials. Thus  $V$  and  $\mathbf{A}$  are gauge invariant. This allows one to leverage gauge invariance to conveniently determine both scalar and gauge potentials for a system.

## 1.2 Minimal coupling and canonical momentum

With gauge potentials and their invariance shown we next review how a gauge potential couples to the momentum operator, also known as minimal coupling. Minimal coupling comes from the following substitution

$$-i\hbar\nabla \rightarrow -i\hbar\nabla - q\mathbf{A}, \quad (1.9)$$

which can be derived from the canonical momentum operator when a charged particle is present in a gauge potential. In this case, minimal coupling is defined by a field coupling orbital and potential only, ignoring higher order multipole moments. This also allows the system to have a local gauge invariance under U(1) transformations, i.e.  $\mathbf{A} \rightarrow \mathbf{A} + \nabla\lambda$  [2].

Next, we derive the canonical momentum operator. Starting with the Lagrangian for charged particle in a scalar and gauge potential,

$$\begin{aligned} \mathcal{L} &= T - U \\ \mathcal{L} &= \frac{1}{2}m\dot{\mathbf{r}}^2 - qV + q\dot{\mathbf{r}} \cdot \mathbf{A}(\mathbf{r}, t), \end{aligned} \quad (1.10)$$

where  $T = \frac{1}{2}m\dot{\mathbf{r}}^2$  and  $U = qV - q\dot{\mathbf{r}} \cdot \mathbf{A}(\mathbf{r}, t)$ . Recalling

$$\begin{aligned} \mathbf{p}_{\text{can}} &= \frac{\partial \mathcal{L}}{\partial \dot{\mathbf{r}}} \\ \mathbf{p}_{\text{can}} &= \mathbf{p}_{\text{kin}} + q\mathbf{A}. \end{aligned} \quad (1.11)$$

With the canonical momentum defined, the Hamiltonian becomes

$$\begin{aligned} \mathcal{H} &= \mathbf{p}_{\text{can}} \cdot \dot{\mathbf{r}} - \mathcal{L} \\ \mathcal{H} &= \frac{1}{2m}(\mathbf{p}_{\text{can}} - q\mathbf{A})^2 + qV. \end{aligned} \quad (1.12)$$

Thus, a charged particle in the presence of a gauge potential has the following minimal coupling,  $i\hbar\nabla - q\mathbf{A}$ .

We will now show the Hamiltonian is gauge invariant. One can show it with a scalar potential in the Hamiltonian, but we do not since it is irrelevant for our purposes. Suppose  $\mathcal{H}|\psi\rangle = \epsilon|\psi\rangle$  and  $\mathbf{A}' = \mathbf{A} + \nabla\lambda$ , then the Hamiltonian acting on the wavevector is

$$\mathcal{H}|\psi\rangle = \frac{1}{2m}(\hat{\mathbf{p}} - q\mathbf{A}' + q\nabla\lambda)^2|\psi\rangle = \epsilon|\psi\rangle. \quad (1.13)$$

We assert

$$\mathcal{H}'|\psi'\rangle = \frac{1}{2m}(\hat{\mathbf{p}} - q\mathbf{A} - q\nabla\lambda)^2|\psi'\rangle = \epsilon|\psi'\rangle. \quad (1.14)$$

Let  $|\psi'\rangle = U|\psi\rangle$ , where  $U$  is a unitary operator such that  $U^\dagger U = \hat{\mathbf{1}}$ . Position and momentum expectation values should be the same under both gauge choices. Starting with position operator we have

$$\langle\psi'|\hat{\mathbf{r}}|\psi'\rangle = \langle\psi|U^\dagger\hat{\mathbf{r}}U|\psi\rangle = \langle\psi|\hat{\mathbf{r}}|\psi\rangle \quad (1.15)$$

which gives the following useful commutation relation is  $[\hat{\mathbf{r}}, U] = 0$ , which can be extrapolated to  $[\mathbf{A}(\mathbf{r}), U] = 0$ . With the momentum operator we find

$$\langle\psi'|\hat{\mathbf{p}} - q\mathbf{A}'|\psi'\rangle = \langle\psi|U^\dagger(\hat{\mathbf{p}} - q\mathbf{A}')U|\psi\rangle = \langle\psi|\hat{\mathbf{p}} - q\mathbf{A}|\psi\rangle \quad (1.16)$$

that gives the following commutation relation  $[\hat{\mathbf{p}}, U] = -i\hbar\partial_{\hat{\mathbf{r}}}U = q\nabla\lambda U$ . This leads us to find  $U = \exp[iq\lambda/\hbar]$ . The gauged Hamiltonian is related to the original basis by

$$\mathcal{H}'|\psi'\rangle = U\epsilon|\psi\rangle. \quad (1.17)$$

We see the local phase of the wavefunction is changed but it still represents the same energy shown by

$$\begin{aligned} \langle\psi'|\mathcal{H}'|\psi'\rangle &= \langle\psi|U^\dagger U\epsilon|\psi\rangle = \epsilon, \\ \langle\psi|\mathcal{H}|\psi\rangle &= \langle\psi|\epsilon|\psi\rangle = \epsilon. \end{aligned} \quad (1.18)$$

Thus,  $U^\dagger \mathcal{H}' U = \mathcal{H}$ , and gauge invariance is shown [3].

### 1.3 Peierls phase in tight-binding models

When working with condensed matter systems we often either work with free particles using Schrodinger's or Dirac's equation or tight-binding models describing how much energy is needed for a particle to “hop” from one lattice to the next. In tight-binding models there is typically no momentum term to use minimal coupling to introduce the gauge potential, but we can find a basis transformation that is equivalent. A few different names this can go by include: Aharonov-Bohm effect, Berry phase, geometric phase, or Peierls phase. There are a few ways to derive Peierls phase and we will use the differential geometry approach. We follow the following textbook reference [2].

Before, we showed minimal coupling and now we would like to express it in terms of a covariant derivative

$$D_\mu = \partial_\mu - i A_\mu. \quad (1.19)$$



Let us now envision how a wavefunction will evolve in the presence of a gauge potential field. Using the covariant derivative with parallel transport along curves we can obtain an expression for the phase accumulation on the wave function. The covariant derivative should vanish if it has been parallel transported along the curve  $\mathcal{C}$  defined by points  $x$  and  $x' = x + v t$ . The expression is as follows  $\nabla_\nu s \rightarrow t v^\mu D_\mu s_{x(t)} = 0$ . This turns out to be a first order ordinary differential equation

$$\dot{s}_{x(t)} - i \dot{x}^\mu(t) A_{x(t),\mu} s_{x(t)} = 0$$

with the following solution

$$s_{x(t)} = s_{x(0)} \exp \left[ i \int_{\mathcal{C}} dx^\mu A_{x(t'),\mu} \right] \quad (1.20)$$

and in general we can rewrite it as the following expression  $\psi(t) = \psi(0) \exp \left[ \frac{iq}{\hbar} \int_{\mathcal{C}} \mathbf{A}(\mathbf{r}) \cdot d\mathbf{l} \right]$ .

Given the following tight-binding Hamiltonian

$$\mathcal{H}_t = -t \sum_{\langle j,l \rangle} c_j^\dagger c_l + h.c., \quad (1.21)$$

a gauge potential is applied to the system making the following Peierls phase transform, a unitary transform, to its creation/annihilation operators

$$c_j^\dagger c_l \rightarrow c_j^\dagger c_l \exp \left[ \frac{iq}{\hbar} \int_{\mathbf{r}_j}^{\mathbf{r}_l} \mathbf{A} \cdot d\mathbf{l} \right]. \quad (1.22)$$

The Hamiltonian in the new basis takes the following form

$$\mathcal{H}_t = \sum_{\langle j,l \rangle} -t_{j,l} c_j^\dagger c_l + h.c., \quad (1.23)$$

where  $t_{j,l} = t \exp \left[ \frac{iq}{\hbar} \int_{\mathbf{r}_j}^{\mathbf{r}_l} \mathbf{A} \cdot d\mathbf{l} \right]$ .

## 1.4 Majorana fermions and topological superconductors

We discuss here MFs and their connection to topological superconductors and the properties that can be exploited for topological quantum computing. There are three types of fermions: Dirac, Weyl, and Majorana. Fermions are particles that follow Fermi-Dirac statistics and the Pauli exclusion principle and have half-integer spin (spin  $1/2$ ,  $3/2$ , etc.). In 1926, both Enrico Fermi and Paul Dirac derived Fermi-Dirac statistics, independently of one another. Dirac's equation led to the derivation of a (complex) wavefunction solution for spin-half fermions that have mass and charge, and an antiparticle, coined as the positron. A few years later, Hermann Weyl derived from Dirac's equation a simplified solution for describing massless fermions. Then, in 1937 Ettore Majorana hypothesized from Dirac's equation a (real) wavefunction solution that showed that these fermions were both particle and antiparticle and neutrally charged.

Examples of observed fermions include electrons, neutrinos, neutrons, and protons. The Standard Model does allow for neutrinos to potentially be MFs. The MAJORANA project: neutrinoless double beta decay, is one experiment for detecting neutrino MFs and has yielded negative results thus far. The particle physics community has yet to find either Weyl or MFs in experiments. There are, however, avenues for pursuing them as quasiparticles in condensed matter systems. For example, in 2011 Weyl fermions were theorized to be in topological semimetals then quickly observed as quasiparticles by 2015 in TaAs semimetals using angle-resolved photoemission spectroscopy (ARPES) [4–6]. Since 2001 it has been hypothesized that MFs can be found on  $p$ -wave superconductors in pairs of 2 and non-localized in half-quantum vortices and at the ends of wires.

In conventional superconductors there are Cooper pairs that make up the supercurrent. These Cooper pairs are made up of two electrons (or holes) with opposite spin and momenta caused by the electron-phonon interaction. A Bogoliubov quasiparticle is the first excited state of a Cooper pair condensate. This is when an electron and hole with opposite momenta become paired. When the systems chemical potential allows the electron and hole bands to cross one another in the Brillouin zone. The superconducting order parameter,  $\Delta$ , dictates the type of

spin coupling for the Bogoliubov quasiparticles. For example, superconductors that are  $s$ -wave, pair electrons and holes with opposite spin. While  $p$ -wave, pairs electrons and holes that compose spin-triplets. In a  $p$ -wave superconductor, if the Bogoliubov quasiparticle is a zero-energy excitation, then it can be written as a highly non-localized Majorana zero mode (MZM). MZMs come in pairs due to particle-hole symmetry of the system.

Here are a few reasons why MFs are highly sought after. MFs are dictated by non-Abelian exchange statistics, which allows for building a universal quantum computer. Another perk of non-trivial topological superconductors, is the ability to protect MFs from local perturbations, also known as fault-tolerant. This reduces the error qubits can acquire when performing a braiding operation. The next few subsections will review these properties of MFs in topological superconductors.

### 1.4.1 Kitaev chain

We now review the Kitaev chain, a realization of MZMs, or MFs, on a 1D spinless  $p$ -wave superconductor. The derivation can be found in the following reference [7]. Originally, Kitaev's proposal was to design a topological quantum storage device. However, a Kitaev chain can be used for more than storage; it is a key building block in constructing topological quantum logic gates.

Start with a 1D spinless  $p$ -wave superconductor tight-binding Hamiltonian

$$\mathcal{H} = \sum_j^{N-1} (-tc_j^\dagger c_{j+1} + \Delta c_j c_{j+1} + h.c.) - \sum_j^N \mu c_j^\dagger c_j, \quad (1.24)$$

where  $t$  is hopping amplitude,  $\Delta = |\Delta|$  is the superconducting order parameter,  $\mu$  is chemical potential, and  $c^\dagger(c)$  is the creation (annihilation) operator for a complex fermion. We use the following MF basis transformation, where  $c_j^\dagger = \frac{1}{2}(a_j - ib_j)$ ,  $\{a_j^\dagger, a_{j'}\} = \{a_j, a_{j'}\} = 2\delta_{j,j'}$  since they are MFs, and  $\{a_j, b_{j'}\} = 0$ . The Hamiltonian becomes

$$\mathcal{H} = \frac{i}{2} \sum_j (-\mu a_j b_j + (t + \Delta) b_j a_{j+1} + (-t + \Delta) a_j b_{j+1}). \quad (1.25)$$

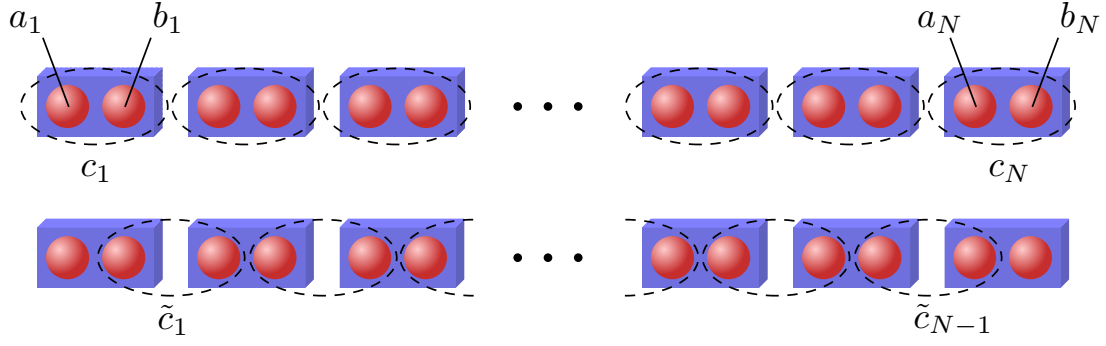


**Figure 1.1:** The top chain represents the system in a trivial topology where each complex fermion  $c_j = \frac{1}{2}(a_j + ib_j)$  is a linear combination of intraconnected MFs. The bottom chain represents the system in a non-trivial topology where each complex fermion  $\tilde{c}_j = \frac{1}{2}(a_j + ib_{j+1})$  is a linear combination of interconnected MFs, leaving the non-localized complex fermion  $f = \frac{1}{2}(a_0 + ib_N)$ , and thus leaving one MF located at each end of the chain.

In the trivial topology phase, there are no MFs,  $\mu \neq 0$  and  $t = \Delta = 0$ ,

$$\mathcal{H} = -\mu \frac{1}{2} \sum_j a_j b_j. \quad (1.26)$$

For non-trivial topology phase, there are MFs present,  $\mu = 0$ , and  $t = \Delta > 0$ ,

$$\mathcal{H} = it \sum_j b_j a_{j+1}. \quad (1.27)$$

Notice terms  $a_1$  and  $b_N$  are missing in the non-trivial topology Hamiltonian. We define the non-localized zero energy mode present in the system as the following fermionic operator,  $f = \frac{1}{2}(a_1 + ib_N)$ . This state is composed of two well separated MZMs. Figure 1.1 shows the wire in both topological phases. A quick note on terminology, sometimes non-trivial topology is referred to as the topological phase, for the purposes of this dissertation we will use the former option.

Slightly outside the Kitaev limit, a non-trivial topology persists if  $|\mu| < 2t$  and  $t = |\Delta| > 0$ . Due to bulk-edge correspondence, MZMs are localized at the interface between trivial and non-trivial segments. To formalize this, we calculate the topological invariant, known as the Majorana number. While calculating the Majorana number is straight forward enough, its proof on

the other hand is not, this can be found in App. A.1. To compute the Majorana number, we perform a MF basis transformation on the Hamiltonian,  $A = -iU\mathcal{H}U^\dagger$ , then take the sign of the Pfaffian,

$$\mathcal{M} = \text{sgn}[\text{Pf}(A)]. \quad (1.28)$$

If the system has translational symmetry in  $x$  and  $y$ , the Hamiltonian can be transformed into momentum space. Using the symmetry condition  $\epsilon(-k) = -\epsilon(k)$ , we find that for any given  $k$ , there are equal numbers of positive and negative eigenvalues. The Majorana number then simplifies to

$$\mathcal{M} = \begin{cases} \text{sgn}[\text{Pf}(A_{k=0})\text{Pf}(A_{k=\pi})], & \text{if } L \text{ is even,} \\ \text{sgn}[\text{Pf}(A_{k=0})], & \text{if } L \text{ is odd,} \end{cases} \quad (1.29)$$

where  $L$  is the number of lattice sites. Within the Kitaev limit, if  $|\mu| < 2t$ , then  $\mathcal{M} = -1$ , and if  $|\mu| > 2t$ , then  $\mathcal{M} = 1$ . If one section of the material exhibits non-trivial topology while adjacent sections remain trivial, MZMs will localize at interfaces of differing topological numbers. This phenomena is a direct consequence of bulk-edge correspondence.

Now that we have a way to distinguish topological states, we must consider the size of the systems band gap and robustness. When  $|\mu| = 2t$ , the system reaches a critical point where the band gap opens and closes, making this region of parameter space undesirable. The band gap is too small, allowing even minor local perturbations to reopen or close the gap, which compromises the stability and information of the MZMs. By tuning the chemical potential further from these critical points, the band gap enhances, increasing robustness against local perturbations (providing greater topological protection).

But what are local perturbations and how do they contribute to error? There are two common types of error in quantum computers: classical and phase. Classical error flips the qubit

state,  $|1\rangle \rightarrow |0\rangle$  and vice versa. Phase error changes the sign of the occupied state,  $|1\rangle \rightarrow -|1\rangle$ , relative to the unoccupied state  $|0\rangle$ .

To rid the system of classical error we envision the following. In a superconductor we can imagine an electron hopping from one site to another as two classical errors occurring simultaneously. If our fermionic qubit state has its information distributed non-locally with a band gap medium between its MZMs, then the possibility of an electron hopping between the two MZMs becomes exponentially small with separation distance. Simply put, the error must affect both MZMs at the same time but with large separation makes it highly unlikely to occur.

Phase error can be represented as  $c_j^\dagger c_j$ , leading to different electron configurations acquiring different phases over time. Majorana operators as defined earlier give the following phase error operator  $c_j^\dagger c_j = \frac{1}{2}(1 + i a_j b_j)$ . This would require the highly non-localized MZMs to share the same site to induce a phase error. In summary, non-trivial topology makes MZMs difficult to couple together due to their separation and a large finite band gap prevents excitations from occurring. [7].

### 1.4.2 Half-quantum vortices in $p$ -wave superconductors

We now transition to Ivanov's derivation of MFs and introduce *braiding* for its topological quantum computing applications. It was proposed by Read and Green that the Pfaffian quantum Hall state derived by Moore and Read belongs to the same topological class as the Bardeen-Cooper-Schrieffer (BCS) pairing state. Ivanov later verified this was the case for a BCS-paired state, demonstrating that the Pfaffian state exhibits non-Abelian statistics in the presence of half-quantum vortices. Since  $p$ -wave superconductors share this topological structure, they also support non-Abelian statistics. To answer this, we need to understand how the superconducting order parameter acts under different pairing potentials composed of singlet or triplet states. The following reference was used for this section.

The superconducting order parameter, also called order parameter or pairing potential for short, tells us the correlation between two fermionic operators in a superconductor and re-

quires the state to be antisymmetric. The order parameter is made up of a spatial and spin component, with symmetry constraints dictating their relationship. In spin-singlet pairing, the spin component is antisymmetric, limiting the spatial component to be symmetric. This occurs in  $s$ - and  $d$ -wave superconductors. In spin-triplet pairing, the spin component is symmetric, limiting the spatial component to be antisymmetric. This occurs in  $p$ - and  $f$ -wave superconductors.

In terms of Pauli matrices, the order parameter can be expressed as

$$\Delta(\mathbf{k}) = (\Delta_0(\mathbf{k}) + \mathbf{d}(\mathbf{k}) \cdot \boldsymbol{\sigma}) i\sigma_y, \quad (1.30)$$

where the antisymmetric condition  $\Delta(\mathbf{k}) = \Delta^T(-\mathbf{k})$  encodes  $\Delta_0(\mathbf{k})$  as spin-singlet components and  $\mathbf{d}(\mathbf{k})$  as spin-triplet components, and  $\sigma_y$  maintains the overall antisymmetric nature of the matrix. The direction vector  $\mathbf{d}$  must be a three dimensional vector to ensure the three spin configurations  $|\uparrow\uparrow\rangle$ ,  $|\uparrow\downarrow\rangle + |\downarrow\uparrow\rangle$ , and  $|\downarrow\downarrow\rangle$ . The parity of the spatial component determines  $\Delta(\mathbf{k})$ . Even-parity is of even powers in momentum, proportional to even spherical harmonics. Odd-parity is of odd powers in momentum, proportional to odd spherical harmonics. For example, in  $s$ -wave superconductors  $l = 0$ , the spherical harmonic  $Y_{0,0}$  is constant and has no momentum dependence and takes the form  $\Delta_s(\mathbf{k}) = i\Delta_0\sigma_y$ . In contrast, for  $p$ -wave superconductors  $l = 1$ , the spherical harmonic  $Y_{1,\pm 1} \propto k_x \pm ik_y$ , leading to linear dependence in momentum. This leads to the order parameter  $\Delta_p(\mathbf{k}) = i\Delta(\mathbf{d} \cdot \boldsymbol{\sigma})(k_x + ik_y)\sigma_y$ . This shows symmetry of the superconducting state determines the structure of  $\Delta(\mathbf{k})$  and how it influences the physical properties of the system.

In Ivanov's proof, a slightly different basis for the triplet-pairing order parameter is used

$$\Delta(\mathbf{k}) = \Delta e^{i\varphi} [d_x\sigma_0 + id_y\sigma_z + d_z\sigma_x] (k_x + ik_y), \quad (1.31)$$

and follows the antisymmetric definition  $\Delta(\mathbf{k}) = -\Delta^T(-\mathbf{k})$ . For a half-quantum vortex to exist, we must allow  $\mathbf{d}$  to rotate in 3D or in a plane. Additionally, the order parameter maps to it-

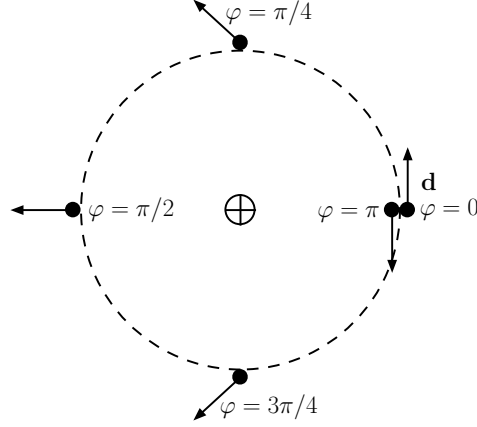


**Figure 1.2:** The order phase  $\varphi$  and angle  $\alpha$  of  $\mathbf{d}$  rotate by  $\pi$ :  $(\varphi, \mathbf{d}) \rightarrow (\varphi + \pi, -\mathbf{d})$ . The order parameter  $\theta$  maps to itself,  $(0, 2\pi)$ , under simultaneous change of both  $\mathbf{d}$  and  $\varphi$ :  $\theta = \varphi + \alpha$ .

self, which requires the change of sign of  $\mathbf{d}$  and shift in the phase  $\varphi$  by  $\pi$ , simultaneously. This mapping is  $(\varphi, \mathbf{d}) \mapsto (\varphi + \pi, -\mathbf{d})$  and can be seen in Figure 1.2.

We now reduce to a 2D superconductor, this forces  $\mathbf{d}$  to point and rotate in the x-y plane and removes the coupling of spin-up and -down fermions from the order parameter. The order parameter can then be written in polar coordinates

$$\begin{aligned} \Delta(\mathbf{k}, r, \theta) &= \Delta(r) e^{i\varphi} \begin{bmatrix} e^{i\alpha} & 0 \\ 0 & e^{-i\alpha} \end{bmatrix} (k_x + i k_y) \\ &= \Delta(r) \begin{bmatrix} e^{i\theta} & 0 \\ 0 & 1 \end{bmatrix} (k_x + i k_y), \end{aligned} \quad (1.32)$$

where  $\alpha$  is the angle of  $\mathbf{d}$ , remembering its simultaneous change w.r.t.  $\varphi$ . We see that the spin-up fermions have a vortex while the spin-down do not have a vortex (and thus no low energy states). The Hamiltonian for spin-up or spinful fermions can now be described by

$$\mathcal{H} = \int d^2\mathbf{r} \left[ -\Psi^\dagger \left( \frac{\nabla^2}{2m} + \epsilon_F \right) \Psi + \Psi^\dagger \left[ e^{i\theta} \Delta(r) * (\partial_x + i\partial_y) \right] \Psi^\dagger + h.c. \right], \quad (1.33)$$



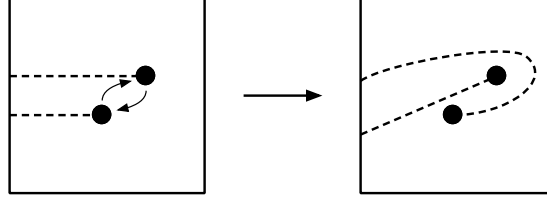


**Figure 1.3:** Two vortices in an elementary braid exchange.

where  $*$  is the symmetrized product  $[A * B = (AB + BA)/2]$ . One can diagonalize the Hamiltonian using the quasiparticle operator  $\gamma^\dagger = u\Psi^\dagger + v\Psi$ . The creation annihilation of the same fermion is related by the parameters  $u$  and  $v$ , causing the energy eigenstates to be symmetric about zero-energy, restricting  $\gamma^\dagger(E) = \gamma(E)$ . The spinful nature eliminates the spin degree of freedom and shows the creation and annihilation operators are coupled due to superconductivity, making MFs possible through self-conjugacy.

### 1.4.3 Braiding

To speak on braiding it is important to start with gauge symmetry. Under  $U(1)$  gauge transformation, if the superconducting gap is shifted by  $\phi$ , it is the same as rotating the creation annihilation operator by half the shift. Thus,  $\Psi_\alpha \mapsto e^{i\phi/2}\Psi_\alpha$ , which leads to the MF operator weights transforming as  $(u, v) \mapsto (ue^{i\phi/2}, v^{-i\phi/2})$ . We can see with a change of superconducting order parameter by  $2\pi$  the MF changes sign,  $\gamma \mapsto -\gamma$  [8].

This change of sign is important in braiding transformations since it allows for non-Abelian exchange statistics. We can circumvent a global phase by introducing branch cuts for the vortices to cross, causing a  $2\pi$  phase change in the MFs. Vortices can be exchanged as described in Figure 1.3, with a "bird's eye" view. We can define the braiding operators as the following

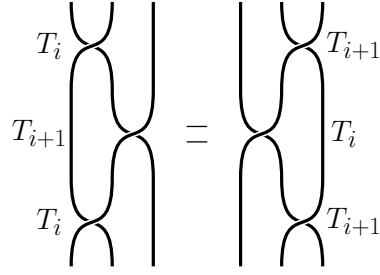


**Figure 1.4:** Braid group relation for  $T_i T_{i+1} T_i = T_{i+1} T_i T_{i+1}$ .

$$T_i : \begin{cases} \gamma_i \mapsto \gamma_{i+1} \\ \gamma_{i+1} \mapsto -\gamma_i \\ \gamma_j \mapsto \gamma_j \quad \text{for } j \neq i \text{ and } j \neq i+1. \end{cases} \quad (1.34)$$

This leads to the following braiding relations

$$\begin{aligned} T_i T_j &= T_j T_i, \quad |i - j| > 1, \\ T_i T_j T_i &= T_j T_i T_j, \quad |i - j| = 1. \end{aligned} \quad (1.35)$$

Figure 1.4 demonstrates three neighboring vortices with braiding statistics having two means of achieving the same braiding exchange. One can write the braiding operators in terms of fermionic operators with the following

$$\tau(T_i) = \exp\left(\frac{\pi}{4} \gamma_{i+1} \gamma_i\right) = \frac{1}{\sqrt{2}} (1 + \gamma_{i+1} \gamma_i). \quad (1.36)$$

This can be further carried out for any number of MFs and builds a set of braiding operators for that system.

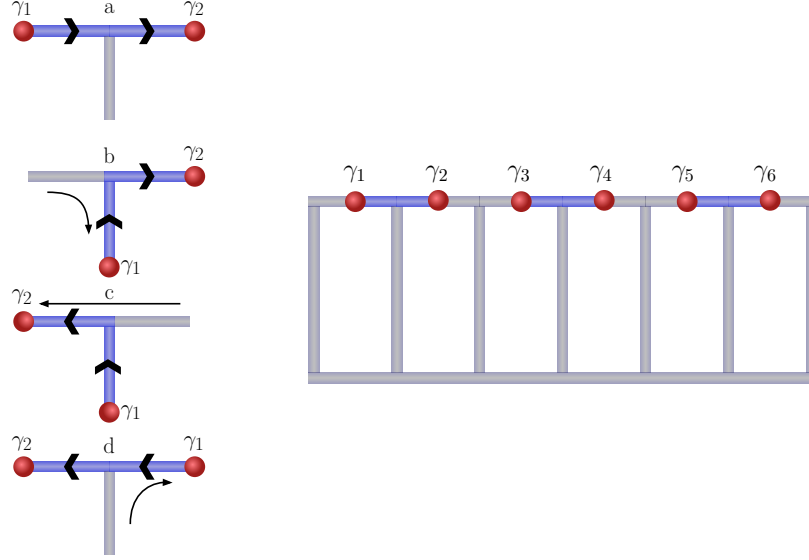


**Figure 1.5:** (Left) Braiding two MFs on a T-junction. (Right) Ladder junction schematic for hosting and braiding multiple MFs.

#### 1.4.4 T-junction qubit

The simplest qubit theorized for braiding MFs is on 1D wires connected in a T-junction, which can be extrapolated to a ladder junction for  $2n$  MFs. In the T-junction we define the quasi-1D Hamiltonian

$$\mathcal{H} = -\mu \sum_j c_j^\dagger c_j - \sum_j \left( t c_j^\dagger c_{j+1} + |\Delta| e^{i\phi} c_j c_{j+1} + h.c. \right), \quad (1.37)$$

where  $c_j = e^{-i\phi/2}(\gamma_{j+1,1} + i\gamma_{j,2})/2$ . We additionally have to define the pairing as  $|\Delta| e^{i\phi} c_j c_{j+1}$  such that the site indices have the following definitions

- Increase moving  $\rightarrow$  /  $\uparrow$  in the horizontal/vertical wires:  $\phi = 0$ ,
- Decrease moving  $\leftarrow$  /  $\downarrow$  in the horizontal/vertical wires:  $\phi = \pi$ .

The braiding of two MFs in a T-junction is achieved by adiabatically tuning the voltage gate, or chemical potential, of the wires which can be seen in Figure 1.5. Then, extrapolate to a ladder junction as shown in Figure 1.5 [9]. While this approach is simple in theory and being seriously

pursued, it is difficult to build, manipulate, and read experimentally. Another difficulty for these wires is due to not having any truly  $p$ -wave superconductors, currently they need to be built from heterostructures to make an effective  $p$ -wave superconductor.

### 1.4.5 Effective $p$ -wave superconductors

There are several ways to build an effective  $p$ -wave superconductor. One example, which we will follow in this section, is provided by Sau et. al. [10] where a zinc-blende semiconductor quantum well grown along the (100) direction is considered. We start with the relevant non-interacting Hamiltonian

$$\mathcal{H}_0 = \sum_{\mathbf{k}} c_{\mathbf{k}}^\dagger \left[ \frac{\hbar^2 k^2}{2m} - \mu + \alpha(\sigma^x k_y - \sigma^y k_x) \right] c_{\mathbf{k}} \quad (1.38)$$

where  $m$  is the effective mass,  $\mu$  is the chemical potential,  $\alpha$  is the Rashba spin-orbit coupling strength, and  $\sigma^i$  are the Pauli matrices that act on the spin degrees of freedom in  $c_{\mathbf{k}}$ , and  $\hbar = 1$  throughout.

Next, introduce a ferromagnetic insulator to induce a Zeeman effect. The ferromagnetic insulator has magnetization pointing perpendicular to the 2D semiconductor with energy

$$\mathcal{H}_Z = V_z \sum_{\mathbf{k}} c_{\mathbf{k}}^\dagger \sigma^z c_{\mathbf{k}} \quad (1.39)$$

but negligible orbital coupling. One can build an eigenbasis from the combined Hamiltonian with the following eigenenergies  $\epsilon'_\pm(\mathbf{k}) = \pm \sqrt{V_z^2 + \alpha^2 k^2}$  with eigenvectors  $u_\pm(\mathbf{k})$ . The details of the derivation can be found in appendix A.4.

With the semiconductor in contact with an  $s$ -wave superconductor, a pairing term is generated by the proximity effect. The full Hamiltonian becomes  $\mathcal{H} = \mathcal{H}_0 + \mathcal{H}_Z + \mathcal{H}_{SC}$  with

$$\mathcal{H}_{SC} = \sum_{\mathbf{k}} \Delta c_{\uparrow, \mathbf{k}}^\dagger c_{\downarrow, -\mathbf{k}}^\dagger + H.c. \quad (1.40)$$

Write the pairing potential in terms of  $c_{\pm}$  using a basis transformation to  $u_{\pm}(\mathbf{k})$ . The pairing potential Hamiltonian then becomes

$$\mathcal{H}_{SC} = \sum_{\mathbf{k}} \Delta_{++} c_{\mathbf{k},+}^{\dagger} c_{-\mathbf{k},+}^{\dagger} + \Delta_{--} c_{\mathbf{k},-}^{\dagger} c_{-\mathbf{k},-}^{\dagger} + \Delta_{+-}(\mathbf{k}) c_{\mathbf{k},+}^{\dagger} c_{-\mathbf{k},-}^{\dagger} + h.c., \quad (1.41)$$

where the  $\Delta_{\alpha\beta}$  terms can be found in appendix A.4. To write the full Hamiltonian in matrix form we will use the following Nambu spinor

$$\Psi = (c_{\mathbf{k},+}, c_{-\mathbf{k},+}^{\dagger}, c_{\mathbf{k},-}, c_{-\mathbf{k},-}^{\dagger})^T. \quad (1.42)$$

The Hamiltonian becomes

$$\mathcal{H} = \frac{1}{2} \sum_{\mathbf{k}} \Psi^{\dagger} H_{BdG} \Psi \quad (1.43)$$

with

$$H_{BdG} = \begin{bmatrix} \epsilon_+(\mathbf{k}) & 2\Delta_{++} & 0 & \Delta_{+-}(\mathbf{k}) \\ 2\Delta_{++}^* & -\epsilon_+(-\mathbf{k}) & -\Delta_{+-}^*(-\mathbf{k}) & 0 \\ 0 & -\Delta_{+-}(-\mathbf{k}) & \epsilon_-(\mathbf{k}) & 2\Delta_{--} \\ \Delta_{+-}^*(\mathbf{k}) & 0 & 2\Delta_{--}^* & -\epsilon_-(-\mathbf{k}) \end{bmatrix}, \quad (1.44)$$

and

$$\epsilon_{\pm}(\mathbf{k}) = \frac{k^2}{2m} - \mu + \epsilon'_{\pm}(\mathbf{k}). \quad (1.45)$$

Upon studying  $V_z \gg \alpha$ , near the Fermi surface the interband pairing has little effect on the band gap. Scaling it's effect from  $0 \rightarrow 1$  the intraband gap appears at a slightly smaller momentum as

the interband pairing is turned off. We use the approximation  $\Delta_{+-}(k_f) \approx 0$  and set  $\mu$  such that it only crosses the lower bands, allowing  $c_+^\dagger \rightarrow 0$ , leaving

$$H_{BdG} = \begin{bmatrix} \epsilon_-(\mathbf{k}) & 2\Delta_{--}(\mathbf{k}) \\ 2\Delta_{--}^*(\mathbf{k}) & -\epsilon_-(-\mathbf{k}) \end{bmatrix}. \quad (1.46)$$

Solving for the dispersion relation of the system

$$E_\pm(\mathbf{k}) = \pm \sqrt{(\epsilon_-(\mathbf{k}))^2 + 4|\Delta_{--}(\mathbf{k})|^2}, \quad (1.47)$$

we arrive at an effective  $p$ -wave superconductor with opening and closing band gaps.

## 1.5 Landau levels and quantum Hall effect

### 1.5.1 Landau levels in condensed matter systems

Here we will discuss the presence of Landau levels (LLs) in condensed matter systems, such as Dirac and 2DEG. In the classical case of charged QHE, the charged particles in the system are quantized in cyclotron orbits due to uniform perpendicular magnetic field, these energies are called LLs. To understand why LLs appear and QHE arises we need to first solve the Hamiltonian associated with a 2DEG and Dirac systems in the presence of a uniform perpendicular magnetic field. We can start with the square lattice tight-binding Hamiltonian for a 2DEG

$$\mathcal{H} = - \sum_{\langle j,l \rangle} t c_j^\dagger c_l + h.c., \quad (1.48)$$

and in momentum space

$$\mathcal{H} = - \sum_{\mathbf{p}} 2t (\cos(p_x a) + \cos(p_y a)) c_{\mathbf{p}}^\dagger c_{\mathbf{p}}. \quad (1.49)$$

Then, in the limit of small momenta  $p$  and shifting the constant energy term, we find

$$\mathcal{H}(\mathbf{p}) = \frac{p_x^2 + p_y^2}{2m}, \quad (1.50)$$

which is Schrodingers equation. Let us assume a 2DEG in the  $x$ - $y$  plane and have a magnetic field that points in the positive  $\hat{\mathbf{z}}$  direction,  $\mathbf{B} = B\hat{\mathbf{z}}$  or  $\mathbf{A} = Bx\hat{\mathbf{y}}$ . The Hamiltonian in momentum space becomes

$$\mathcal{H} = \frac{1}{2m} (\hat{p}_x^2 + (\hat{p}_y - qB\hat{x})^2) \quad (1.51)$$

Recall  $[\hat{r}_\alpha, \hat{p}_\beta] = i\hbar\delta_{\alpha,\beta}$ , meaning magnetic term commutes with  $\hat{p}_y$ , and lets us assume  $\Psi(x, y) = e^{ik_y y}\psi(x)$ . Acting the Hamiltonian on the ansatz wavefunction yields

$$\mathcal{H} = \frac{1}{2m} (\hat{p}_x^2 + q^2 B^2 \hat{x}^2), \quad (1.52)$$

where we let  $x - \frac{\hbar k_y}{qB} \rightarrow x$ . This is the expression for a quantum harmonic oscillator. A derivation for the energy solutions can be found in [B.1](#). The energy solutions are

$$E_n = \frac{\hbar qB}{m} \left( n + \frac{1}{2} \right) = \hbar\omega \left( n + \frac{1}{2} \right). \quad (1.53)$$

An alteration to the lattice model can have slightly different results. Using a honeycomb lattice, provided by graphene, gives the following Hamiltonian

$$\mathcal{H} = -t \sum_{\substack{j,l \\ \alpha\beta}} c_{j\alpha}^\dagger c_{l\beta} + h.c., \quad (1.54)$$

with lattice vectors  $\mathbf{a}_1 = \sqrt{3}a\hat{\mathbf{x}}$  and  $\mathbf{a}_2 = \frac{\sqrt{3}}{2}a\hat{\mathbf{x}} + \frac{3}{2}a\hat{\mathbf{y}}$ . In momentum space

$$\mathcal{H} = -t \sum_{\mathbf{p}} \begin{bmatrix} 0 & 1 + e^{i\mathbf{p}\cdot\mathbf{a}_1} + e^{i\mathbf{p}\cdot\mathbf{a}_2} \\ 1 + e^{-i\mathbf{p}\cdot\mathbf{a}_1} + e^{-i\mathbf{p}\cdot\mathbf{a}_2} & 0 \end{bmatrix},$$

which gives the following energy spectrum

$$E(\mathbf{p}) = \pm t \sqrt{3 + 2\cos(\sqrt{3}p_x a) + 4\cos\left(\frac{\sqrt{3}p_x a}{2}\right)\cos\left(\frac{3p_y a}{2}\right)}. \quad (1.55)$$

There are several high symmetry points on the corners of the Brillouin zone, one point is  $\mathbf{K} = \frac{4\pi}{3\sqrt{3}a}\hat{\mathbf{x}}$ . Expanding about  $\mathbf{K}$  with small  $\mathbf{q}$ ,  $\mathbf{q} = \mathbf{p} + \mathbf{K}$ , results in

$$t(\mathbf{q}) \approx v_F e^{i2\pi/3} (q_x - i q_y),$$

$$t^*(\mathbf{q}) \approx v_F e^{-i2\pi/3} (q_x + i q_y),$$

keeping the leading order in  $\mathbf{q}$  and  $v_F = \frac{3ta}{2}$ . Using a gauge transformation and redefining  $\mathbf{q} \rightarrow \mathbf{p}$  the Dirac equation becomes

$$\mathcal{H}(\mathbf{p}) = v_F \boldsymbol{\sigma} \cdot \mathbf{p}. \quad (1.56)$$

With graphene spanning the  $x$ - $y$  plane in the presence of a magnetic field  $\mathbf{B} = B\hat{\mathbf{z}}$ ,  $\mathbf{A} = Bx\hat{\mathbf{y}}$ , the Dirac equation becomes

$$\mathcal{H}(\mathbf{p}) = v_F \boldsymbol{\sigma} \cdot (\mathbf{p} - q\mathbf{A}). \quad (1.57)$$

A derivation for the energy solution can be found in [B.2](#). The quantized energy solutions for a 2D Dirac equation in the presence of perpendicular magnetic field are



$$E_n = v_F \sqrt{2n\hbar qB} \quad (1.58)$$

Energy in both systems produce discrete quantized energies for charged particles in cyclotron orbits with no dependence on momenta, by definition LLs. It is important to note these Landau levels are highly degenerate flat bands, which leads to bulk insulating states.

### 1.5.2 Quantized Hall conductivity and Chern number

Here we will go over the relationship between quantized Hall conductivity and Chern number, which is given as

$$\sigma_{xy} = -C \frac{e^2}{h}, \quad C \in \mathbb{Z}. \quad (1.59)$$

Consider a 2D system with translation symmetry in the  $x$  and  $y$  axis with lattice constants  $l_x$  and  $l_y$ , respectively. The Brillouin zone boundaries are

$$k_x = \frac{\pi}{l_x} [-1, 1) \quad \text{and} \quad k_y = \frac{\pi}{l_y} [-1, 1), \quad (1.60)$$

where the periodicity in  $k_x$  and  $k_y$  creates a torus,  $\mathbf{T}$ , in 3D space. We now introduce the Kubo-Greenwood formula, which is a linear response to a physical observable by a time-dependent perturbation and non-interacting, for conductivity as

$$\sigma_{xy} = i\hbar \sum_{E_a < E_F < E_b} \int_{\mathbf{T}} \frac{d^2 k}{(2\pi)^2} \frac{\langle u_{\mathbf{k}}^a | J_y | u_{\mathbf{k}}^b \rangle \langle u_{\mathbf{k}}^b | J_x | u_{\mathbf{k}}^a \rangle - \langle u_{\mathbf{k}}^a | J_x | u_{\mathbf{k}}^b \rangle \langle u_{\mathbf{k}}^b | J_y | u_{\mathbf{k}}^a \rangle}{(E_b - E_a)^2}. \quad (1.61)$$

The  $a$  and  $b$  terms represent dispersion bands below and above the Fermi energy, respectively, and a basic requirement the bands be separated to allow for an insulating state. Recall, current density defined by  $\mathbf{J} = (e/\hbar) \partial_{\mathbf{k}} H$ . If  $H$  is written in a basis where current density is non-zero we can continue. Plugging current density in Eq. (1.61) gives

$$\sigma_{xy} = \frac{ie^2}{h} \sum_{E_a < E_F < E_b} \int_{\mathbf{T}} \frac{d^2k}{2\pi} \frac{\langle u_{\mathbf{k}}^a | \partial_{k_y} H | u_{\mathbf{k}}^b \rangle \langle u_{\mathbf{k}}^b | \partial_{k_x} H | u_{\mathbf{k}}^a \rangle - \langle u_{\mathbf{k}}^a | \partial_{k_x} H | u_{\mathbf{k}}^b \rangle \langle u_{\mathbf{k}}^b | \partial_{k_y} H | u_{\mathbf{k}}^a \rangle}{(E_b - E_a)^2}. \quad (1.62)$$

Using the product rule on the following expression  $\langle \alpha | \partial_j (H | \beta) \rangle$  and using  $\sum_b = \mathbf{1} - \sum_a |u_{\mathbf{k}}^a\rangle \langle u_{\mathbf{k}}^a|$  simplifies the previous expression to

$$\sigma_{xy} = \frac{e^2}{h} \sum_a \int_{\mathbf{T}} \frac{d^2k}{2\pi} i \left( \langle \partial_{k_y} u_{\mathbf{k}}^a | \partial_{k_x} u_{\mathbf{k}}^a \rangle - \langle \partial_{k_x} u_{\mathbf{k}}^a | \partial_{k_y} u_{\mathbf{k}}^a \rangle \right) = \frac{e^2}{h} \sum_a \int_{\mathbf{T}} \frac{d^2k}{2\pi} \mathcal{F}_{xy} \quad (1.63)$$

recognizing the integral is the negative Chern number integral, which is always integer. The Hall conductivity becomes

$$\sigma_{xy} = -\frac{e^2}{h} \sum_a C_a = -C \frac{e^2}{h}. \quad (1.64)$$

Hall conductivity becomes quantized and increases for each flat band below the Fermi level. This is one way to describe the topological invariant of the quantum Hall effect by looking at geometry of momentum space with PBC.

### 1.5.3 Laughlin pump on a Hall cylinder

We demonstrate another way to describe quantum Hall effect for Landau Levels on a Hall cylinder. For a 2D system let there be PBC in the  $y$ -axis with length  $L$ , which discretizes momentum space into  $k = 2\pi n/L$  points. This creates a cylinder with  $y$  along the angular axis and  $x$  along the axial axis. Laughlin pumping requires one apply a flux along the cylinder's  $x$  axis. We can introduce the flux in the gauge potential as

$$\mathbf{A} = (Bx + \Phi/L)\hat{\mathbf{y}}. \quad (1.65)$$

Inserting the flux into the LL Schrodinger Hamiltonian gives

$$\mathcal{H} = \frac{1}{2m^*} \left( p_x^2 + \left( \frac{2\pi\hbar n}{L} + eBx + \frac{e\Phi}{L} \right)^2 \right). \quad (1.66)$$

This becomes the quantum harmonic oscillator solution seen earlier, if we set  $x' = x + x_n$  and

$$x_n = \frac{\hbar}{eBL} \left( n + \frac{\Phi}{\Phi_0} \right), \quad (1.67)$$

where  $\Phi_0 = \hbar/e$  is the flux quanta. The generalized LL wave function solution is

$$\psi_n(x) \propto H_n(x + x_n) e^{-eB(x+x_n)^2/2\hbar} e^{i2\pi n/L}, \quad (1.68)$$

where  $H_n(x)$  is the Hermite polynomial. Solving for  $\langle x_n \rangle = \langle \psi_n(x) | x | \psi_n(x) \rangle$  results in each electron centered at Eq. (1.67).

When the flux increases by one flux quanta, the electron's center of mass shifts by an integer multiple, moving from states  $n \rightarrow n + 1$ . This causes a charge transfer as electrons are pumped across the Laughlin cylinder. If  $n$  LLs are filled,  $n$  electrons are transferred, hence  $\Delta Q = ne$ . Hall conductivity is  $\sigma_H = \Delta Q / \Delta \Phi$ , and for a change in  $n$  flux quanta, it becomes quantized as  $\sigma_H = ne^2/h$ . Thus, Hall conductivity remains quantized in LLs systems mapped to a Laughlin cylinder.

## Chapter 2

# Superconducting Triangular Islands as a Platform for Manipulating Majorana Zero Modes

### 2.1 Context

This chapter consists of the paper *Superconducting triangular islands as a platform for manipulating Majorana zero modes*, which was published in Physical Review B in 2024. The full reference is:

A. Winblad, H. Chen, Phys. Rev. B **109**, 205158 (2024).

The supplemental information is shown in section [2.4](#). This article shows two ways to incorporate geometry and gauge potentials in triangular lattice models to host and manipulate Majorana zero modes for topological quantum computing systems.

### 2.2 Paper abstract

Current proposals for topological quantum computation (TQC) based on Majorana zero modes (MZM) have mostly been focused on coupled-wire architecture which can be challenging to implement experimentally. To explore alternative building blocks of TQC, in this work we study the possibility of obtaining robust MZM at the corners of triangular superconducting islands, which often appear spontaneously in epitaxial growth. We first show that a minimal three-site triangle model of spinless  $p$ -wave superconductor allows MZM to appear at different pairs of vertices controlled by a staggered vector potential, which may be realized using coupled quantum dots and can already demonstrate braiding. For systems with less fine-tuned parameters, we suggest an alternative structure of a “hollow” triangle subject to uniform supercurrents or vector potentials, in which MZM generally appear when two of the edges are in a different topological phase from the third. We also discuss the feasibility of constructing the tri-

angles using existing candidate MZM systems and of braiding more MZM in networks of such triangles.

## 2.3 Research article

### Introduction

For more than twenty years, Majorana zero modes (MZM) in condensed matter systems have been highly sought after due to their potential for serving as building blocks of topological quantum computation, thanks to their inherent robustness against decoherence and non-Abelian exchange statistics [8, 9, 11–13]. MZM were originally proposed to be found in half-quantum vortices of two-dimensional (2D) topological  $p$ -wave superconductors and at the ends of 1D spinless  $p$ -wave superconductors [7, 14]. Whether a pristine  $p$ -wave superconductor [15] has been found is still under debate. However, innovative heterostructures proximate to ordinary  $s$ -wave superconductors have been proposed to behave as effective topological superconductors in both 1D and 2D. These include, for example, semiconductor nanowires subject to magnetic fields [16–18], ferromagnetic atomic spin chains [19–24], 3D topological insulators [25–28], quantum anomalous Hall insulators [29–31], quasi-2D spin-orbit-coupled superconductors with a perpendicular Zeeman field [10, 32–36], and planar Josephson junctions [37–43], etc. It has been a challenging task to decisively confirm the existence of MZM in the various experimental systems due to other competing mechanisms that can potentially result in similar features as MZM do in different probes [40, 41, 44–49]. Other proposals for constructing Kitaev chains through a bottom-up approach, based on, e.g. magnetic tunnel junctions proximate to spin-orbit-coupled superconductors [50], and quantum dots coupled through superconducting links [51–53] are therefore promising. In particular, the recent experiment [53] of a designer minimal Kitaev chain based on two quantum dots coupled through tunable crossed Andreev reflections (CAR) offers a compelling route towards MZM platforms based on exactly solvable building blocks.

In parallel with the above efforts of realizing MZM in different materials systems, scalable architectures for quantum logic circuits based on MZM have also been intensely studied over the past decades. A major proposal among these studies is to build networks of T-junctions, which are minimal units for swapping a pair of MZM hosted at different ends of a junction, that allow braiding-based TQC [13]. Alternatively, networks based on coupled wires forming the so-called tetrons and hexons, aiming at measurement-based logic gate operations [54], have also been extensively investigated. To counter the technical challenges of engineering networks with physical wires or atomic chains, various ideas based on effective Kitaev chains, such as quasi-1D systems in thin films [55], cross Josephson junctions [43], scissor cuts on a quantum anomalous Hall insulator [31], and rings of magnetic atoms [56], etc. have been proposed. However, due to the same difficulty of obtaining or identifying genuine MZM in quasi-1D systems mentioned above, it remains unclear how practical these strategies are in the near future. These challenges, along with the advancements in building designer minimal Kitaev chains, motivate us to explore new MZM platforms that are not based on bulk-boundary correspondence: In small systems with only a few fermion degrees of freedom, discussing the emergence of MZM due to bulk-boundary correspondence is less meaningful. Instead, it is easier to fine-tune system parameters based on exactly solvable models to realize well-behaved MZM.

Additionally, in this Letter we highlight triangular superconducting islands as a promising structural unit for manipulating MZM. Unique geometries combined with simple protocols of control parameters can greatly facilitate MZM creation and operations [56–59]. We also note that triangles naturally break 2D inversion symmetry and do not present a straightforward strategy for morphing into either 1D or 2D structures with periodic boundary conditions, implying different bulk-boundary physics from other quasi-2D structures. Finally, it is worth mentioning that triangular islands routinely appear spontaneously in epitaxial growth [60] on close-packed atomic surfaces.

In this Letter we propose two triangular geometry designs that are pertinent to different experimental platforms. The first is an exactly solvable “Kitaev triangle” model consisting of

three fermion sites. The Kitaev triangle hosts MZM at different pairs of vertices controlled by Peierls phases on the three edges [Fig. 2.1 (a)], that is not due to topological bulk-boundary correspondence, and can realize the braiding of two MZM. The second is finite-size triangles with a hollow interior [Fig. 2.1 (b)] under a uniform vector potential, which tunes its individual edges into different topological phases. Compared to existing proposals based on vector potentials or supercurrents [61–64], our design explores the utility of geometry rather than the individual control of superconducting nanowires. We also discuss scaled-up networks of triangles for implementing braiding operations of MZM.

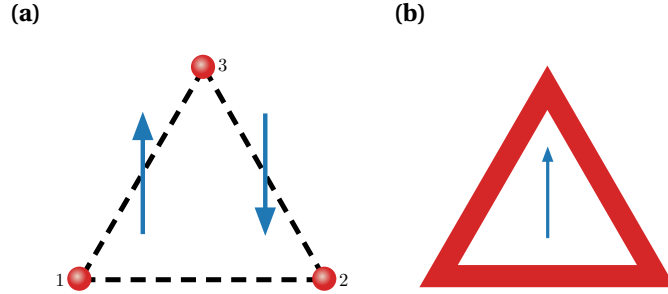


**Figure 2.1:** Schematics of two triangle structures proposed in this work. (a) Three-site Kitaev triangle with bond-dependent Peierls phases. (b) Hollow triangular island with a uniform vector potential.

### Kitaev triangle

In this section we present an exactly solvable minimal model with three sites forming a “Kitaev triangle” that can host MZM at different pairs of vertices controlled by Peierls phases on the edges. The Bogoliubov-de Gennes (BdG) Hamiltonian includes complex hopping and  $p$ -wave pairing between three spinless fermions forming an equilateral triangle [Fig. 2.1 (a)]:

$$\mathcal{H} = \sum_{\langle jl \rangle} (-te^{i\phi_{jl}} c_j^\dagger c_l + \Delta e^{i\theta_{jl}} c_j c_l + \text{h.c.}) - \sum_j \mu c_j^\dagger c_j, \quad (2.1)$$

where  $t$  is the hopping amplitude,  $\Delta$  is the amplitude of the (2D)  $p$ -wave pairing,  $\mu$  is the chemical potential,  $\theta_{jl}$  is the azimuthal angle of  $\mathbf{r}_{jl} = \mathbf{r}_l - \mathbf{r}_j$  (the  $x$  axis is chosen to be along  $\mathbf{r}_{12}$ ),

consistent with  $\{c_l^\dagger, c_j^\dagger\} = 0$ .  $\phi_{jl}$  is the Peierls phase due to a bond-dependent vector potential  $\mathbf{A}$  to be specified below (the nearest neighbor distance  $a$  is chosen to be the length unit and  $e = \hbar = 1$  hereinbelow):  $\phi_{jl} = \int_{\mathbf{r}_j}^{\mathbf{r}_l} \mathbf{A} \cdot d\mathbf{l} = -\phi_{lj}$ . We have chosen a gauge so that the vector potential only appears in the normal part of the Hamiltonian [65], and the  $p$ -wave gap  $\Delta$  is assumed to be an effective one induced by proximity to a neighboring superconductor, on which the vector potential has negligible influence. The minimal model may be realized as an effective low-energy model of carefully engineered mesoscopic superconductor devices, such as that made by quantum dots connected by superconducting islands [53]. Rewriting  $\mathcal{H}$  in the Majorana fermion basis  $a_j = c_j + c_j^\dagger$ ,  $b_j = \frac{1}{i}(c_j - c_j^\dagger)$  and specializing to the Kitaev limit  $t = \Delta$ ,  $\mu = 0$ , we can obtain explicit conditions for getting MZM at different sites [66]. For example, first let  $\phi_{12} = 0$  so that sites 1 and 2 alone form a minimal Kitaev chain with  $\mathcal{H}_{12} = itb_1a_2$  and hosting MZM  $a_1$  and  $b_2$ . Then one can set  $\phi_{23}$  and  $\phi_{31}$  so that all terms involving the above two Majorana operators cancel out. Solving the corresponding equations gives  $\phi_{23} = -\pi/3$  and  $\phi_{31} = -\phi_{13} = -\pi/3$ . The three Peierls phases can be realized by the following staggered vector potential

$$\mathbf{A} = [1 - 2\Theta(x)] \frac{2\pi}{3\sqrt{3}} \hat{\mathbf{y}} \quad (2.2)$$

where  $\Theta(x)$  is the Heavisde step function. The above condition for MZM localized at triangle corners can be generalized to Kitaev chains forming a triangular loop, as well as to finite-size triangles of 2D spinless  $p$ -wave superconductors in the Kitaev limit, as the existence of  $a_1$  and  $b_2$  are only dictated by the vector potential near the corresponding corners. It should be noted that in the latter case, 1D edge states will arise when the triangle becomes larger, and effectively diminish the gap that protects the corner MZM. In this sense, the gap that protects the MZM in the Kitaev triangle model, defined by the energies of the first excited states  $\pm(1 - \frac{\sqrt{2}}{2})t \approx \pm 0.29t$  [66], is due to finite size effects. On the other hand, for the longer Kitaev chain, another pair of MZM will appear near the two bottom vertices which can be understood using a topological argument given in the next section. In this sense, the MZM in the Kitaev triangle here are not



due to topological bulk-boundary correspondence [the point of  $A = \frac{2\pi}{3\sqrt{3}}$  and  $\mu = 0$  sits in the trivial phase in Fig. 2.3 (a)].

We next show that the minimal Kitaev triangle suffices to demonstrate braiding of MZM. To this end we consider a closed parameter path linearly interpolating between the following sets of values of  $\phi_{jl}$ :

$$(\phi_{12}, \phi_{23}, \phi_{31}) : \boldsymbol{\phi}_1 \rightarrow \boldsymbol{\phi}_2 \rightarrow \boldsymbol{\phi}_3 \rightarrow \boldsymbol{\phi}_1 \quad (2.3)$$

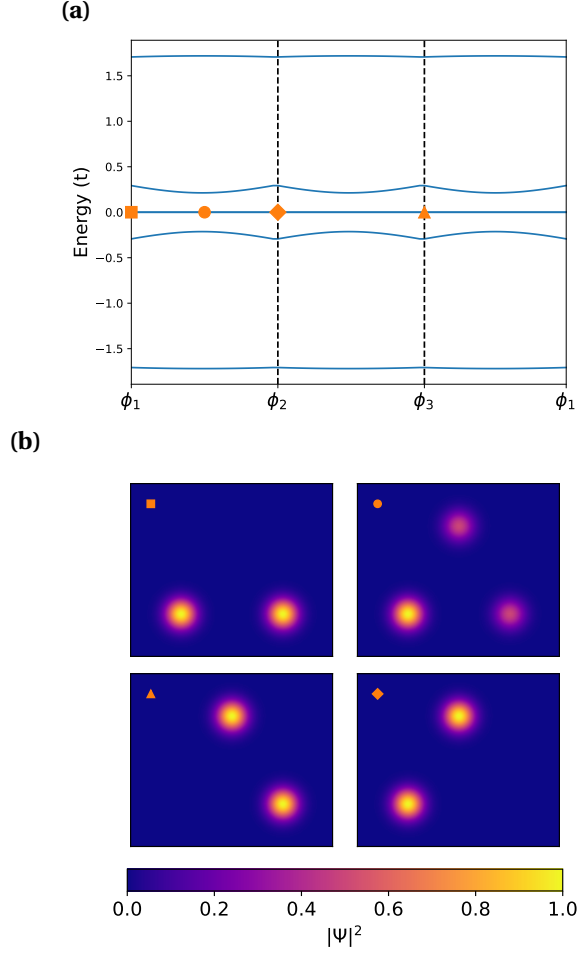
with  $\boldsymbol{\phi}_1 = (0, -\frac{\pi}{3}, -\frac{\pi}{3})$ ,  $\boldsymbol{\phi}_2 = (-\frac{\pi}{3}, -\frac{\pi}{3}, 0)$ ,  $\boldsymbol{\phi}_3 = (-\frac{\pi}{3}, 0, -\frac{\pi}{3})$ . It is straightforward to show that at  $\boldsymbol{\phi}_2$  and  $\boldsymbol{\phi}_3$  there are MZM located at sites 1, 3 and 2, 3, respectively. Therefore the two original MZM at sites 1, 2 should switch their positions at the end of the adiabatic evolution.

Fig. 2.2 shows that the MZM stays at zero energy throughout the parameter path that interchanges their positions. In [66] we proved the exact degeneracy of the MZM along the path [67]. To show that such an operation indeed realizes braiding, we explicitly calculated the many-body Berry phase of the evolution [9, 56, 66] and found the two degenerate many-body ground states acquire a  $\frac{\pi}{2}$  difference in their Berry phases as expected [9]. Compared to the minimum T-junction model with four sites [9, 68], our Kitaev triangle model only requires three sites to achieve braiding between two MZM, and is potentially easier to engineer experimentally.

### Hollow triangles

For systems with less fine-tuned Hamiltonians than the minimal model in the previous section, it is more instructive to search for MZM based on topological bulk-boundary correspondence. In this section we show that MZM generally appear at the corners of a hollow triangle, which can be approximated by joining three finite-width chains or ribbons whose bulk topology is individually tuned by the same uniform vector potential.

To this end, we first show that topological phase transitions can be induced by a vector potential in a spinless  $p$ -wave superconductor ribbon as illustrated in Fig. 2.3 (a). In comparison with similar previous proposals that mostly focused on vector potentials or supercurrents flow-



**Figure 2.2:** (a) Evolution of the eigenvalues of the 3-site Kitaev triangle along the closed parameter path for  $\phi$  on the three edges. (b) MZM wavefunctions at different points of the parameter path. Clockwise from the upper left panel:  $\phi_1 \rightarrow \frac{1}{2}(\phi_1 + \phi_2) \rightarrow \phi_2 \rightarrow \phi_3$ .

ing along the chain [61, 62], we consider in particular the tunability by varying the direction of the vector potential relative to the length direction of the ribbon, which will become instrumental in a triangular structure.

Consider Eq. (A.74) on a triangular lattice defined by unit-length lattice vectors  $(\mathbf{a}_1, \mathbf{a}_2) = (\hat{\mathbf{x}}, \frac{1}{2}\hat{\mathbf{x}} + \frac{\sqrt{3}}{2}\hat{\mathbf{y}})$  with  $W$  unit cells along  $\mathbf{a}_2$  but infinite unit cells along  $\mathbf{a}_1$ , and assume the Peierls phases are due to a uniform vector potential  $\mathbf{A}$  so that  $\phi_{jl} = \mathbf{A} \cdot \mathbf{r}_{jl}$ . The Hamiltonian is periodic along  $x$  and can be Fourier transformed through  $c_{m,n}^\dagger = \frac{1}{\sqrt{N}} \sum_k c_{k,n}^\dagger e^{-ikm}$ , where  $m, n$  label the lattice sites as  $\mathbf{r}_{m,n} = m\mathbf{a}_1 + n\mathbf{a}_2$ . The resulting momentum space Hamiltonian [66] can then be used to calculate the Majorana number [7, 69]  $\mathcal{M}$  of the 1D ribbon. When  $\mathcal{M} = -1$ , the 1D

system is in a nontrivial topological phase with MZM appearing at open ends of semi-infinite ribbons, and otherwise for  $\mathcal{M} = 1$ .

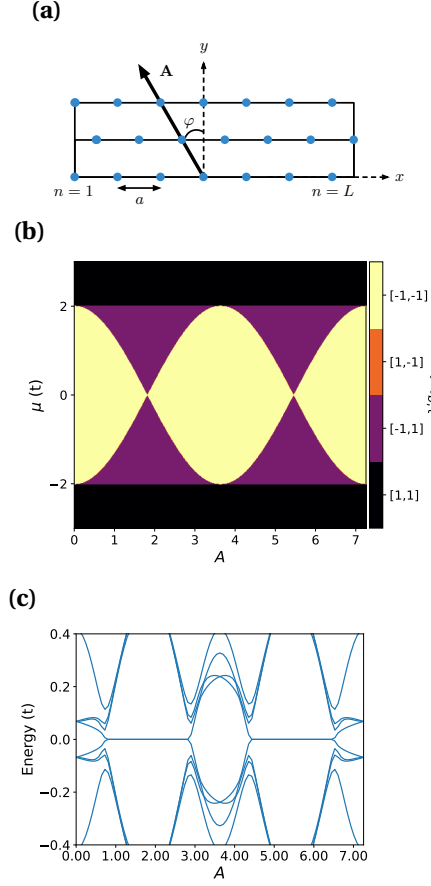


**Figure 2.3:** (a) Schematic illustration of a finite-width ( $W = 3$  here) ribbon based on the triangular lattice in the presence of a vector potential  $\mathbf{A} = A(-\sin\varphi\hat{\mathbf{x}} + \cos\varphi\hat{\mathbf{y}})$ . (b) Topological phase diagram for a  $W = 1$  triangular chain obtained by superimposing the  $\mathcal{M}_{b,t}(A, \mu)$  ( $b$ -bottom edge,  $t$ -top edges) plots of 1D chains with  $\mathbf{A} = A\hat{\mathbf{y}}$  (bottom edge) and  $\mathbf{A} = A(\frac{\sqrt{3}}{2}\hat{\mathbf{x}} + \frac{1}{2}\hat{\mathbf{y}})$  (top edges). Color scheme: black— $[\mathcal{M}_b, \mathcal{M}_t] = [1, 1]$ , yellow— $[-1, -1]$ , purple— $[-1, 1]$ , orange— $[1, -1]$  (not present in this case) (b) Near-gap BdG eigen-energies vs  $A$  for a finite triangle with edge length  $L = 50$ ,  $W = 1$ , and  $\mu = 1.6$ .  $t = \Delta = 1$  in all calculations.

In Fig. 2.3 (b) we show the topological phase diagrams for a 1D ribbon with width  $W = 1$ ,  $\mathbf{A} = A\hat{\mathbf{y}}$  and  $\mathbf{A} = A(\frac{\sqrt{3}}{2}\hat{\mathbf{x}} + \frac{1}{2}\hat{\mathbf{y}})$  superimposed. We found that the vector potential component normal to the ribbon length direction has no effect on the Majorana number, nor does the sign of its component along the ribbon length direction. However, topological phase transitions can be induced by varying the size of the vector potential component along the ribbon, consistent

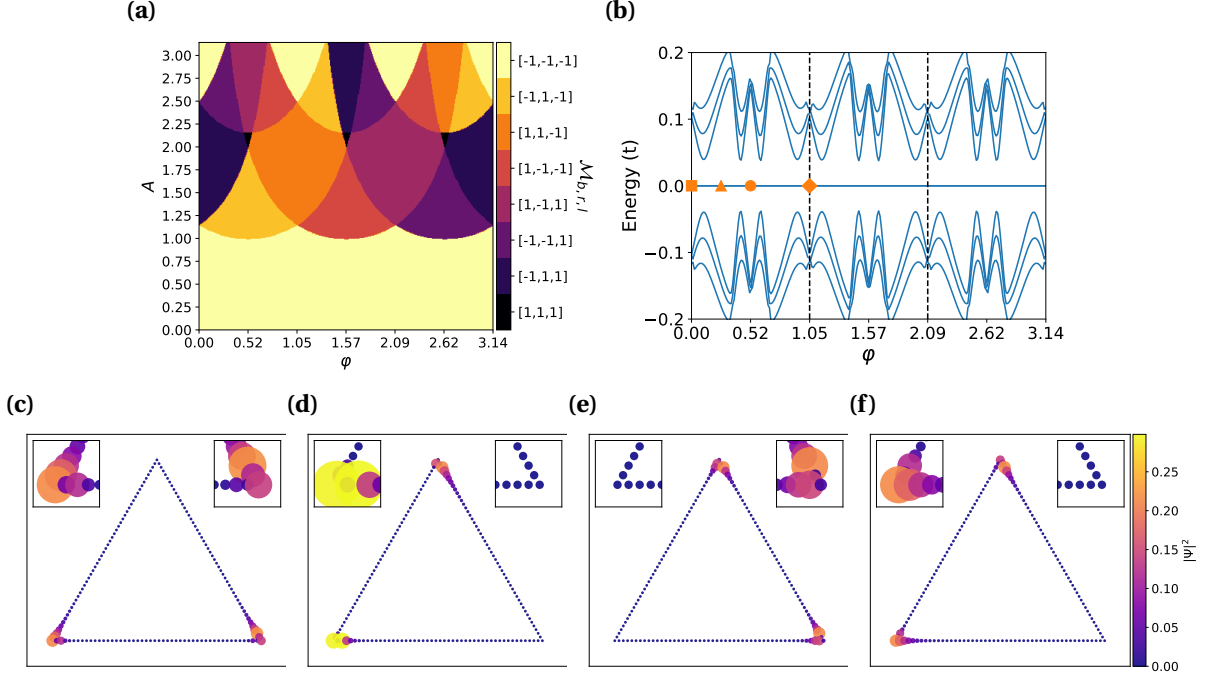


**Figure 2.4:** (a) Topological phase diagram for a  $W = 1$  triangle by superimposing the  $\mathcal{M}_{b,r,l}(A, \varphi)$  plots of 1D chains ( $b$ -bottom,  $r$ -right,  $l$ -left,  $\mu = 1.1$ ).  $\varphi_{r,l}$  are equal to  $\varphi_b + \pi/3$  and  $\varphi_b - \pi/3$ , respectively. The colors are coded by which edges have non-trivial topology. For example, Black— $[\mathcal{M}_b, \mathcal{M}_r, \mathcal{M}_l] = [1, 1, 1]$  means all edges are trivial. The behavior depicted in panels (b-f) is representative of that when  $A$  is in the range of (2.25, 2.5), for which the  $\mathcal{M} = -1$  phase “crawls” through the three edges counterclockwise as  $\varphi$  increases. (b) Spectral flow of a triangle with  $W = 1$ ,  $L = 50$ ,  $\mu = 1.1$ , and  $A = 2.35$  with increasing  $\varphi$ . (c-f) BdG eigenfunction  $|\Psi|^2$  summed over the two zero modes at  $\varphi = 0$ ,  $\frac{\pi}{12}$ ,  $\frac{\pi}{6}$ , and  $\frac{\pi}{3}$ , respectively. The bottom edge is parallel with  $\hat{x}$  in the coordinates illustrated in Fig. 2.3 (a).

with previous results [61, 62]. These properties motivate us to consider the structure of a hollow triangle formed by three finite-width ribbons subject to a uniform vector potential  $\mathbf{A} = A\hat{y}$  as illustrated in Fig. 2.1 (b), in which the bottom edge is aligned with  $\hat{x}$ . The purple regions on the phase diagram Fig. 2.3 (a) mean the bottom edge and the two upper edges of the hollow triangle have different  $\mathcal{M}$ , which should give rise to MZM localized at the two bottom corners if the triangle is large enough so that bulk-edge correspondence holds, and gap closing does not occur at other places along its edges.

To support the above arguments, we directly diagonalize the BdG Hamiltonian of a finite hollow triangle with edge length  $L = 50$  and width  $W = 1$ . Fig. 2.3 (c) shows the spectral flow (BdG eigen-energies evolving with increasing vector potential  $A$ ) close to zero energy at chem-

ical potential  $\mu = 1.6$ . Indeed, zero-energy modes appear in the regions of  $\mu$  and  $A$  consistent with the phase diagram. Hollow triangles with larger  $W$  also have qualitatively similar behavior, although the phase diagrams are more complex [66]. The eigenfunctions for the zero-energy modes at  $A = 2.35$  and  $\mu = 1.1$  in Fig. 2.4 (c) also confirm their spatial localization at the bottom corners of the triangle.

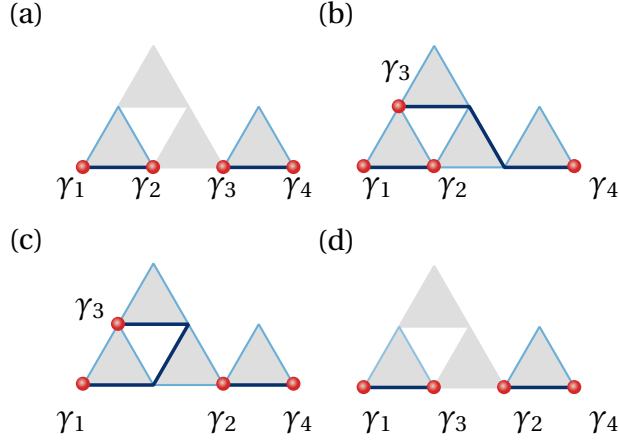
We next show that rotating the uniform vector potential in-plane, guided by the phase diagram of the three edges overlapped together [Fig. 2.4 (a)], can manipulate the positions of the MZM. Specifically, a desired path on the  $(A, \varphi)$  plane,  $\varphi$  being the in-plane azimuthal angle of  $\mathbf{A}$  [Fig. 2.3 (a)], of the phase diagram should make the nontrivial  $\mathcal{M} = -1$  phase cycle through the three edges but without entering any trivial regions, when all edges have the same  $\mathcal{M}$ .

Fig. 2.4 (b) plots the spectral flow versus  $\varphi$  for a path determined in the above manner, which clearly shows that the zero-energy modes persist throughout the rotation and the bulk gap never closes. At a critical point when individual edges change their topology, e.g., near the middle of the  $\varphi \in [0, \pi/6)$  region, gap closing is avoided due to finite-size effects, as discussed in [9]. Figs. 2.4 (c-f) plot the BdG wavefunctions of the MZM at special values of  $\varphi$ . One can see that the two MZM appear to cycle through the three vertices by following the rotation of  $\mathbf{A}$ . We note in passing that if the vector potentials on the three edges can be controlled independently similar to the Kitaev triangle case, a swapping of the two MZM can in principle be achieved as well.

In [66] we also gave an example of a  $W = 3$  triangle, for which one has to additionally consider the nontrivial dependence of the bulk gap of the three edges on  $\mathbf{A}$ . In general, optimization of the parameter path can be done by examining the (suitably designed) topological phase diagram together with the bulk gap diagram, and choosing triangles of appropriate sizes.

Before ending this section, we present a tentative design for braiding more than two MZM based on our hollow triangles. The structure, illustrated in Fig. 2.5, consists of four triangles sharing corners with their neighbors. The critical step of transporting  $\gamma_2$  to the left vertex of the rightmost triangle, corresponding to Figs. 2.5 (b,c), can be achieved by rotating the vector

potential of the bottom-middle triangle counterclockwise from  $\varphi = \frac{\pi}{6}$  to  $\frac{\pi}{3}$ , which swaps the topological phases of the two side edges as shown in Fig. 2.4. In [66] we show this operation does not involve gap closing when the parameter path is chosen judiciously.



**Figure 2.5:** Representative steps for braiding four MZM in four triangles sharing corners. (a) Initialization of four MZM  $\gamma_1, \gamma_2, \gamma_3, \gamma_4$ . All three edges of the bottom-middle and the top triangles are in the trivial phase by e.g. controlling the chemical potential. The bottom-left and bottom-right triangles have  $\varphi = 0$  so that their bottom edges are nontrivial. (b) Moving  $\gamma_3$  by “switching on” the middle triangle by changing the chemical potential under a fixed vector potential at  $\varphi = \frac{\pi}{6}$ , and then turning on the top triangle with similar means except  $\varphi = 0$ . (c) Transporting  $\gamma_2$  to the right triangle through rotating the vector potential in the middle triangle counterclockwise by  $\pi/6$ . (d) Moving  $\gamma_3$  to the left triangle by “switching off” the top triangle followed by the middle triangle.

## Discussion

The hollow interior of the triangles considered in this work is needed for two reasons: (1)  $W \ll L$  is required for bulk-edge correspondence based on 1D topology to hold; (2) A finite  $W$  is needed to gap out the chiral edge states of a 2D spinless  $p$ -wave superconductor. The latter is not essential if one does not start with a spinless  $p$ -wave superconductor but a more realistic model such as the Rashba+Zeeman+s-wave pairing model. On the other hand, the former constraint may also be removed if one uses the Kitaev triangle. Nonetheless, an effective 3-site Kitaev triangle may emerge as the effective theory of triangular structures if a three-orbital low-energy Wannier basis can be isolated, similar to the continuum theory of moiré structures.

We also note that the corner MZM in our triangles appear due to different reasons from that in higher-order topological superconductors [47, 57–59].

For possible physical realizations of our triangles, immediate choices are quantum dots forming a Kitaev triangle [53], planar Josephson junctions or cuts on quantum anomalous Hall insulator/superconductor heterostructures [31] that form a hollow triangle, and triangular atomic chains assembled by an STM tip [24] on a close-packed surface. The quantum-dot platform may be advantageous in the convenience of implementing parity readout by turning the third vertex temporarily into a normal quantum dot [67, 70, 71]. Looking into the future, it is more intriguing to utilize the spontaneously formed triangular islands in epitaxial growth [60] with the center region removed either physically by lithography/ablation, or electrically by gating. To create a staggered vector potential or supercurrent profile for the Kitaev triangle, one can use a uniform magnetic field, corresponding to a constant vector potential gradient, plus a uniform supercurrent that controls the position of the zero. It is also possible to use two parallel superconducting wires with counter-propagating supercurrents proximate to the triangle. Our work provides a versatile platform for manipulating MZM based on currently available candidate MZM systems and for potentially demonstrating the non-Abelian nature of MZM in near-term devices.

## 2.4 Supplemental material

### Analytic solutions of the Kitaev triangle

In this section we present some analytic results related to the 3-site Kitaev triangle.

We start from the 1D Kitaev chain Hamiltonian with complex nearest-neighbor hopping  $-te^{i\phi}$  and  $p$ -wave pairing  $\Delta e^{i\theta}$  in the Kitaev limit ( $t = \Delta > 0, \mu = 0$ ):

$$H = \sum_n \left( -te^{i\phi} c_n^\dagger c_{n+1} + \Delta e^{i\theta} c_n c_{n+1} + \text{h.c.} \right) \quad (2.4)$$

In the Majorana fermion basis  $a_n = c_n + c_n^\dagger$ ,  $b_n = -i(c_n - c_n^\dagger)$  the Hamiltonian becomes

$$H = -\frac{it}{2} \sum_n [(S_\phi - S_\theta) a_n a_{n+1} + (S_\phi + S_\theta) b_n b_{n+1} + (C_\phi - C_\theta) a_n b_{n+1} - (C_\phi + C_\theta) b_n a_{n+1}] \quad (2.5)$$

where  $S_\phi \equiv \sin \phi$ ,  $C_\phi \equiv \cos \phi$ , etc. Therefore, when  $\phi = \theta$ ,  $a_n$  becomes decoupled from  $a_{n+1}$  and  $b_{n+1}$ , and  $a_1$  drops out from the Hamiltonian. Similarly, when  $\phi = \theta + \pi$ ,  $b_1$  becomes isolated. To find the other MZM, we note that when  $\phi = \theta$ , terms involving  $a_N$  and  $b_N$  in the Hamiltonian are

$$H_N = -it b_{N-1} (S_\phi b_N - C_\phi a_N). \quad (2.6)$$

Considering the unitary transformation

$$\begin{pmatrix} a'_N \\ b'_N \end{pmatrix} \equiv \begin{pmatrix} C_\phi & -S_\phi \\ S_\phi & C_\phi \end{pmatrix} \begin{pmatrix} a_N \\ b_N \end{pmatrix} \quad (2.7)$$

we have

$$H_N = it b_{N-1} a'_N \quad (2.8)$$

Therefore the other MZM is  $b'_N = S_\phi a_N + C_\phi b_N$ . Similarly, when  $\phi = \theta + \pi$  the other MZM is  $a'_N \equiv C_\phi a_N - S_\phi b_N$ .

For the 3-site Kitaev triangle at the initial configuration  $\phi_1$ , if the three edges were isolated from each other, the MZM would have been

$$1-2: \quad a_1, b_2 \quad (2.9)$$

$$2-3: \quad b_2, \frac{1}{2}a_3 + \frac{\sqrt{3}}{2}b_3$$

$$3-1: \quad a_1, \frac{\sqrt{3}}{2}a_3 + \frac{1}{2}b_3$$



One can therefore see that the two MZM at site 3 are not compatible with each other.

We next solve for the excited states of the Kitaev triangle at the initial configuration  $\phi_1$ . The Hamiltonian in the Majorana basis is

$$H = -\frac{it}{2} \left( -2b_1 a_2 - \sqrt{3} a_2 a_3 + a_2 b_3 + \sqrt{3} b_1 b_3 - b_1 a_3 \right) = \frac{1}{2} \Gamma h \Gamma^T \quad (2.10)$$

$$\Gamma \equiv (b_1, a_2, a_3, b_3)$$

$$h \equiv -it \begin{pmatrix} 0 & -1 & -\frac{1}{2} & \frac{\sqrt{3}}{2} \\ 1 & 0 & -\frac{\sqrt{3}}{2} & \frac{1}{2} \\ \frac{1}{2} & \frac{\sqrt{3}}{2} & 0 & 0 \\ -\frac{\sqrt{3}}{2} & -\frac{1}{2} & 0 & 0 \end{pmatrix} = t \left( -\frac{1}{2} \sigma_0 \tau_y - \frac{1}{2} \sigma_z \tau_y - \frac{1}{2} \sigma_y \tau_z + \frac{\sqrt{3}}{2} \sigma_x \tau_y \right)$$

$h$  has the following symmetry:

$$O = \left( \frac{\sqrt{3}}{2} \sigma_x - \frac{1}{2} \sigma_z \right) \tau_y \quad (2.11)$$

We therefore rotate the Hamiltonian so that  $O$  becomes diagonal using the following unitary operator

$$U = e^{-\frac{i\pi}{3} \sigma_y} \otimes e^{i\frac{\pi}{4} \tau_x} \quad (2.12)$$

which leads to

$$U^\dagger O U = \text{Diag}(1, -1, -1, 1) \quad (2.13)$$

$U$  therefore block-diagonalizes  $h$  as

$$U^\dagger h U = \frac{t}{2} \begin{pmatrix} 1 & & -1 \\ & -1 & 1 \\ & 1 & -3 \\ -1 & & 3 \end{pmatrix} \quad (2.14)$$

which can then be diagonalized by

$$V = \begin{pmatrix} \frac{1+\sqrt{2}}{\sqrt{4+2\sqrt{2}}} & 0 & \frac{1-\sqrt{2}}{\sqrt{4-2\sqrt{2}}} & 0 \\ 0 & \frac{1+\sqrt{2}}{\sqrt{4+2\sqrt{2}}} & 0 & \frac{1-\sqrt{2}}{\sqrt{4-2\sqrt{2}}} \\ 0 & \frac{1}{\sqrt{4+2\sqrt{2}}} & 0 & \frac{1}{\sqrt{4-2\sqrt{2}}} \\ \frac{1}{\sqrt{4+2\sqrt{2}}} & 0 & \frac{1}{\sqrt{4-2\sqrt{2}}} & 0 \end{pmatrix} \quad (2.15)$$

as

$$V^\dagger U^\dagger h U V = t \times \text{Diag} \left( 1 - \frac{\sqrt{2}}{2}, -1 + \frac{\sqrt{2}}{2}, 1 + \frac{\sqrt{2}}{2}, -1 - \frac{\sqrt{2}}{2} \right) \quad (2.16)$$

We therefore have the two lowest excited states with eigenenergies  $\pm t(1 - \frac{\sqrt{2}}{2})$

$$\begin{aligned} \psi_{+1} &= \Gamma U \begin{pmatrix} \frac{1+\sqrt{2}}{\sqrt{4+2\sqrt{2}}} \\ 0 \\ 0 \\ \frac{1}{\sqrt{4+2\sqrt{2}}} \end{pmatrix} = \Gamma \times \frac{1}{4\sqrt{2+\sqrt{2}}} \begin{pmatrix} 1 + \sqrt{2} - \sqrt{3}i \\ (1 + \sqrt{2})i - \sqrt{3} \\ i + \sqrt{3} + \sqrt{6} \\ 1 + (\sqrt{3} + \sqrt{6})i \end{pmatrix} \\ \psi_{-1} &= \Gamma U \begin{pmatrix} 0 \\ \frac{1+\sqrt{2}}{\sqrt{4+2\sqrt{2}}} \\ \frac{1}{\sqrt{4+2\sqrt{2}}} \\ 0 \end{pmatrix} = \Gamma \times \frac{1}{4\sqrt{2+\sqrt{2}}} \begin{pmatrix} (1 + \sqrt{2})i - \sqrt{3} \\ 1 + \sqrt{2} - \sqrt{3}i \\ 1 + (\sqrt{3} + \sqrt{6})i \\ i + \sqrt{3} + \sqrt{6} \end{pmatrix} \end{aligned} \quad (2.17)$$

The first excited states can therefore be understood as a hybridization between the “bulk” states of the 1-2 bond and the fermion on site 3. The other two eigenstates can be obtained similarly.

We next prove that in the braiding process given in the main text there is always a pair of MZM at exactly zero energy. Without loss of generality we consider the  $\phi_1 \rightarrow \phi_2$  step. The Hamiltonian in the fermion basis becomes

$$\begin{aligned}
H = & -e^{ix}c_1^\dagger c_2 + c_1 c_2 + e^{-ix}c_1 c_2^\dagger - c_1^\dagger c_2^\dagger \\
& -e^{-\frac{\pi}{3}i}c_2^\dagger c_3 + e^{\frac{2\pi}{3}i}c_2 c_3 + e^{\frac{\pi}{3}i}c_2 c_3^\dagger - e^{-\frac{2\pi}{3}i}c_2^\dagger c_3^\dagger \\
& + e^{(-\frac{\pi}{3}-x)i}c_1 c_3^\dagger - e^{-\frac{2\pi}{3}i}c_1 c_3 - e^{(\frac{\pi}{3}+x)i}c_1^\dagger c_3 + e^{\frac{2\pi}{3}i}c_1^\dagger c_3^\dagger
\end{aligned} \tag{2.18}$$

where we have temporarily omitted the energy unit  $t$ . We then have

$$\begin{aligned}
[c_1^\dagger, H] &= c_2 + e^{-ix}c_2^\dagger + e^{(-\frac{\pi}{3}-x)i}c_3^\dagger - e^{-\frac{2\pi}{3}i}c_3 \\
[c_1, H] &= -[c_1^\dagger, H]^\dagger = -e^{ix} \left[ c_2 + e^{-ix}c_2^\dagger - e^{-\frac{2\pi}{3}i}c_3 + e^{(-\frac{\pi}{3}-x)i}c_3^\dagger \right]
\end{aligned} \tag{2.19}$$

Therefore

$$[e^{\frac{ix}{2}}c_1^\dagger + e^{-\frac{ix}{2}}c_1, H] = 0 \tag{2.20}$$

Namely we have an MZM:

$$\tilde{a}_1 \equiv e^{\frac{ix}{2}}c_1^\dagger + e^{-\frac{ix}{2}}c_1 = C_{\frac{x}{2}}a_1 + S_{\frac{x}{2}}b_1 \tag{2.21}$$

To find the other MZM, we calculate the commutators between the other fermion operators with the Hamiltonian:

$$\begin{aligned}
[c_2^\dagger, H] &= e^{ix} c_1^\dagger - c_1 - e^{-\frac{i\pi}{3}} c_3 + e^{\frac{i\pi}{3}} c_3^\dagger \\
[c_2, H] &= -e^{-ix} c_1 + c_1^\dagger + e^{\frac{i\pi}{3}} c_3^\dagger - e^{-\frac{i\pi}{3}} c_3 \\
[c_3^\dagger, H] &= e^{-\frac{i\pi}{3}} c_2^\dagger + e^{-\frac{i\pi}{3}} c_2 - e^{\frac{i\pi}{3}} c_1 + e^{i(\frac{\pi}{3}+x)} c_1^\dagger \\
[c_3, H] &= -e^{\frac{i\pi}{3}} c_2 - e^{\frac{i\pi}{3}} c_2^\dagger + e^{-\frac{i\pi}{3}} c_1^\dagger - e^{-i(\frac{\pi}{3}+x)} c_1
\end{aligned} \tag{2.22}$$

Therefore

$$\begin{aligned}
[c_2 - c_2^\dagger, H] &= (1 - e^{-ix}) c_1 + (1 - e^{ix}) c_1^\dagger \\
\left[ \left( e^{\frac{i\pi}{6}} c_3 - e^{-i\frac{\pi}{6}} c_3^\dagger \right), H \right] &= e^{\frac{i\pi}{6}} (1 - e^{-i(\frac{\pi}{3}+x)}) c_1 + e^{-\frac{i\pi}{6}} (1 - e^{i(\frac{\pi}{3}+x)}) c_1^\dagger
\end{aligned} \tag{2.23}$$

However, the ratio between the coefficients of  $c_1$  or  $c_1^\dagger$  in the two commutators above is purely real:

$$-\frac{1 - e^{-ix}}{e^{\frac{i\pi}{6}} (1 - e^{-i(\frac{\pi}{3}+x)})} = -\frac{2 - 2\cos x}{e^{\frac{i\pi}{6}} (1 - e^{-i(\frac{\pi}{3}+x)}) (1 - e^{ix})} = \frac{1 - \cos x}{\cos(x + \frac{\pi}{6}) - \frac{\sqrt{3}}{2}} \tag{2.24}$$

Thus the following Majorana operator commutes with the Hamiltonian and is the second MZM:

$$\begin{aligned}
\tilde{b}_{23} &\equiv -iN \left( \left[ \cos\left(x + \frac{\pi}{6}\right) - \frac{\sqrt{3}}{2} \right] (c_2 - c_2^\dagger) + (1 - \cos x) \left( e^{\frac{i\pi}{6}} c_3 - e^{-\frac{i\pi}{6}} c_3^\dagger \right) \right) \\
&= N \left( \left[ \cos\left(x + \frac{\pi}{6}\right) - \frac{\sqrt{3}}{2} \right] b_2 + (1 - \cos x) \left( \frac{1}{2} a_3 + \frac{\sqrt{3}}{2} b_3 \right) \right)
\end{aligned} \tag{2.25}$$

where  $N$  is a normalization factor. When  $x = 0$  only the first term survives since

$$\lim_{x \rightarrow 0} \frac{1 - \cos x}{\cos(x + \frac{\pi}{6}) - \frac{\sqrt{3}}{2}} = 0 \tag{2.26}$$

while when  $x = -\frac{\pi}{3}$  only the second term survives. So  $\tilde{b}_{23}$  continuously evolves from  $b_2$  to  $\frac{1}{2}a_3 + \frac{\sqrt{3}}{2}b_3$  along the path  $\phi_1 \rightarrow \phi_2$ .

### Many-body Berry phase calculation for the 3-site Kitaev triangle

In this section we provide details for calculating the many-body Berry phase for braiding two MZM in the Kitaev triangle, as shown in Fig. 2 in the main text. To start we use the Hamiltonian Eq. (1) in the main text,

$$\mathcal{H} = \sum_{\langle jl \rangle} (-te^{i\phi_{jl}} c_j^\dagger c_l + \Delta e^{i\theta_{jl}} c_j c_l + \text{h.c.}) - \sum_j \mu c_j^\dagger c_j, \quad (2.27)$$

and write the creation and annihilation operators in the following Fock space basis for three spinless fermions

$$\begin{aligned} (|0\rangle, |1\rangle, \dots, |7\rangle) &\equiv \{|n_1, n_2, n_3\rangle\} \\ &= (|0, 0, 0\rangle, \\ &\quad |1, 0, 0\rangle, |0, 1, 0\rangle, |0, 0, 1\rangle, \\ &\quad |0, 1, 1\rangle, |1, 0, 1\rangle, |1, 1, 0\rangle, \\ &\quad |1, 1, 1\rangle) \end{aligned}$$

The creation(annihilation) operators in this space are defined as

$$\begin{aligned} c_j^\dagger |n_1, \dots, n_j, \dots\rangle &= \sqrt{n_j + 1} (-1)^{s_j} |n_1, \dots, n_j + 1, \dots\rangle, \\ c_j |n_1, \dots, n_j, \dots\rangle &= \sqrt{n_j} (-1)^{s_j} |n_1, \dots, n_j - 1, \dots\rangle, \end{aligned} \quad (2.28)$$

where

$$s_j = \begin{cases} \sum_{l=1}^{j-1} n_l & j > 1 \\ 0 & j = 1 \end{cases} \quad (2.29)$$

For the initial configuration corresponding to  $\boldsymbol{\phi}_1$  in Eq. (6) of the main text, diagonalizing the  $8 \times 8$  BdG Hamiltonian in the above basis leads to two degenerate ground states that can be distinguished by the occupation number of the following fermion operator constructed from the two MZM at the two bottom vertices

$$c_M \equiv \frac{1}{2}(a_1 + ib_2), \quad n_M \equiv c_M^\dagger c_M \quad (2.30)$$

The two degenerate ground states for the initial configuration, denoted as  $|0\rangle_i$  and  $|1\rangle_i$ , therefore satisfy

$$n_M |0\rangle_i = 0, \quad (2.31)$$

$$n_M |1\rangle_i = |1\rangle_i$$

In practice, we first construct the operator  $R_{\text{gs}}$  as a  $8 \times 2$  matrix by combining the two column eigenvectors of the two lowest-energy eigenstates of the initial BdG Hamiltonian:

$$R_{\text{gs}} \equiv (\psi_i, \psi'_i) \quad (2.32)$$

and then diagonalize the projected  $n_M$  operator:

$$U_n^\dagger (R_{\text{gs}}^\dagger n_M R_{\text{gs}}) U_n \equiv R_i^\dagger n_M R_i = \begin{pmatrix} 0 & \\ & 1 \end{pmatrix} \quad (2.33)$$

To carry out the Berry phase calculation we next need to adiabatically “rotate” the vector potential field by following the linearly interpolated closed parameter path described in the main text, which is discretized into  $N + 1$  segments. At any given point labeled by  $j$  along the path, we diagonalize the corresponding Hamiltonian and construct the projection operator  $P_j$  using the two lowest-energy eigenvectors  $\psi_j, \psi'_j$ :

$$P_j \equiv \psi_j \otimes \psi_j^\dagger + \psi'_j \otimes \psi'^{\dagger}_j \quad (2.34)$$

where  $\otimes$  means tensor product. The  $2 \times 2$  Berry phase matrix  $M_{f \leftarrow i}$  for the given parameter path is then obtained as

$$M_{f \leftarrow i} = \lim_{N \rightarrow \infty} R_f^\dagger P_N P_{N-1} \dots P_1 R_i \quad (2.35)$$

where  $R_f = R_i$  since the path is closed.

By using a large enough  $N$  we found the converged  $M_{f \leftarrow i}$  matrix has only diagonal elements being nonzero, meaning the braiding only changes each ground state by a scalar phase factor. Their values are  $(M_{f \leftarrow i})_{00} = e^{i0.118\pi}$  and  $(M_{f \leftarrow i})_{11} = e^{-i0.382\pi} = e^{i(0.118-0.5)\pi}$ .

We end this section by noting that the parameter path considered for the 3-site Kitaev triangle above is not equivalent to rotating a staggered vector potential but to separately manipulating the Peierls phases along the three edges. We have also done calculations for the latter case and found the two lowest-energy states fail to be degenerate everywhere along the parameter path, leading to non-standard relative Berry phases between the two initial states.

### Corner MZM in finite-width hollow triangles

A model that is closer to a realistic hollow triangular island is the finite-width triangular chain or ribbon. An example, illustrated in Figure 2.7 (d), has its edge length  $L = 80$  and width  $W = 3$ . The Hamiltonian for a single ribbon parallel to  $\hat{\mathbf{x}}$  is constructed and Fourier transformed

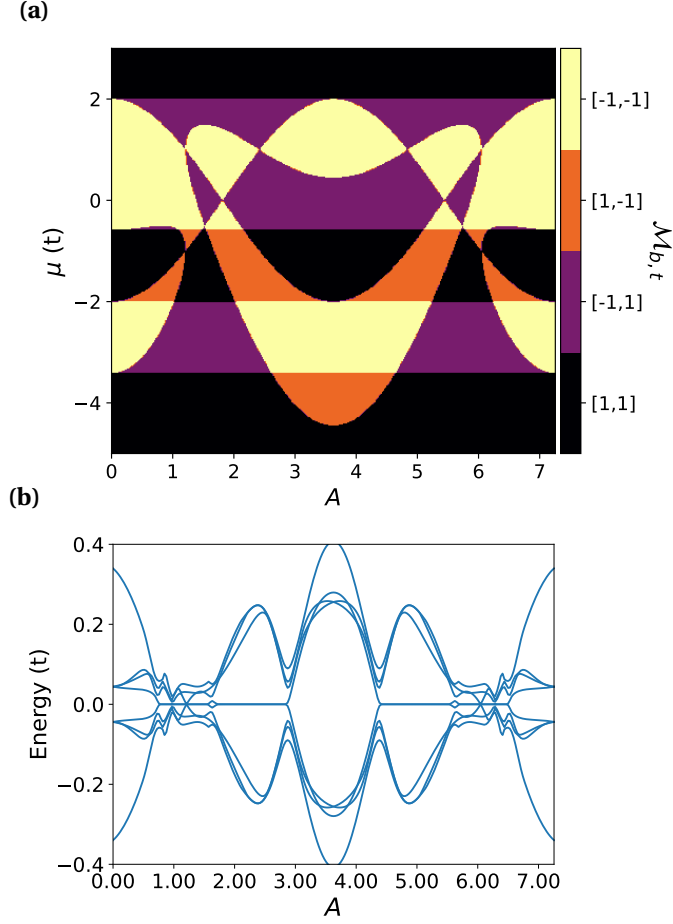


**Figure 2.6:** (a) Topological phase diagram for a  $W = 3$  hollow triangle obtained by overlapping the  $\mathcal{M}_{b,t}(A, \mu)$  plots of 1D chains with  $\mathbf{A} = A\hat{\mathbf{y}}$  and  $\mathbf{A} = A(\frac{\sqrt{3}}{2}\hat{\mathbf{x}} + \frac{1}{2}\hat{\mathbf{y}})$ . Color scheme: purple— $[\mathcal{M}_b, \mathcal{M}_t] = [1, 1]$ , yellow— $[\mathcal{M}_b, \mathcal{M}_t] = [-1, -1]$ , red— $[\mathcal{M}_b, \mathcal{M}_t] = [-1, 1]$ , orange— $[\mathcal{M}_b, \mathcal{M}_t] = [1, -1]$  (b) Near-gap BdG eigen-energies vs  $A$  for a finite triangle with edge length  $L = 80$ ,  $W = 3$ , and  $\mu = 1.6$ .

in the way described in the main text and has the following block form up to a constant

$$\mathcal{H} = \frac{1}{2} \sum_k \Psi_k^\dagger \begin{pmatrix} h_t(k) & h_\Delta(k) \\ h_\Delta^\dagger(k) & -h_t^*(-k) \end{pmatrix} \Psi_k \quad (2.36)$$

where  $\Psi_k \equiv (c_{k,1}, \dots, c_{k,W}, c_{-k,1}^\dagger, \dots, c_{-k,W}^\dagger)^T$ .  $h_t(k)$  is a  $W \times W$  Hermitian tridiagonal matrix with  $(h_t)_{n,n} = -2t \cos(k + \mathbf{A} \cdot \mathbf{a}_1) - \mu$  and  $(h_t)_{n,n+1} = -t(e^{i(-k + \mathbf{A} \cdot \mathbf{a}_3)} + e^{i\mathbf{A} \cdot \mathbf{a}_2})$  (here  $\mathbf{a}_3 \equiv -\mathbf{a}_1 + \mathbf{a}_2$ ).  $h_\Delta(k)$  is a  $W \times W$  tridiagonal matrix with  $(h_\Delta)_{n,n} = -2i\Delta \sin k$  and  $(h_\Delta)_{n,n\pm 1} = \mp \Delta [e^{-i(\pm k + \frac{2\pi}{3})} + e^{-i\frac{\pi}{3}}]$ .



The phase diagram Fig. 2.6 (a) is created in a similar way as that in Fig. 3 (b) of the main text, assuming a constant vector potential along  $\hat{y}$  and infinitely long  $W = 3$  ribbons. The spectral flow for the actual triangle with  $\mu = 1.6$  in Fig. 2.6 (b) shows MZM in the parameter regions in agreement with the phase diagram. Fig. 2.6. The MZM wavefunctions for  $A = 0.83$  and  $\mu = 1.6$ , illustrated in Fig. 2.7 (d), are indeed well localized at the bottom corners.

We next discuss how to move the MZM on a hollow triangle by rotating the vector potential. Due to the Peierls phase accumulated by hopping that is not parallel with the finite-width ribbon edges, the vector potential has a more complex effect on the energy spectrum here than that for the  $W = 1$  case. To ensure that the bulk band gap of individual edges only closes at a few isolated topological phase transition points, we plot in Figure 2.7 (b) the smallest gap of the three edges with periodic boundary condition versus  $(A, \varphi)$  when  $\mu = 1.6$ . A relatively clean region can be identified when  $A \in (0.75, 0.8)$ . Further taking into account the topological phase diagram Fig. 2.7 (a) obtained in a similar way as Fig. 4 (a) in the main text, we chose a parameter path on the  $(A, \varphi)$  plane that linearly interpolates the following points:

$$(A, \varphi) = (0.83, 0) \rightarrow \left(0.77, \frac{\pi}{6}\right) \rightarrow \left(0.83, \frac{\pi}{3}\right) \rightarrow \left(0.77, \frac{\pi}{2}\right) \quad (2.37)$$

The phase diagram indicates that along this path, the nontrivial  $\mathcal{M} = -1$  phase crawls through the three edges in a clockwise manner. Such a path ensures that only one edge undergoes a topological phase transition at a time. Then in the actual triangle the bulk gap will stay open due to finite size effect as a MZM moves across an edge without hybridizing with the other MZM.

To support this claim, we plot in Fig. 2.7 (c) the spectral flow for a finite triangle with  $L = 80$ ,  $W = 3$ ,  $\mu = 1.6$  and the above parameter path. The bulk gap is indeed open throughout the path, and the degeneracy of the two MZM also stays intact. The wavefunctions of the MZM at representative points along the path are plotted in panels (d-g) in the same order as that marked in panel (c). The locations of the MZM are also consistent with that inferred from the topological phase diagram.

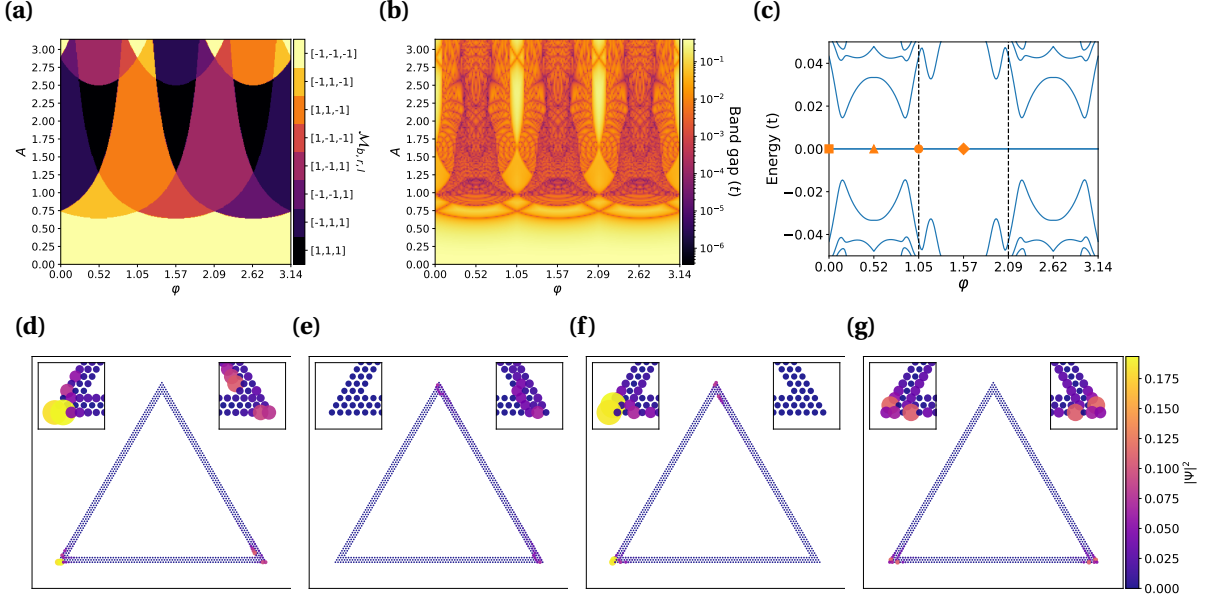


**Figure 2.7:** (a) Topological phase diagram for three  $W = 3$  ribbons corresponding to the three edges of a hollow triangle. ( $\mu = 1.6$  in all panels.) (b) Minimum of the bulk gaps of the three ribbons plotted on the  $(A, \varphi)$  plane. (c) Spectral flow of a hollow triangle with  $W = 3, L = 80$ , and the parameter path given in Eq. (2.37). (d-g) BdG eigenfunction  $|\Psi|^2$  summed over the two zero modes at  $\varphi = 0, \frac{\pi}{6}, \frac{\pi}{3}, \frac{\pi}{2}$ , respectively.

### Braiding MZM in a small network of triangles

In this section we show that one can braid two out of four MZM, a minimal setting for non-trivial manipulation of the degenerate many-body ground states, by using a small network of corner-sharing triangles. We focus on the critical step of swapping  $\gamma_2$  and  $\gamma_3$  as labeled in Fig. 5 of the main text. This can be done by rotating the vector potential of the triangle in the middle of the bottom row from  $\varphi = \frac{\pi}{6}$  to  $\frac{\pi}{3}$ . More specifically, when  $\varphi = \frac{\pi}{6}$ , with the chosen values of  $\mu$  and  $A$ , only the right edge of the said triangle is topologically nontrivial. The chain that hosts  $\gamma_{3,4}$  thus extends through this nontrivial edge to the top triangle as in Fig. 2.8 (b). On the other hand, when  $\varphi$  increases to  $\frac{\pi}{3}$ , the nontrivial edge of the middle triangle changes from right to left, which leads to  $\gamma_2$  hopping from its left corner to the right through the top corner, while  $\gamma_3$  is unaffected [Figs. 2.8 (c-g)]. As a result the  $\gamma_2, \gamma_3$  swapping is done without closing the bulk gap, as can be seen from the spectral flow in Fig. 2.8 (a).

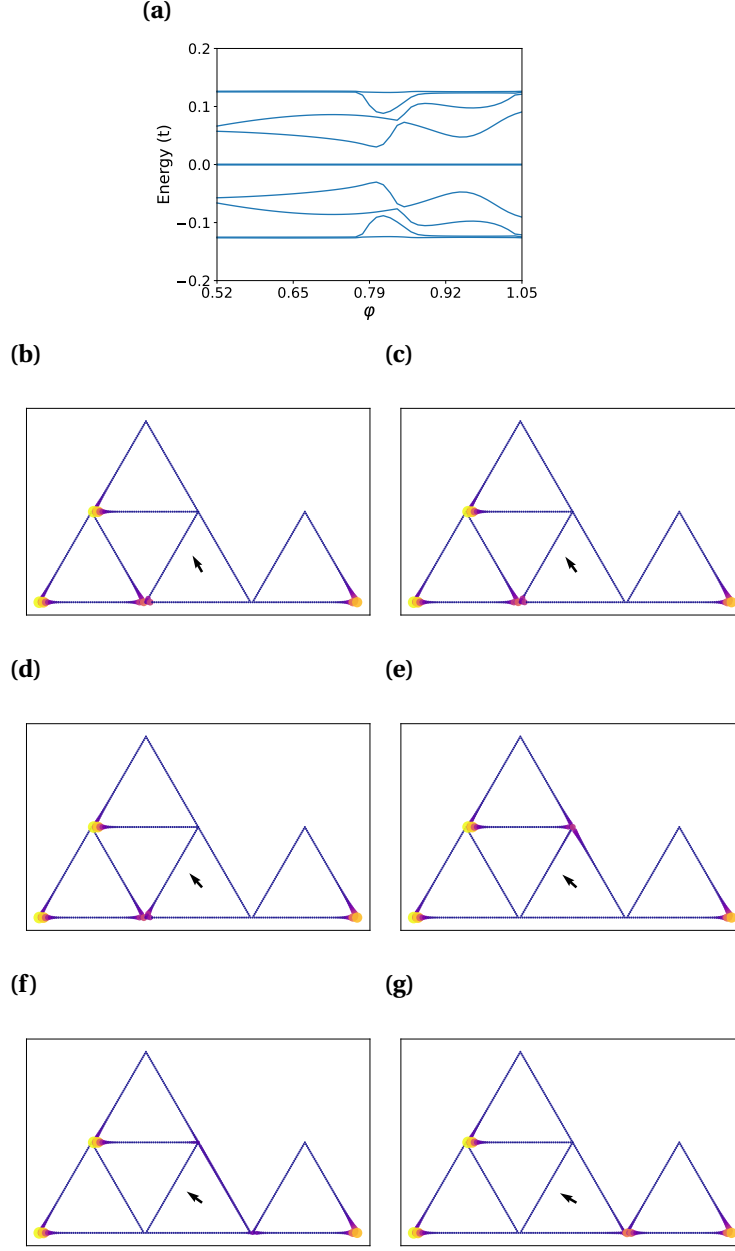


**Figure 2.8:** (a) Spectral flow for the critical step of swapping  $\gamma_2$  and  $\gamma_3$  in the example of Fig. 5 in the main text, calculated using four corner-sharing triangles of  $W = 1$  and  $L = 50$ , with  $\mu = 1.6$  and  $A = 2.6$ . Vector potential for the middle triangle in the bottom row can rotate according to  $\mathbf{A} = A(-\sin \phi \hat{\mathbf{x}} + \cos \phi \hat{\mathbf{y}})$  from  $\phi = \frac{\pi}{6}$  to  $\frac{\pi}{3}$ , while the other three have fixed  $\phi = 0$ . (b)-(g) BdG eigenfunction  $|\Psi|^2$  summed over the four zero modes at equally-spaced points along the rotation path. The black arrow indicates the direction of the vector potential for the bottom middle triangle.

## Chapter 3

# Landau Level-Like Topological Floquet Hamiltonians

### 3.1 Introduction

The quantum Hall effect (QHE) in conventional two-dimensional electron gas (2DEG) is one of the most remarkable phenomena in condensed matter physics [72]. This effect arises when a uniform external perpendicular magnetic field quantizes the electron energy spectrum into discrete Landau levels (LLs). Subject to a strong magnetic field, the diagonal (longitudinal) electric conductivity is vanishingly small, while the nondiagonal (Hall) conductivity is quantized. This happens when the Fermi energy lies in the gap between two LLs, referred to as integer QHE as the Hall conductivity takes values of  $-Ce^2/h$  with integer  $C$ , being the number of occupied bands below the Fermi energy [73]. Recent experimental realization of graphene has stimulated additional interest to explore QHE in two dimensional systems [73–75].

This significant effect is important to explore in Floquet systems [76, 77] because one may observe new phases in an alternative venue that can be experimentally realized [78–83]. Time periodically modulated Floquet theory has been extensively studied and well established for a large class of systems [77, 84–88]. One can then employ the high frequency expansions [77, 87–94] such as the well known Floquet-Magnus expansion [92–95] and Van Vleck expansion [77, 87], to analyze these effects. The significant difference is the latter provides an explicit formula for the time evolution operator starting at initial time  $t_0 = 0$  rather than former starting with finite time  $t_0$ , as seen in appendix B.3. In nonequilibrium systems, circularly polarized laser light can drive transitions that induce nontrivial topological phases, even in materials that are topologically trivial in equilibrium [96].

Optical manipulation of electronic properties has been emerging as a promising way of exploring novel phases [97, 98]. This leads to Floquet-Bloch states exhibiting emerging physical properties that are otherwise inaccessible in equilibrium [99]. Examples include Floquet

Chern insulator [100], Floquet topological insulators [101], Floquet notion of magnetic and other strongly-correlated phases [101], manipulation of topological antiferromagnet [102], topological classifications, symmetry-breaking concept, and symmetry protected topological phases in nonequilibrium quantum many-body systems [101, 103]. However, it is important to note that these studies have been demonstrated in the presence of time-periodic homogeneous laser lights. The role of spatially inhomogeneous laser light [104–108] remains largely unexplored.

In this work, we demonstrate that QHE can be observed in Floquet systems without need of a uniform magnetic field. We show that three linearly polarized lights are an effective and versatile way of realizing QHE, both in graphene-like 2D systems or in conventional 2DEGs. Additionally, two of the lights need to be spatially inhomogeneous and mirror one another to create a standing wave on the material. Employing Floquet theory, we rely on the standard degenerate perturbation formalism and use the Van Vleck expansion B.3 [77, 87] to derive an effective Hamiltonian and corresponding bandstructure in the long wavelength limit. We leverage high-refractive index materials [109] to enhance the effective magnetic fields and energy bandstructure. Our work provides new platforms for realizing QHE and related novel phases in nonequilibrium systems.

## 3.2 Floquet Landau level-like bands in Dirac systems

In this section we demonstrate a Dirac system in the presence of a standing, non-uniform, circularly polarized light becomes an effective Dirac Hamiltonian with a magnetic field that is composed of the electric field component of light. Dirac electrons can be represented with a generic model 2D Hamiltonian honeycomb monolayer in the presence of a gauge potential as

$$\mathcal{H}(t) = v_F \boldsymbol{\sigma} \cdot (\mathbf{p} + e\mathbf{A}(t)), \quad (3.1)$$

where  $\mathbf{A}$  is the gauge potential,  $\mathbf{p}$  is the momentum operator,  $v_F$  is the Fermi velocity of Dirac fermions,  $e$  is electron charge, and  $\boldsymbol{\sigma}$  the Pauli matrices vector in 2D. The light is made of three linearly polarized lasers, as shown in Fig. 3.1. Where the first is normally incident in the  $z$ -axis

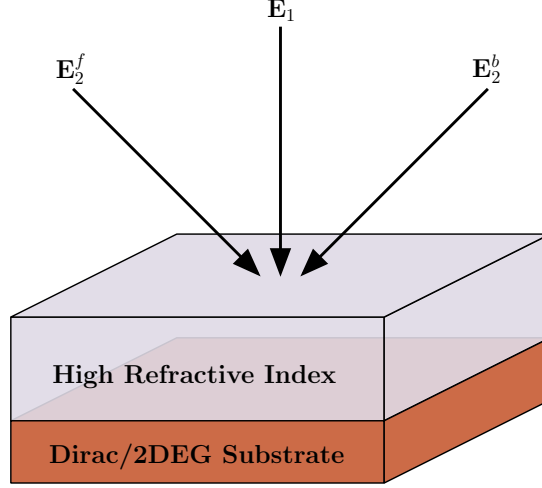


**Figure 3.1:** Schematic of two oblique (forward and backward) and one normally incident light on graphene or a 2DEG substrate with high refractive index material on top. Oblique lasers have polarization in  $y$ -axis and travel in  $xz$ -plane and normally incident laser has polarization in the  $x$ -axis and travel in  $yz$ -plane. With beam width large enough to cover the device fully.

with polarization in the  $x$ -axis. The second and third are of oblique incidence in the  $xz$ -plane, to acquire non-uniformity in the  $x$ -axis, with polarization in the  $y$ -axis, and mirrored about the  $yz$ -plane. This is to introduce  $x$ -dependence with the  $p_y$  term of the Dirac Hamiltonian. The relevant electric field components at the Dirac system interface are

$$\begin{aligned}\mathbf{E}_1 &= E \cos \omega t \hat{\mathbf{x}}, \\ \mathbf{E}_2 &= \mathbf{E}_2^f + \mathbf{E}_2^b = E \sin(Kx) \sin 2\omega t \hat{\mathbf{y}},\end{aligned}\tag{3.2}$$

Where  $\omega$  is angular frequency of the laser with time  $t$  and  $K = \omega \sin(\theta_i)/v_p$ , with  $\theta_i$  as incident angle of the oblique lasers and  $v_p$  is phase velocity of the lasers. Notice, the second electric field has twice frequency of the first, this allows for the second gauge potentials  $\sigma_y$  to have non-zero commutation with the first gauge potentials  $\sigma_x$ , and due to the high-frequency expansion used later, allows for the second gauge potential to return to a  $\sigma_y$ , as seen in [B.4.1](#). This form of the electric field relates to the following gauge potential, via  $\mathbf{E} = -\partial_t \mathbf{A}$  as

$$\mathbf{A}(t) = \frac{E}{\omega} \left\langle -\sin \omega t, \frac{1}{2} \sin(Kx) \cos 2\omega t \right\rangle, \quad (3.3)$$

Substituting Eq. (3.3) into Eq. (3.1), we arrive at

$$\mathcal{H}(t) = v_F \boldsymbol{\sigma} \cdot \mathbf{p} - \sigma_x \frac{v_F e E}{\omega} \sin \omega t - \sigma_y \frac{v_F e E}{2\omega} \sin(Kx) \cos 2\omega t. \quad (3.4)$$

Due to the laser's time-translation symmetry through  $A(t+T) = A(t)$  with  $T = 2\pi/\omega$ , one can apply the Floquet theory [66, 77, 87] and obtain an effective Hamiltonian from Eq. (3.4). This introduces the quasienergy matrix  $Q_{m,m+n} = H_n + m\hbar\omega\delta_{n0}$  after performing the Fourier time-transform of the Hamiltonian, given as

$$H_n = \frac{1}{T} \int_0^T \mathcal{H}(t) e^{-in\omega t} dt, \quad (3.5)$$

then we are left with modes  $m = 0, \pm 1, \pm 2$ . To use the high-frequency approximation we require  $\hbar\omega \gg H_{\pm 1, \pm 2}$ , the off-diagonal terms. After applying the high-frequency approximation to first and second order expansion in  $\hbar\omega$ , it leads to the zeroth-mode effective Hamiltonian in Eq. (3.4) as

$$H_{\text{eff}} = v_F \boldsymbol{\sigma} \cdot \mathbf{p} - \sigma_y \frac{v_F^3 e^2 E^2 p_y}{\hbar^2 \omega^4} + \sigma_y \frac{v_F^3 e^3 E^3 \sin(Kx)}{4\hbar^2 \omega^5} - \sigma_x \frac{v_F^3 e^2 E^2 \{p_x, \sin^2(Kx)\}}{8\hbar^2 \omega^4}. \quad (3.6)$$

The derivation can be found in the Appendix B.4.1. This effective Hamiltonian can be simplified in the long wavelength limit,  $Kx \ll 1$  to

$$\mathcal{H}_{\text{eff}}^D = v_F \sigma_x p_x + v_F \sigma_y (C p_y + e B^D x), \quad (3.7)$$

where  $C = 1 - \left(\frac{v_F e E}{\hbar \omega^2}\right)^2$  and  $B^D = \frac{K v_F^2 e^2 E^3}{4\hbar^2 \omega^5}$ . Diagonalizing the Hamiltonian in Eq. (3.7), we obtained the eigenvalues for Dirac system as

$$\epsilon_n^D = \pm v_F^2 \sqrt{\frac{nK e^3 E^3}{2\hbar\omega^5}} \quad (3.8)$$

which is similar to graphene LLs spectrum in the limit of equal velocities. The effective magnetic field in the Dirac Hamiltonian achieves a highly degenerate energy spectrum similar to LLs. Unlike conventional LLs, the electron motion is not a cyclotron orbit but a potentially more complicated orbit, due to CPL inducing a Coulomb force in the material's 2D plane. In Eq. (3.6), the first order term in  $\hbar\omega$  leads to gap at the Dirac point in normally incident, circularly polarized light experiments [79, 81] and is zero here due to the non-uniformity nature of oblique incident lasers.

There are several ways to enhance the effective magnetic field and directly LL-like energies for a Dirac system. Electric field strength can be increased within reason as we are limited by the photon energy to ensure the high-frequency expansion holds,  $E \ll 2\hbar\omega^2/ev_F$ . One can reasonably use electric field strengths up to 20% of the limit due to photon energy. The laser wavenumber  $K = \omega \sin(\theta_i)/v_p$  has a linear relationship to photon energy, too. Overall, considering the high-frequency limit on the electric field, the effective field  $B^D \propto \omega^2 \sin(\theta_i)/(v_F v_p)$ . Without too much consequence the incident angle can be increased up to  $\pi/2$  and decreasing the phase velocity of light would enhance the effective magnetic field. Increasing photon energy is one way to enhance the effective magnetic field. As considered in previous literature, when photon energy and electric field are increased more energy is pumped into the system, shorter pulses are required to prevent damaging the system [79, 81].

### 3.3 Floquet Landau level-like bands in 2DEG systems

In this section we show a 2DEG system with a standing, non-uniform, circularly polarized light becomes an effective 2DEG Hamiltonian with an effective magnetic field composed of the electric field component of light. We consider the case of Schrodinger charged particles in the



presence of a gauge potential as

$$\mathcal{H}(t) = \frac{1}{2m^*} (\mathbf{p} + e\mathbf{A}(t))^2 \quad (3.9)$$

where  $m^*$  is the effective charge mass. We again consider a similar setup with three linearly polarized lasers. The relevant electric field components at the 2DEG interface are

$$\begin{aligned} \mathbf{E}_1 &= E \cos \omega t \hat{\mathbf{x}}, \\ \mathbf{E}_2 &= \mathbf{E}_2^f + \mathbf{E}_2^b = -E \cos(Kx) \sin \omega t \hat{\mathbf{y}}. \end{aligned} \quad (3.10)$$

Unlike the Dirac system, all lasers have the same frequency. This ensures a LL-like behavior from the nonzero commutation of  $x$  and  $p_x$  terms during the high-frequency expansion. The electric field relates to the following gauge potential, via  $\mathbf{E} = -\partial_t \mathbf{A}$  as

$$\mathbf{A}(t) = \frac{E}{\omega} \langle -\sin \omega t, \cos(Kx) \cos \omega t \rangle. \quad (3.11)$$

Substituting Eq. (3.11) into Eq. (3.9), we arrive at

$$\begin{aligned} \mathcal{H}(t) &= \frac{1}{2m^*} \left[ p_x^2 + p_y^2 + \frac{e^2 E^2}{2\omega^2} (1 - \cos 2\omega t) + \frac{e^2 E^2}{2\omega^2} (1 + \cos 2\omega t) \cos^2(Kx) \right. \\ &\quad \left. + \frac{2eE}{\omega} (p_y \cos(Kx) \cos \omega t - p_x \sin \omega t) \right]. \end{aligned} \quad (3.12)$$

Again, due to laser's time-translation symmetry we can apply the Floquet theory, which includes computing the Fourier time-transform using Eq. (3.5). This leaves us with modes  $m = 0, \pm 1, \pm 2$ . In the high-frequency expansion we still require  $\hbar\omega \gg H_{\pm 1, \pm 2}$ . After applying the high-frequency approximation to first order in  $\hbar\omega$ , it leads to the zeroth-mode effective Hamiltonian as

$$\mathcal{H}_{\text{eff}} = \frac{1}{2m^*} \left[ p_x^2 + \left( p_y - \frac{Ke^2E^2 \sin(Kx)}{m^*\omega^3} \right)^2 + \frac{e^2E^2 \cos^2(Kx)}{\omega^2} - \frac{K^2e^4E^4 \sin(Kx)}{m^{*2}\omega^6} \right].$$

where we shifted a constant energy out of the effective Hamiltonian and completed the square for the  $p_y$  and  $x$  terms. Here we can see the high-frequency expansion terms  $H^{F(1)}$  and  $H^{F(2)}$ , as shown in B.3, introduce a periodic potential in the  $x$ -direction, this can be cancelled out by applying an external periodic potential of the same strength and wavenumber in the  $x$ -direction. Finally, in the long wavelength,  $Kx \ll 1$ ,

$$\mathcal{H}_{\text{eff}}^{2\text{DEG}} = \frac{1}{2m^*} \left[ p_x^2 + (p_y - eB^{2\text{DEG}}x)^2 \right], \quad (3.13)$$

with  $B^{2\text{DEG}} = \frac{K^2eE^2}{m^*\omega^3}$ . The energy spectrum values are

$$\epsilon_n^{2\text{DEG}} = \frac{\hbar K^2 e^2 E^2}{m^{*2} \omega^3} \left( n + \frac{1}{2} \right), \quad (3.14)$$

which is similar to 2DEG LLs spectrum. This is another highly degenerate LL-like spectrum due to an effective magnetic field induced by the combination of lasers provided.

The 2DEG system has the same ways to enhance its effective magnetic field and energy spectrum. First, the electric field is limited by the high-frequency expansion, we find  $E \ll (8m^*\hbar\omega^3/e^2)^{1/2}$  to be a reasonable cutoff. The effective field  $B^{2\text{DEG}} \propto \omega^2 \sin^2(\theta_i)/v_p^2$ , is similar to the Dirac system. For a 2DEG system, the enhancement to the effective magnetic field follows a squared dependence on the incident angle and phase velocity, differing from the Dirac case, where it scales linearly and by Fermi velocity. Similarly, increasing the photon energy is one way to enhance the effective magnetic field, with the requirement of using shorter pulses as photon energy and electric field increase.

### 3.4 Conclusion

We now examine the topology of both systems. Eqs. (3.7) and (3.13) are in LL Hamiltonian form, and typically exhibit QHE. The two systems only have translational symmetry in the  $y$ -axis, so a Chern number based on periodicity in  $k_x$  and  $k_y$  is not applicable, though one can relate the center of mass of an electron to the Chern number as shown in Appendix B.7, which is related to the Laughlin pump. Considering the Laughlin pump argument, both systems have quantized Hall conductivity, since both have the same eigenstates as their respective LL Hamiltonian. A key difference to note about both systems is the  $C$  term in Eq. (3.7). This term will stay positive for the values of  $E$  used in the high-frequency limit for the Dirac case.

Using existing experiments [79, 81] we can provide an estimate for the strength of the effective magnetic field to observe LL-like spectrum and QHE. Analytical structure of Eq. (3.8) and Eq. (3.14) are primarily responsible for the LL-like spectrum in both the Dirac and 2DEG systems, respectively. Although such results are valid for other 2D materials or Schrödinger systems, however, for simplicity, we will consider parameters realized for graphene or topological insulators [79, 81]. We will consider a similar range of mid-IR photon energies (or  $\lambda = [3\mu\text{m}, 10\mu\text{m}]$ ) as seen in graphene or topological insulators [79, 81] to match with recently proposed high refractive index metamaterial composites [109]. In these experiments [79, 81], the strength of the electric field used is  $1 \times 10^7$  V/m to  $1 \times 10^8$  V/m, for the parameters used to estimate effective magnetic fields for both systems the largest electric field is around  $1.4 \times 10^8$  V/m. As should be considered, the larger both photon energy and electric field become ultrafast pulses should be used to prevent thermal damage to materials, on the order of 500 fs. To note, for the following results we assume a high oblique angle to let  $\sin(\theta_i) \approx 1$ .

To enhance the effective magnetic field, aside from using higher photon energy, reducing the photon phase velocity can see a considerable increase in both systems. The refractive index materials can be set above graphene, or any Dirac material, such that the lasers can propagate through to reduce its phase velocity. Germanium refractive index increases monotonically with increasing photon energy, we use a linear interpolation of the refractive index due the small

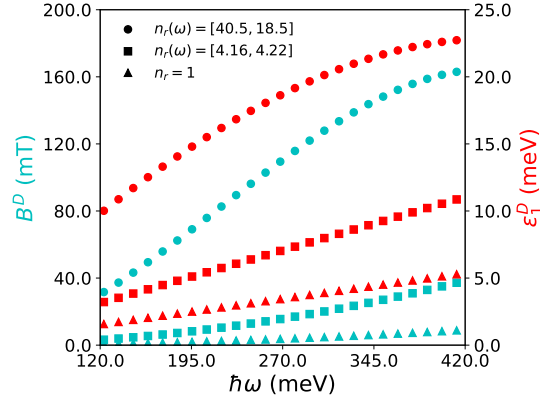


**Figure 3.2:** Effective magnetic field (cyan) and first quasienergy (red) as a function of photon energy for various refractive materials: vacuum (triangles), germanium (squares), and Al-composite metamaterial (circles).

change for the range of photon energies used. Al-composite metamaterials refractive index is monotonically decreasing with increasing photon energy and we use a linear interpolation here as the data is roughly linear.

In case of a Dirac system Fig. 3.2 shows graphene with various refractive index materials to enhance the effective magnetic field and first order quasienergy of the LL-like spectrum. For mid-IR ranges of lasers, the effective magnetic field (cyan) can get up to 8.8 mT for vacuum, 37.2 mT for germanium, and 163 mT for Al-composite metamaterial for  $\hbar\omega = 413$  meV and results in first order quasienergies (red) of 5.3 meV, 11 meV, and 23 meV, respectively. As can be seen in 3.2 as photon energy increases the Al-composite refractive index decreases quite a bit and if we used higher energy we would see the effective magnetic field and quasienergies start to decrease, as will be seen with 2DEG. While the material has higher index of refraction overall, it would be better to find a material that increases refractive index with photon energy, like germanium can, for it can drastically increase for slightly higher photon energies before effective magnetic field dips [110].

For 2DEG systems Fig. 3.3 shows GaAs and InSb materials with the same refractive materials used for graphene to enhance effective magnetic field and zeroth order quasienergy of the LL-like spectrum. The vacuum and germanium interfaces are scaled up by a factor of 10 and 50,

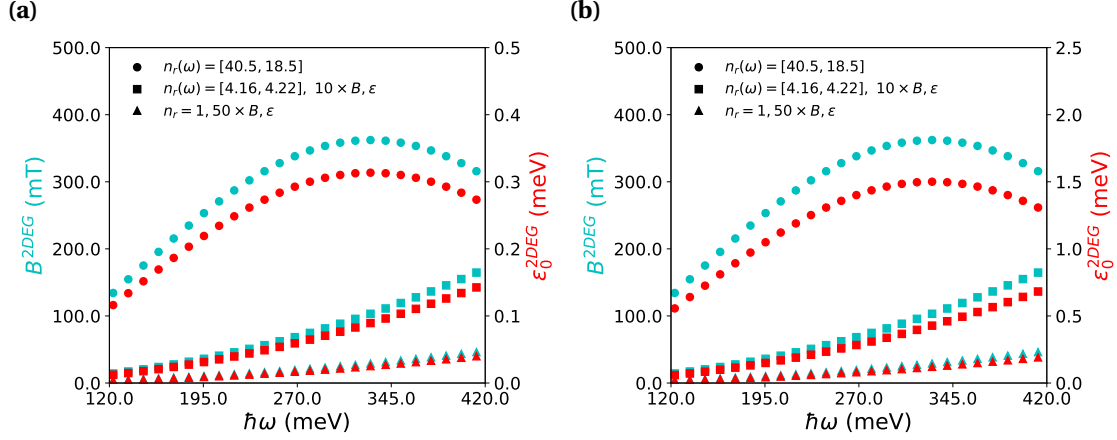


**Figure 3.3:** Effective magnetic field (cyan) and first quasienergy (red) as a function of photon energy for 2DEGs for various refractive materials: vacuum (triangles) scaled by a factor of 50, germanium (squares) scaled by a factor of 10, and Al-composite metamaterials. The 2DEG materials used are (a) GaAs and (b) InSb.

respectively, to visually enhance and compare it to the Al-composite interface. GaAs is used as it is one of the most common 2DEG with relatively small effective electron mass, followed by InSb since it has the smallest effective electron mass found in 2DEG materials. For the GaAs system, effective magnetic field (cyan) can get up to 0.92 mT for vacuum, 16.5 mT for germanium, and 362 mT for Al-composite metamaterial and achieves zeroth order quasienergies (red) of  $0.8 \mu\text{eV}$ ,  $14.3 \mu\text{eV}$ , and  $314 \mu\text{eV}$ , respectively. In the InSb system, effective magnetic field is the same as GaAs, since it has no dependence on effective mass, and achieves zeroth order quasienergies (red) of  $3.8 \mu\text{eV}$  for vacuum,  $68.2 \mu\text{eV}$  for germanium, and  $1.5 \text{ meV}$  for Al-composite. As alluded to earlier, due to Al-composites large decrease in refractive index for increasing photon energy, it peaks earlier around  $\hbar\omega = 328 \text{ mT}$ , for 2DEG. Overall, we see large changes in 2DEG for both effective magnetic field, due to being proportional to refractive index squared and quasienergies, being inversely proportional to effective electron mass.

There are a few items we did not consider for our calculations. First, we do not consider any effects due to a refractive index material in contact with a Dirac or 2DEG system. Secondly, while the high-frequency expansion limits the electric field applied to the materials one could still go beyond the limit of  $\hbar\omega \ll H_{pm1}, H_{\pm 2}$  to enhance the effective magnetic field by a few

orders of magnitude with some error. For example, if instead we use  $\hbar\omega = H_{\pm 1}, H_{\pm 2}$ , this would be multiplying the electric field by a factor of 5 from our calculations presented, Dirac effective magnetic field would increase by a factor of 125 while 2DEG effective magnetic field would increase by a factor of 25. For Dirac systems with higher electric field strengths, if  $C = 0$ , there would be no QHE as there is no coupling between  $x$  and  $p_y$ , and if  $C < 0$ , the direction of chirality flips.

In conclusion, we have shown Floquet LLs and the QHE using three linearly polarized lasers for Dirac and conventional 2DEG systems. While using these lasers, we need at least two polarized lasers to be spatially inhomogeneous and mirrored. We have presented results using frequency space expansion method and degenerate Floquet perturbation theory. While, a tight-binding model capable of using “low-frequency” with a Peierls substitution can be found in appendix B.5 and B.6, the results are difficult to interpret and currently not informative. The results agree well to show Floquet LL-like energies in experimentally accessible parameters range. Also, it is vital to note we are flexible to use different values of the electric field strength, photon energy, or phase velocity to realize QHE and control the strength of the effective magnetic field. Therefore, we think Floquet LL-like and QHE can be observed in experiments for moderate strength of the spatially inhomogeneous lasers. Moreover, we expect to open up new avenues for nanoelectronics in nonequilibrium systems.

# Chapter 4

## Conclusion

In this dissertation, we focused on gauge potentials as a key mechanism for tuning systems from trivial topology to non-trivial topology. One can either use minimal coupling to introduce a gauge potential in a continuum model or a Peierls phase in a tight-binding model. Both approaches are equivalent for slowly varying gauge potentials. This lends a lot of flexibility in tackling a Hamiltonian in either form, continuum or tight-binding. Another key aspect of gauge potentials is gauge invariance under a gauge transform. This allows us to transform a Hamiltonian into a basis that is more descriptive of the physics we are interested in.

In Chapter 2, we showed through a Peierls phase of a gauge potential in a superconducting tight-binding model in Majorana basis allows one to achieve non-trivial topology. We showed for a three lattice superconducting equilateral triangle one can apply a gauge potential as a step function exactly solves the Hamiltonian to have two MFs on two of the triangles three vertices. With a rotation of the gauge potential via a linear interpolation, we can keep the band gap from closing and rotate one MF at a time to the next vertex. Then, for larger triangular islands, as a chain or with finite thick edges, we can use bulk-edge correspondence to inform us which edge is trivial and non-trivial. Using a uniform gauge potential across the triangle showed, due to geometry and the gauge potential contributions, individual edges topology could be tuned from trivial to non-trivial topology. The phase diagrams showed there are swaths of tunable parameters to then make the topology crawl cw or ccw, without band gap closing, around the triangular island, effectively rotating two MFs around a triangle. With two options for hosting and rotating MFs we finally showed a minimal network of triangles to host and braid 4 MFs, which can be upscaled to increase the number of MFs for braiding operations. This opens up new routes to achieve fault-tolerant, topological quantum computing.

In Chapter 3, we showed through minimal coupling of a gauge potential, created from laser light, for both Dirac and 2DEG systems, one can induce LL-like spectrum and QHE. This used

Floquet theory and high-frequency expansion, and allows us to approximate an effective magnetic field as a function of electric field and arrive at LL-like Hamiltonians, to which we know the physics of in equilibrium systems. There are many tunable parameters to enhance the LL-like spectrum and QHE, from photon energy, electric field, phase velocity, incidence angle, to Fermi velocity or effective electron mass. The estimated values are achievable with current experimental setups found in previous literature and comparable with classic magnetic field QHE. These avenues open up new frontiers in nonequilibrium physics.



# Appendix A

## Superconducting Triangular Islands

### A.1 Kitaev chain

A pair of Majorana fermions can be defined in terms of spinless operators  $a_j, a_j^\dagger$ , where  $j$  labels general quantum numbers, as

$$c_{2j-1} = a_j + a_j^\dagger \tag{A.1}$$

$$c_{2j} = -i(a_j - a_j^\dagger)$$

which are hermitian conjugates of themselves. Conversely,

$$a_j = \frac{1}{2}(c_{2j-1} + i c_{2j}), \tag{A.2}$$

$$a_j^\dagger = \frac{1}{2}(c_{2j-1} - i c_{2j})$$

For a general mean-field Hamiltonian

$$H = \sum_{jl} h_{jl} a_j^\dagger a_l \tag{A.3}$$

where  $h$  is a Hermitian matrix, it can be transformed to the Majorana fermion representation as follows:

$$\begin{aligned}
H &= \frac{1}{4} \sum_{jl} h_{jl} (c_{2j-1} - i c_{2j}) (c_{2l-1} + i c_{2l}) \\
&= \frac{1}{4} \sum_{jl} (h_{jl} c_{2j-1} c_{2l-1} - i h_{jl} c_{2j} c_{2l-1} + i h_{jl} c_{2j-1} c_{2l} + h_{jl} c_{2j} c_{2l}) \\
&= \frac{i}{4} \sum_{jl} (c_{2j-1}, c_{2j}) \begin{pmatrix} -i h_{jl} & h_{jl} \\ -h_{jl} & -i h_{jl} \end{pmatrix} \begin{pmatrix} c_{2l-1} \\ c_{2l} \end{pmatrix} \\
&\equiv \frac{i}{4} \sum_{mn} A_{mn} c_m c_n
\end{aligned} \tag{A.4}$$

where the matrix  $A$  anti-Hermitian since

$$H^\dagger = -\frac{i}{4} \sum_{mn} A_{mn}^* c_n c_m = H \tag{A.5}$$

which leads to  $A_{mn}^* = -A_{nm}$ . If the Hamiltonian does not preserve particle number, i.e., it is a BdG Hamiltonian, we have, similarly

$$H = \sum_{jl} \left( h_{jl} a_j^\dagger a_l + \Delta_{jl} a_j a_l + \Delta_{jl}^\dagger a_j^\dagger a_l^\dagger \right) \tag{A.6}$$

supposing we do not double count the terms in the normal part of the Hamiltonian. Then

$$H = \frac{i}{4} \sum_{jl} (c_{2j-1}, c_{2j}) \begin{pmatrix} -i h - i(\Delta + \Delta^\dagger) & h + (\Delta - \Delta^\dagger) \\ -h + (\Delta - \Delta^\dagger) & -i h + i(\Delta + \Delta^\dagger) \end{pmatrix}_{jl} \begin{pmatrix} c_{2l-1} \\ c_{2l} \end{pmatrix} \tag{A.7}$$

On the other hand, the BdG Hamiltonian can be written as

$$\begin{aligned}
H &= \frac{1}{2} \sum_j h_{jj} + \sum_{jl} \left( \frac{1}{2} h_{jl} a_j^\dagger a_l - \frac{1}{2} h_{lj} a_j a_l^\dagger + \Delta_{jl} a_j a_l + \Delta_{jl}^\dagger a_j^\dagger a_l^\dagger \right) \\
&= \frac{1}{2} \text{Tr}(h) + \sum_{jl} (a_j^\dagger, a_j) \begin{pmatrix} \frac{1}{2} h & \Delta^\dagger \\ \Delta & -\frac{1}{2} h^T \end{pmatrix}_{jl} \begin{pmatrix} a_l \\ a_l^\dagger \end{pmatrix} \\
&\equiv \frac{1}{2} \text{Tr}(h) + a^\dagger \begin{pmatrix} \frac{1}{2} h & \Delta^\dagger \\ \Delta & -\frac{1}{2} h^T \end{pmatrix} a
\end{aligned} \tag{A.8}$$

where  $a \equiv (a_1, a_2, \dots, a_1^\dagger, a_2^\dagger, \dots)^T$ . Suppose the BdG Hamiltonian can be diagonalized by a Bogoliubov transformation:

$$\tilde{a}_j^\dagger = a_l^\dagger U_{1,lj} + a_k U_{2,kj} \tag{A.9}$$

$$\tilde{a}_j = a_l U_{1,lj}^* + a_k^\dagger U_{2,kj}^*$$

Preserving the anticommutation relation suggests

$$\begin{aligned}
\delta_{ij} &= \{\tilde{a}_i, \tilde{a}_j^\dagger\} = \{a_l U_{1,li}^* + a_k^\dagger U_{2,ki}^*, a_{l'}^\dagger U_{1,l'j} + a_{k'} U_{2,k'j}\} \\
&= U_{1,li}^* U_{1,l'j} + U_{2,ki}^* U_{2,k'j} = (U_1^\dagger U_1 + U_2^\dagger U_2)_{ij} \\
0 &= \{\tilde{a}_i, \tilde{a}_j\} = \{a_l U_{1,li}^* + a_k^\dagger U_{2,ki}^*, a_{l'} U_{1,l'j} + a_{k'}^\dagger U_{2,k'j}^*\} \\
&= U_{1,li}^* U_{2,l'j} + U_{2,ki}^* U_{1,k'j} = (U_1^\dagger U_2^* + U_2^\dagger U_1^*)_{ij} \\
0 &= \{\tilde{a}_i^\dagger, \tilde{a}_j^\dagger\} = \{a_l^\dagger U_{1,li} + a_k U_{2,ki}, a_{l'}^\dagger U_{1,l'j} + a_{k'} U_{2,k'j}\} \\
&= U_{1,li} U_{2,l'j} + U_{2,ki} U_{1,k'j} = (U_1^\dagger U_2^* + U_2^\dagger U_1^*)_{ij}^*
\end{aligned} \tag{A.10}$$

The above identities simply indicate

$$\mathcal{U} \equiv \begin{pmatrix} U_1 & U_2 \\ U_2^* & U_1^* \end{pmatrix} \quad (\text{A.11})$$

is a unitary matrix. Therefore one can diagonalize the BdG Hamiltonian using usual unitary matrices obtained from the eigenvectors of the matrix in the last line of Eq. A.74:

$$\begin{aligned} H &= \frac{1}{2} \text{Tr}(h) + \tilde{a}^\dagger U^\dagger \begin{pmatrix} \frac{1}{2}h & \Delta^\dagger \\ \Delta & -\frac{1}{2}h^T \end{pmatrix} U \tilde{a} \\ &\equiv \frac{1}{2} \text{Tr}(h) + \frac{1}{2} \tilde{a}^\dagger \begin{pmatrix} \epsilon & 0 \\ 0 & -\epsilon \end{pmatrix} \tilde{a} \\ &= \frac{1}{2} \sum_j h_{jj} + \frac{1}{2} \sum_j (\epsilon_j \tilde{a}_j^\dagger \tilde{a}_j - \epsilon_j \tilde{a}_j \tilde{a}_j^\dagger) \\ &= \frac{1}{2} \sum_j h_{jj} + \sum_j \epsilon_j (\tilde{a}_j^\dagger \tilde{a}_j - \frac{1}{2}) \end{aligned} \quad (\text{A.12})$$

where  $\epsilon \equiv \text{Diag}[\epsilon_1, \epsilon_2, \dots]$ . To see why  $U$  can transform the BdG Hamiltonian into such a diagonal matrix with opposite eigenvalues at the same positions in the upper-left and lower-right blocks, we check these two terms explicitly

$$\begin{aligned} &\frac{1}{2} (\epsilon_1 \tilde{a}_j^\dagger \tilde{a}_j - \epsilon_2 \tilde{a}_j \tilde{a}_j^\dagger) \\ &= \frac{\epsilon_1}{2} (a_l^\dagger U_{1,lj} + a_k U_{2,kj}) (a_{l'} U_{1,l'j}^* + a_{k'}^\dagger U_{2,k'j}^*) - \frac{\epsilon_2}{2} (a_{l'} U_{1,l'j}^* + a_{k'}^\dagger U_{2,k'j}^*) (a_l^\dagger U_{1,lj} + a_k U_{2,kj}) \\ &= \frac{1}{2} (\epsilon_1 U_{1,lj} U_{1,l'j}^* - \epsilon_2 U_{2,lj}^* U_{2,l'j}) a_l^\dagger a_{l'} + \frac{1}{2} (\epsilon_1 U_{2,kj} U_{2,k'j}^* - \epsilon_2 U_{1,kj}^* U_{1,k'j}) a_k a_{k'}^\dagger \\ &+ \frac{1}{2} (\epsilon_1 U_{1,lj} U_{2,k'j}^* - \epsilon_2 U_{2,lj}^* U_{1,k'j}) a_l^\dagger a_{k'}^\dagger + \frac{1}{2} (\epsilon_1 U_{2,kj} U_{1,l'j}^* - \epsilon_2 U_{1,kj}^* U_{2,l'j}) a_k a_{l'} \end{aligned} \quad (\text{A.13})$$

Comparing them with the original BdG Hamiltonian Eq. A.74, we can conclude that

$$\epsilon_1 U_{1,lj} U_{1,l'j}^* - \epsilon_2 U_{2,lj}^* U_{2,l'j} = -(\epsilon_1 U_{2,l'j} U_{2,lj}^* - \epsilon_2 U_{1,l'j}^* U_{1,lj}) \quad (\text{A.14})$$

$$\epsilon_1 U_{1,lj} U_{2,k'j}^* - \epsilon_2 U_{2,lj}^* U_{1,k'j} = (\epsilon_1 U_{2,k'j} U_{1,lj}^* - \epsilon_2 U_{1,k'j}^* U_{2,lj})^*$$

or equivalently

$$(\epsilon_1 - \epsilon_2)(U_{1,lj} U_{1,l'j}^* + U_{2,l'j} U_{2,lj}^*) = 0 \quad (\text{A.15})$$

$$0 = 0$$

The first equation therefore dictates  $\epsilon_1 = \epsilon_2$ . However, note that  $\epsilon_j$  does not have to be all positive. If the original normal state Hamiltonian can be diagonalized into a form

$$H = \sum_j \tilde{\epsilon}_j b_j^\dagger b_j \quad (\text{A.16})$$

where  $\tilde{\epsilon}_j$  can be either positive or negative, the state with the lowest possible energy from the system is

$$|\Omega\rangle = \prod_{\tilde{\epsilon}_k < 0} b_k^\dagger |0\rangle \quad (\text{A.17})$$

where  $|0\rangle$  is the true vacuum with no particles in any sense. This is the ground state, and its parity is therefore determined by the number of single-particle eigenstates that have negative energies.

From the same perspective, one can define the ground state of the BdG Hamiltonian Eq. A.12 for a specific set of Fermion operators  $\tilde{a}_j$ , as

$$|\Omega_{\text{BdG}}\rangle = \prod_{\epsilon_j < 0} \tilde{a}_j^\dagger |0_{\text{BdG}}\rangle \quad (\text{A.18})$$

where  $|0_{\text{BdG}}\rangle$  is certain “vacuum state” for the given set of  $\tilde{a}_j$ :

$$\tilde{a}_j |0_{\text{BdG}}\rangle = 0, \forall j \quad (\text{A.19})$$

The number of particles in the ground state is therefore determined by the number of negative  $\epsilon_j$ . However, the sign of  $\epsilon_j$  in the present case does not have absolute meaning. For example, supposing  $\epsilon_{j_0} < 0$ , the following Bogoliubov transformation

$$\tilde{a}'_{j_0} = \tilde{a}_{j_0}^\dagger \quad (\text{A.20})$$

$$\tilde{a}_{j_0}'^\dagger = \tilde{a}_{j_0}$$

that only interchanges the creation and annihilation operators for a single  $j_0$  and keeps the others unchanged, leads to a different ground state

$$|\Omega'_{\text{BdG}}\rangle = \prod_{\epsilon_j < 0, j \neq j_0} \tilde{a}_j^\dagger |0_{\text{BdG}}\rangle \quad (\text{A.21})$$

since the number of negative energy eigenstates decreases by one. The transformation in Eq. A.20 therefore neither preserves particle number nor particle parity. This can be explicitly checked. The particle number operator in the  $\tilde{a}_j$  representation is

$$N = \sum_j \tilde{a}_j^\dagger \tilde{a}_j \quad (\text{A.22})$$

Therefore

$$N' = \sum_{j \neq j_0} \tilde{a}_j^\dagger \tilde{a}_j + \tilde{a}_{j_0} \tilde{a}_{j_0}^\dagger = N + (1 - 2\tilde{a}_{j_0}^\dagger \tilde{a}_{j_0}) \quad (\text{A.23})$$

The latter equation also means that when the  $j_0$  state is occupied in  $\Omega_{\text{BdG}}$ , i.e.,  $\tilde{a}_{j_0}^\dagger \tilde{a}_{j_0} |\Omega_{\text{BdG}}\rangle = |\Omega_{\text{BdG}}\rangle$ , the transformation decreases the total number of particles by 1. Conversely, if it is un-

occupied ( $\epsilon_{j_0} > 0$ ), or  $\tilde{a}_{j_0}^\dagger \tilde{a}_{j_0} |\Omega_{\text{BdG}}\rangle = 0$ , the transformation increases the particle number by one.

The fermion parity operator can be defined by

$$P = \prod_j (1 - 2a_j^\dagger a_j) \quad (\text{A.24})$$

so that  $P = 1$  if the number of occupied states is even, and  $-1$  otherwise. Alternatively, since

$$a_j^\dagger a_j = \frac{1}{4}(c_{2j-1} - ic_{2j})(c_{2j-1} + ic_{2j}) = \frac{1}{2}(1 + ic_{2j-1}c_{2j}) \quad (\text{A.25})$$

$P$  can be written in the Majorana representation as

$$P = \prod_j (-ic_{2j-1}c_{2j}). \quad (\text{A.26})$$

Eq. [A.20](#) transforms  $P$  by changing

$$1 - 2\tilde{a}_{j_0}^\dagger \tilde{a}_{j_0} \rightarrow 1 - 2\tilde{a}'_{j_0} \tilde{a}'_{j_0}{}^\dagger = -(1 - \tilde{a}_{j_0}^\dagger \tilde{a}'_{j_0}) \quad (\text{A.27})$$

and hence indeed changes  $P$ .

We can also understand why the BdG Hamiltonian preserves  $P$  but not  $N$ . Due to the following commutation relations:

$$[a_j^\dagger a_l, a_j^\dagger a_j] = a_j^\dagger a_l a_j^\dagger a_j - a_j^\dagger a_j a_j^\dagger a_l = -a_j^\dagger a_l \quad (\text{A.28})$$

$$[a_j^\dagger a_l, a_l^\dagger a_l] = a_j^\dagger a_l a_l^\dagger a_l - a_l^\dagger a_l a_j^\dagger a_l = a_j^\dagger a_l$$

$$[a_j^\dagger a_l^\dagger, a_j^\dagger a_j] = a_j^\dagger a_l^\dagger a_j^\dagger a_j - a_j^\dagger a_j a_j^\dagger a_l^\dagger = -a_j^\dagger a_l^\dagger$$

$$[a_j^\dagger a_l^\dagger, a_l^\dagger a_l] = a_j^\dagger a_l^\dagger a_l^\dagger a_l - a_l^\dagger a_l a_j^\dagger a_l^\dagger = -a_j^\dagger a_l^\dagger$$

$$[a_j a_l, a_j^\dagger a_j] = a_j a_l a_j^\dagger a_j - a_j^\dagger a_j a_j a_l = a_j a_l$$

$$[a_j a_l, a_l^\dagger a_l] = a_j a_l a_l^\dagger a_l - a_l^\dagger a_l a_j a_l = a_j a_l$$

and

$$\begin{aligned} [a_j^\dagger a_l, (1 - 2a_j^\dagger a_j)(1 - 2a_l^\dagger a_l)] &= (1 - 2a_j^\dagger a_j)[a_j^\dagger a_l, (1 - 2a_l^\dagger a_l)] + [a_j^\dagger a_l, (1 - 2a_j^\dagger a_j)](1 - 2a_l^\dagger a_l) \\ &= -2(1 - 2a_j^\dagger a_j)a_j^\dagger a_l + 2a_j^\dagger a_l(1 - 2a_l^\dagger a_l) \\ &= -2a_j^\dagger a_l + 4a_j^\dagger a_l + 2a_j^\dagger a_l - 4a_j^\dagger a_l = 0 \end{aligned}$$

$$\begin{aligned} [a_j a_l, (1 - 2a_j^\dagger a_j)(1 - 2a_l^\dagger a_l)] &= (1 - 2a_j^\dagger a_j)[a_j a_l, (1 - 2a_l^\dagger a_l)] + [a_j a_l, (1 - 2a_j^\dagger a_j)](1 - 2a_l^\dagger a_l) \\ &= -2(1 - 2a_j^\dagger a_j)a_j a_l - 2a_j a_l(1 - 2a_l^\dagger a_l) \\ &= -2a_j a_l - 2a_j a_l + 4a_j a_l = 0 \end{aligned}$$

we have

$$[H, N] = 2 \sum_{jl} (\Delta_{jl} a_j a_l - \Delta_{jl}^\dagger a_j^\dagger a_l^\dagger) \quad (\text{A.29})$$

$$[H, P] = 0$$



Since  $[H, P] = 0$ , there are common eigenstates of  $H$  and  $P$ , or that they can be simultaneously diagonalized by some unitary transformation. However, since  $P$  is not a one-body operator, its unitary transformation in general cannot be written as multiplications of  $2N \times 2N$  matrices as the BdG Hamiltonian. We therefore need to understand how the Bogoliubov transformation Eq. A.9 transforms  $P$ . To this end we first write Eq. A.9 into a block form

$$(\tilde{a}^\dagger, \tilde{a}) = (a^\dagger, a)\mathcal{U} \quad (\text{A.30})$$

where  $a \equiv (a_1, a_2, \dots, a_N)$  and so on. On the other hand, Eqs. A.2 and A.1 can be written as

$$(c_o, c_e) = (a^\dagger, a) \begin{pmatrix} 1 & i \\ 1 & -i \end{pmatrix}, \quad (a^\dagger, a) = (c_o, c_e) \begin{pmatrix} \frac{1}{2} & \frac{1}{2} \\ -\frac{i}{2} & \frac{i}{2} \end{pmatrix} \quad (\text{A.31})$$

where  $c_o \equiv (c_1, c_3, \dots, c_{2N-1})$  and  $c_e \equiv (c_2, c_4, \dots, c_{2N})$ . The above equations then lead to

$$\begin{aligned} (\tilde{c}_o, \tilde{c}_e) &= (c_o, c_e) \begin{pmatrix} \frac{1}{2} & \frac{1}{2} \\ -\frac{i}{2} & \frac{i}{2} \end{pmatrix} \mathcal{U} \begin{pmatrix} 1 & i \\ 1 & -i \end{pmatrix} \\ &= (c_o, c_e) \begin{pmatrix} \text{Re}(U_1 + U_2) & -\text{Im}(U_1 - U_2) \\ \text{Im}(U_1 + U_2) & \text{Re}(U_1 - U_2) \end{pmatrix} \\ &= (c_o, c_e)\mathcal{O} \end{aligned} \quad (\text{A.32})$$

or equivalently

$$\tilde{c}_{2j-1} = c_{2k-1}\mathcal{O}_{k,j} + c_{2k}\mathcal{O}_{N+k,j} \quad (\text{A.33})$$

$$\tilde{c}_{2j} = c_{2k-1}\mathcal{O}_{k,N+j} + c_{2k}\mathcal{O}_{N+k,N+j}$$

Since all elements of  $\mathcal{O}$  are real,

$$\mathcal{O}^T \mathcal{O} = \mathcal{O}^\dagger \mathcal{O} = \begin{pmatrix} \frac{1}{2} & \frac{1}{2} \\ -\frac{i}{2} & \frac{i}{2} \end{pmatrix} \mathcal{U}^\dagger \mathcal{U} \begin{pmatrix} 1 & i \\ 1 & -i \end{pmatrix} = \mathbb{I} \quad (\text{A.34})$$

Namely,  $\mathcal{O}$  is a real orthogonal matrix. As a result we have

$$1 = \det(\mathcal{O}^T \mathcal{O}) = (\det\{\mathcal{O}\})^2 \quad (\text{A.35})$$

which necessarily means  $\det\{\mathcal{O}\} = \pm 1$ . From linear algebra we know that an arbitrary special orthogonal matrix, i.e.,  $\det\{\mathcal{O}\} = +1$ , can always be written as

$$\mathcal{O} = e^A \quad (\text{A.36})$$

where  $A = -A^T$  is a real skew-symmetric matrix. But no such general expressions exist for those  $\mathcal{O}$  with  $\det \mathcal{O} = -1$ . For later convenience we reorganize the elements of  $\mathcal{O}$  so that they are labeled in the same way as the Majorana operators. Namely

$$\mathcal{O}_{k,j} \rightarrow \mathcal{O}_{2k-1,2j-1} \quad (\text{A.37})$$

$$\mathcal{O}_{N+k,j} \rightarrow \mathcal{O}_{2k,2j-1}$$

$$\mathcal{O}_{k,N+j} \rightarrow \mathcal{O}_{2k-1,2j}$$

$$\mathcal{O}_{N+k,N+j} \rightarrow \mathcal{O}_{2k,2j}$$

This does not affect the orthogonality of  $\mathcal{O}$ .

To see how  $\mathcal{O}$  transforms  $P$ , we start from Eq. A.26 and note that it can be written as

$$P = (-i)^N \prod_{j=1}^N (c_{2j-1} c_{2j}) = \text{pf}(\mathcal{C}) \quad (\text{A.38})$$

where

$$\mathcal{C} \equiv \begin{pmatrix} C_1 & & \\ & \ddots & \\ & & C_N \end{pmatrix}, C_j \equiv \begin{pmatrix} 0 & -ic_{2j-1}c_{2j} \\ ic_{2j-1}c_{2j} & 0 \end{pmatrix} \quad (\text{A.39})$$

The pfaffian pf for an arbitrary skew-symmetric matrix is defined as

$$\text{pf}(A) = \frac{1}{2^n n!} \sum_{\sigma \in S_{2n}} \text{sgn}(\sigma) \prod_{i=1}^n a_{\sigma(2i-1), \sigma(2i)} \quad (\text{A.40})$$

where  $A$  is a  $2n \times 2n$  skew-symmetric matrix,  $S_{2n}$  is the permutation group of order  $2n$ . For skew-symmetric tridiagonal  $A$  with  $A_{2j-1, 2j} = -A_{2j, 2j-1} = b_j$  and all other elements zero,  $\text{pf}(A) = \prod_{j=1}^n b_j$ . Eq. A.38 is valid since all the  $-ic_{2j-1}c_{2j}$  commute with one another and can be viewed as c-numbers.

Our goal is to convert the complicated transformation rule of  $P$  under  $\mathcal{O}$  to something that is more manageable. To this end we generalize the  $\mathcal{C}$  matrix above to the following:

$$\mathcal{C}_{mn} = \begin{cases} 0 & m = n \\ -ic_m c_n & m \neq n \end{cases} \quad (\text{A.41})$$

Apparently  $\mathcal{C} = -\mathcal{C}^T$  and one can still calculate its pfaffian. To simplify the calculation we use the following equivalent definition of the pfaffian:

$$\text{pf}(A) = \sum_{\alpha \in \Pi} A_\alpha \quad (\text{A.42})$$

where  $A_\alpha$  is

$$A_\alpha = \text{sgn}(\pi_\alpha) a_{i_1, j_1} a_{i_2, j_2} \cdots a_{i_n, j_n} \quad (\text{A.43})$$

and the permutation  $\pi_\alpha$  and its set  $\Pi$  are constructed in the following way: Consider a partition of  $\{1, 2, \dots, 2n\}$  into unordered pairs and define  $\alpha$  as such a partition

$$\alpha = \{(i_1, j_1), (i_2, j_2), \dots, (i_n, j_n)\} \quad (\text{A.44})$$

so that there are  $(2n)!/(2^n n!)$  such partitions. The permutation  $\pi_\alpha$  is defined as

$$\pi_\alpha \equiv \begin{pmatrix} 1 & 2 & 3 & 4 & \dots & 2n-1 & 2n \\ i_1 & j_1 & i_2 & j_2 & \dots & i_n & j_n \end{pmatrix} \quad (\text{A.45})$$

For our  $\mathcal{C}$  this means the counterpart of  $A_\alpha$  is

$$\text{sgn}(\pi_\alpha)(-i)^N c_{m_1} c_{n_1} c_{m_2} c_{n_2} \dots c_{m_N} c_{n_N} = \prod_{j=1}^N (-i c_{2j-1} c_{2j}) \quad (\text{A.46})$$

since  $\text{sgn}(\pi_\alpha)$  is exactly compensated by the anticommutation relation of the Majorana fermions.

We therefore have

$$P = \frac{2^N N!}{(2N)!} \text{pf}(\mathcal{C}) \quad (\text{A.47})$$

We next consider the transformation of  $\mathcal{C}$  by  $\mathcal{O}$ :

$$\tilde{\mathcal{C}}_{mn} = -i \tilde{c}_m \tilde{c}_n = -i \sum_{i \neq j} \mathcal{O}_{mi} \mathcal{O}_{nj} c_i c_j = (\mathcal{O}^T \mathcal{C} \mathcal{O})_{mn} \quad (\text{A.48})$$

which is nothing but the usual similarity transformation of the matrix  $\mathcal{C}$ . We therefore immediately get

$$\begin{aligned} \tilde{P} &= \frac{2^N N!}{(2N)!} \text{pf}(\tilde{\mathcal{C}}) = \frac{2^N N!}{(2N)!} \text{pf}(\mathcal{O}^T \mathcal{C} \mathcal{O}) = \frac{2^N N!}{(2N)!} \text{pf}(\mathcal{C}) \det(\mathcal{O}) \\ &= \det(\mathcal{O}) P \end{aligned} \quad (\text{A.49})$$

Therefore the Bogoliubov transformation  $\mathcal{O}$  preserves the parity if  $\det(\mathcal{O}) = +1$ , and changes the parity if  $\det(\mathcal{O}) = -1$ .

Using the above transformation rule of  $P$  under a general Bogoliubov transformation we can now understand the meaning of ground state parity in [7]. Start from an arbitrary state that is an eigenstate of  $P$  with even parity, we have

$$P|\psi\rangle = |\psi\rangle \quad (\text{A.50})$$

Under a Bogoliubov transformation, the state itself is unchanged, but  $P \rightarrow \tilde{P}$ , since the meaning of particles is different. We then have

$$\tilde{P}|\psi\rangle = \det(\mathcal{O})P|\psi\rangle = \det(\mathcal{O})|\psi\rangle \quad (\text{A.51})$$

Namely, because the Bogoliubov transformation redefines particles and hence the parity operator, an even-parity state can become an odd-parity state in the new definition of the parity operator. Therefore for a given BdG Hamiltonian, the meaning of its ground state parity must be relative, and we need to choose a reference in order to discuss the parity. Such a reference is the ground state of the “canonical form” of the BdG Hamiltonian:

$$\begin{aligned} H_{\text{canonical}} &= \sum_m \epsilon_m (\tilde{a}_m^\dagger \tilde{a}_m - \frac{1}{2}) = \frac{i}{2} \sum_m \tilde{c}_{2m-1} \tilde{c}_{2m} \\ &\equiv \frac{i}{2} \sum_m \epsilon_m b'_m b''_m, \quad \epsilon_m \geq 0 \end{aligned} \quad (\text{A.52})$$

where the crucial requirement is that all the eigenenergies are non-negative. For a given BdG Hamiltonian such a canonical form is uniquely fixed, and we can use its ground state as a reference for the parity and the parity operator. The ground state of  $H_{\text{canonical}}$  is defined by

$$\tilde{a}_m |\Omega_{\text{canonical}}\rangle = 0 \quad \forall m \in [1, N]. \quad (\text{A.53})$$

and the “reference” or canonical parity operator is

$$P_{\text{canonical}} \equiv \prod_{m=1}^N (-i b'_m b''_m). \quad (\text{A.54})$$

Since there are no  $\tilde{a}$  particles in  $|\Omega_{\text{canonical}}\rangle$ , we must have

$$P_{\text{canonical}}|\Omega_{\text{canonical}}\rangle = |\Omega_{\text{canonical}}\rangle \quad (\text{A.55})$$

Namely  $|\Omega_{\text{canonical}}\rangle$  has even parity. We can then ask the following question: What is the parity of  $|\Omega_{\text{canonical}}\rangle$  in the sense of particles in the original BdG Hamiltonian, i.e.,  $a_j$ ? This requires us to evaluate

$$\begin{aligned} P_{\text{BdG}}|\Omega_{\text{canonical}}\rangle &\equiv \prod_j (-i c_{2j-1} c_{2j}) |\Omega_{\text{canonical}}\rangle = \det(\mathcal{O}) P_{\text{canonical}}|\Omega_{\text{canonical}}\rangle \\ &= \det(\mathcal{O}) |\Omega_{\text{canonical}}\rangle \end{aligned} \quad (\text{A.56})$$

Namely, the parity is equal to the determinant of the orthogonal transformation that transforms  $c$  to  $b'$  and  $b''$ . More precisely,

$$\begin{pmatrix} b'_1 \\ b''_1 \\ \vdots \\ b'_N \\ b''_N \end{pmatrix} = \mathcal{O} \begin{pmatrix} c_1 \\ c_2 \\ \vdots \\ c_{2N-1} \\ c_{2N} \end{pmatrix} \quad (\text{A.57})$$

and

$$\mathcal{O} A \mathcal{O}^T = \begin{pmatrix} 0 & \epsilon_1 & & \\ -\epsilon_1 & 0 & & \\ & & \ddots & \\ & & & 0 & \epsilon_N \\ & & & -\epsilon_N & 0 \end{pmatrix} \quad (\text{A.58})$$

where  $A$  is introduced in Eq. A.4, and our  $\mathcal{O}$  is the matrix  $W$  in [7]. Eq. A.58 therefore leads to a convenient formula for calculating  $\det(\mathcal{O})$ :

$$\text{pf}(\mathcal{O} A \mathcal{O}^T) = \det(\mathcal{O}) \text{pf}(A) = \text{pf} \begin{pmatrix} 0 & \epsilon_1 & & \\ -\epsilon_1 & 0 & & \\ & & \ddots & \\ & & & 0 & \epsilon_N \\ & & & -\epsilon_N & 0 \end{pmatrix} = \prod_m \epsilon_m \geq 0 \quad (\text{A.59})$$

Therefore

$$\det(\mathcal{O}) = \left( \prod_m \epsilon_m \right) [\text{pf}(A)]^{-1} \quad (\text{A.60})$$

Since  $\det(\mathcal{O}) = \pm 1$  we only need the signs of the two quantities on the right hand side of the above equation. If none of the  $\epsilon_m$  vanishes,  $(\prod_m \epsilon_m) > 0$ , we finally arrive at

$$\det(\mathcal{O}) = \text{sgn}[\text{pf}(A)] \quad (\text{A.61})$$

Namely,

$$\begin{aligned} P_{\text{BdG}}|\Omega_{\text{canonical}}\rangle &= \det(\mathcal{O})|\Omega_{\text{canonical}}\rangle \\ &= \text{sgn}[\text{pf}(A)]|\Omega_{\text{canonical}}\rangle \end{aligned} \quad (\text{A.62})$$

## A.2 Gauge potential and gauge invariance

In this section we address the question of how to understand the Peierls substitution in BdG Hamiltonian.

Although the superconductivity order parameter appears to break the U(1) gauge symmetry, all physical observables are still gauge invariant. More explicitly, consider a general tight-binding BdG Hamiltonian

$$H = \sum_{ij,\alpha\beta} \left( t_{ij}^{\alpha\beta} c_{i\alpha}^\dagger c_{j\beta} + \Delta_{ij,\alpha\beta} c_{i\alpha} c_{j\beta} - \frac{\mu}{2} c_{i\alpha}^\dagger c_{i\alpha} + \text{h.c.} \right) \equiv \frac{1}{2} C^\dagger h C \quad (\text{A.63})$$

where  $i, j$  label position,  $\alpha, \beta$  label any internal degrees of freedom, and  $C = (\{c_{i\alpha}\}, \{c_{i\alpha}^\dagger\})^T$ .  $H$  has the eigensolutions

$$H|\psi_n\rangle = \epsilon_n|\psi_n\rangle \quad (\text{A.64})$$

$$|\psi_n\rangle = d_{\psi_n}^\dagger |\Omega\rangle = \sum_{i\alpha\sigma} c_{i\alpha}^\sigma |\Omega\rangle U_{i\alpha\sigma,n}$$

where  $|\Omega\rangle$  is the BCS ground state,  $\sigma = \pm$  distinguishes the creation (particle) and annihilation (creation for hole) operators, and  $U$  is a Bogoliubov transformation matrix which is unitary for fermions. Substituting  $|\psi\rangle$  into the eigenequation leads to

$$U^\dagger h U = \text{Diag}[\{\epsilon_n\}] \quad (\text{A.65})$$



where the pairing potential satisfies the gap equation

$$\begin{aligned}\Delta_{ij,\alpha\beta} &= Z^{-1} \text{Tr}[V_{j\beta,i\alpha} c_{j\beta}^\dagger c_{i\alpha}^\dagger e^{-\frac{1}{k_B T} H}] \\ &= \sum_n f(\epsilon_n) (U^\dagger \mathbb{V} U)_{nn}\end{aligned}\tag{A.66}$$

where  $\mathbb{V}$  is a matrix with the only nonzero element being  $\mathbb{V}_{j\beta+,i\alpha-} = V_{j\beta,i\alpha}$ ,  $f$  is the Fermi-Dirac distribution function.

We now show that physical observables are gauge invariant. A gauge transformation corresponds to

$$\mathbf{A} \rightarrow \mathbf{A}' = \mathbf{A} + \nabla \chi\tag{A.67}$$

where  $\mathbf{A}$  is the gauge potential.  $\mathbf{A}$  enters the tight-binding Hamiltonian implicitly through the Peierls substitution:

$$c_{i\alpha}^\dagger \rightarrow \tilde{c}_{i\alpha}^\dagger = e^{-\frac{ie}{\hbar} \int_0^{\mathbf{r}_i} \mathbf{A} \cdot d\mathbf{l}} c_{i\alpha}^\dagger\tag{A.68}$$

and we can understand Eq. (A.63) as that written for certain  $\mathbf{A}$  already absorbed into the definitions of  $t$  and  $\Delta$ . The gauge transformation leads to

$$c_{i\alpha}^\dagger \rightarrow c_{i\alpha}^\dagger e^{-\frac{ie}{\hbar} \chi_i}\tag{A.69}$$

The Hamiltonian therefore becomes

$$\begin{aligned}H \rightarrow H' &= \sum_{ij,\alpha\beta} \left[ t_{ij}^{\alpha\beta} e^{-\frac{ie}{\hbar}(\chi_i - \chi_j)} c_{i\alpha}^\dagger c_{j\beta} + \Delta_{ij,\alpha\beta} e^{\frac{ie}{\hbar}(\chi_i + \chi_j)} c_{i\alpha} c_{j\beta} - \frac{\mu}{2} c_{i\alpha}^\dagger c_{i\alpha} + \text{h.c.} \right] \\ &= \frac{1}{2} C^\dagger U_\chi h U_\chi^\dagger C\end{aligned}\tag{A.70}$$

where

$$U_\chi = \text{Diag}[\{e^{-\frac{ie}{\hbar}\chi_i}\}, \{e^{\frac{ie}{\hbar}\chi_i}\}] \quad (\text{A.71})$$

As a result, the BdG eigenvalues as well as all other physical observables represented in terms of Bogoliubov quasiparticles are invariant under the gauge transformation.

The above derivation includes, however, an assumption. Namely the pairing potential  $\Delta_{ij,\alpha\beta}$  stays unchanged. This is indeed the case, since

$$\begin{aligned} \Delta'_{ij,\alpha\beta} &= Z'^{-1} \text{Tr}[V_{j\beta,i\alpha} c_{j\beta}^\dagger c_{i\alpha}^\dagger e^{-\frac{ie}{\hbar}(\chi_i + \chi_j)} e^{-\frac{1}{k_B T} H'}] \\ &= \sum_n f(\epsilon_n) (U^\dagger U_\chi^\dagger U_\chi U^\dagger U_\chi U) \\ &= \Delta_{ij,\alpha\beta} \end{aligned} \quad (\text{A.72})$$

### A.3 Kitaev Triangle and Peierls substitution

We start with a spinless or spin-polarized  $p$ -wave superconductor

$$\mathcal{H} = \sum_{\langle j,l \rangle} (-t c_j^\dagger c_l + \Delta e^{i\theta_{jl}} c_j c_l + h.c.) - \sum_j \mu c_j^\dagger c_j, \quad (\text{A.73})$$

where  $t$  is the hopping amplitude,  $\Delta$  is the amplitude of (2D)  $p$ -wave pairing,  $\mu$  is the chemical potential,  $\theta_{jl}$  is the polar angle of  $\mathbf{r}_{jl} = \mathbf{r}_l - \mathbf{r}_j$ , consistent with  $\{c_l^\dagger, c_j^\dagger\} = 0$ .

We will now include a gauge potential via a Peierls substitution as

$$\begin{aligned}
c_j^\dagger &\rightarrow c_j^\dagger \exp\left(-\frac{ie}{\hbar} \int_0^{\mathbf{r}_j} \mathbf{A} \cdot d\mathbf{l}\right), \\
c_j^\dagger c_l &\rightarrow c_j^\dagger c_l \exp\left(\frac{ie}{\hbar} \int_{\mathbf{r}_j}^{\mathbf{r}_l} \mathbf{A} \cdot d\mathbf{l}\right) \\
&\rightarrow c_l^\dagger c_j e^{i\phi_{j,l}}. \\
\phi_{jl} &= \frac{e}{\hbar} \int_{\mathbf{r}_j}^{\mathbf{r}_l} \mathbf{A} \cdot d\mathbf{l} = -\phi_{lj}
\end{aligned} \tag{A.74}$$

The modified Hamiltonian is then

$$\mathcal{H} = \sum_{\langle j,l \rangle} (-te^{i\phi_{jl}} c_j^\dagger c_l + \Delta e^{i\theta_{jl}} c_j c_l + h.c.) - \sum_j \mu c_j^\dagger c_j, \tag{A.75}$$

The complex fermion operator can be written in the Majorana Fermion basis, a superposition of two Majorana fermions  $c_j = \frac{1}{2}(a_j + ib_j)$ . Due to the nature of Majorana fermions,  $a_j^\dagger = a_j$ , the creation operator is  $c_j^\dagger = \frac{1}{2}(a_j - ib_j)$ . It is quickly seen after substitution we arrive at

$$c_j^\dagger c_j = \frac{1}{2}(1 + ia_j b_j), \tag{A.76}$$

$$c_j^\dagger c_l = \frac{1}{4}(a_j a_l + b_j b_l + ia_j b_l - ib_j a_l), \tag{A.77}$$

$$c_j c_l = \frac{1}{4}(a_j a_l - b_j b_l + ia_j b_l + ib_j a_l). \tag{A.78}$$

The hopping term in MF basis are

$$-t(e^{i\phi_{jl}} c_j^\dagger c_l + e^{-i\phi_{jl}} c_l^\dagger c_j) = -\frac{it}{2}(\sin \phi_{jl}(a_j a_l + b_j b_l) + \cos \phi_{jl}(a_j b_l - b_j a_l)), \tag{A.79}$$

the order parameter terms are

$$\Delta(e^{i\theta_{jl}}c_j^\dagger c_l^\dagger + e^{-i\theta_{jl}}c_j c_l) = \frac{i\Delta}{2}(\sin\theta_{jl}(a_l a_j - b_l b_j) + \cos\theta_{jl}(a_l b_j + b_l a_j)). \quad (\text{A.80})$$

Our Hamiltonian in MF basis is then

$$\begin{aligned} \mathcal{H} = & -\frac{i}{2} \sum_{\langle j,l \rangle} [(t \sin\phi_{jl} - \Delta \sin\theta_{jl})a_j a_l + (t \sin\phi_{jl} + \Delta \sin\theta_{jl})b_j b_l \\ & + (t \cos\phi_{jl} - \Delta \cos\theta_{jl})a_j b_l - (t \cos\phi_{jl} + \Delta \cos\theta_{jl})b_j a_l] \\ & - \frac{i\mu}{2} \sum_j a_j b_j \end{aligned} \quad (\text{A.81})$$

For concreteness we consider a 1-D chain in the Kitaev limit  $t = \Delta$ ,  $\mu = 0$ , and choose  $\phi_{jl} = 0$  (either zero or a perpendicular gauge potential). The Kitaev chain is resultant with  $\mathcal{H} = -\sum_{j,j+1} i t b_j a_{j+1}$  and hosting MZM  $a_1$  and  $b_N$ .

## A.4 Effective $p$ -wave superconductors

We start with the relevant non-interacting Hamiltonian

$$\mathcal{H}_0 = \sum_{\mathbf{k}} c_{\mathbf{k}}^\dagger \left[ \frac{\hbar^2 k^2}{2m} - \mu + \alpha(\sigma^x k_y - \sigma^y k_x) \right] c_{\mathbf{k}} \quad (\text{A.82})$$

where  $m$  is the effective mass,  $\mu$  is the chemical potential,  $\alpha$  is the Rashba spin-orbit coupling strength, and  $\sigma^i$  are the Pauli matrices that act on the spin degrees of freedom in  $c_{\mathbf{k}}$ , and  $\hbar = 1$  throughout.

Next, introduce a ferromagnetic insulator to induce a Zeeman effect. The ferromagnetic insulator has magnetization pointing perpendicular to the 2D semiconductor with energy

$$\mathcal{H}_Z = V_z \sum_{\mathbf{k}} c_{\mathbf{k}}^\dagger \sigma^z c_{\mathbf{k}} \quad (\text{A.83})$$

but negligible orbital coupling. One can build an eigenbasis from the combined Hamiltonian with the following eigenenergies  $\epsilon'_{\pm}(\mathbf{k}) = \pm \sqrt{V_z^2 + \alpha^2 k^2}$  with eigenvectors

$$u_+(\mathbf{k}) = \begin{pmatrix} A_{\uparrow}(\mathbf{k}) \\ -A_{\downarrow}(\mathbf{k}) \frac{k_y - i k_x}{k} \end{pmatrix}, \quad (\text{A.84})$$

$$(\text{A.85})$$

$$u_-(\mathbf{k}) = \begin{pmatrix} B_{\uparrow}(\mathbf{k}) \frac{k_y + i k_x}{k} \\ B_{\downarrow}(\mathbf{k}) \end{pmatrix}. \quad (\text{A.86})$$

Where  $A_{\sigma} = A_{\sigma}^*$  and  $B_{\sigma} = B_{\sigma}^*$  and the coefficients are

$$A_{\uparrow}(\mathbf{k}) = \frac{-\alpha k}{\sqrt{2\epsilon'_+(\mathbf{k})}} \sqrt{\frac{1}{\epsilon'_+(\mathbf{k}) - V_z}} \quad (\text{A.87})$$

$$A_{\downarrow}(\mathbf{k}) = \sqrt{\frac{\epsilon'_+(\mathbf{k}) - V_z}{2\epsilon'_+(\mathbf{k})}} \quad (\text{A.88})$$

$$B_{\uparrow}(\mathbf{k}) = \sqrt{\frac{\epsilon'_-(\mathbf{k}) + V_z}{2\epsilon'_-(\mathbf{k})}} \quad (\text{A.89})$$

$$B_{\downarrow}(\mathbf{k}) = \frac{\alpha k}{\sqrt{2\epsilon'_-(\mathbf{k})}} \sqrt{\frac{1}{\epsilon'_-(\mathbf{k}) + V_z}}. \quad (\text{A.90})$$

The expressions for  $A_{\uparrow,\downarrow}$  and  $B_{\uparrow,\downarrow}$  can be written as

$$f_p(\mathbf{k}) = A_{\uparrow}(\mathbf{k}) A_{\downarrow}(-\mathbf{k}) = B_{\uparrow}(-\mathbf{k}) B_{\downarrow}(\mathbf{k}) \quad (\text{A.91})$$

$$= \frac{-\alpha k}{2\epsilon'_+(\mathbf{k})}. \quad (\text{A.92})$$

With the semiconductor in contact with an  $s$ -wave superconductor, a pairing term is generated by the proximity effect. The full Hamiltonian becomes  $\mathcal{H} = \mathcal{H}_0 + \mathcal{H}_Z + \mathcal{H}_{SC}$  with

$$\mathcal{H}_{SC} = \sum_{\mathbf{k}} \Delta c_{\uparrow, \mathbf{k}}^\dagger c_{\downarrow, -\mathbf{k}}^\dagger + H.c. \quad (\text{A.93})$$

Write the pairing potential in terms of  $c_\pm$  using a basis transformation,

$$c_{\uparrow, \mathbf{k}} = \langle \uparrow | u_+(\mathbf{k}) \rangle c_{\mathbf{k}, +} + \langle \uparrow | u_-(\mathbf{k}) \rangle c_{\mathbf{k}, -} \quad (\text{A.94})$$

$$= A_\uparrow(\mathbf{k}) c_{\mathbf{k}, +} + B_\uparrow(\mathbf{k}) \frac{k_y + i k_x}{k} c_{\mathbf{k}, -}, \quad (\text{A.95})$$

$$c_{\downarrow, -\mathbf{k}} = \langle \downarrow | u_+(-\mathbf{k}) \rangle c_{-\mathbf{k}, +} + \langle \downarrow | u_-(-\mathbf{k}) \rangle c_{-\mathbf{k}, -} \quad (\text{A.96})$$

$$= A_\downarrow(-\mathbf{k}) \frac{k_y - i k_x}{k} c_{-\mathbf{k}, +} + B_\downarrow(-\mathbf{k}) c_{-\mathbf{k}, -} \quad (\text{A.97})$$

with the adjoints being

$$c_{\uparrow, \mathbf{k}}^\dagger = A_\uparrow(\mathbf{k}) c_{\mathbf{k}, +}^\dagger + B_\uparrow(\mathbf{k}) \frac{k_y - i k_x}{k} c_{\mathbf{k}, -}^\dagger \quad (\text{A.98})$$

$$c_{\downarrow, -\mathbf{k}}^\dagger = A_\downarrow(-\mathbf{k}) \frac{k_y + i k_x}{k} c_{-\mathbf{k}, +}^\dagger + B_\downarrow(-\mathbf{k}) c_{-\mathbf{k}, -}^\dagger. \quad (\text{A.99})$$

Reducing the pairing potential further becomes

$$\begin{aligned} \Delta c_{\uparrow, \mathbf{k}}^\dagger c_{\downarrow, -\mathbf{k}}^\dagger &= \Delta [A_\uparrow(\mathbf{k}) A_\downarrow(-\mathbf{k}) \frac{k_y + i k_x}{k} c_{\mathbf{k}, +}^\dagger c_{-\mathbf{k}, +}^\dagger + B_\uparrow(\mathbf{k}) B_\downarrow(-\mathbf{k}) \frac{k_y - i k_x}{k} c_{\mathbf{k}, -}^\dagger c_{-\mathbf{k}, -}^\dagger \\ &\quad + (A_\uparrow(\mathbf{k}) B_\downarrow(-\mathbf{k}) + B_\uparrow(\mathbf{k}) A_\downarrow(-\mathbf{k})) c_{\mathbf{k}, +}^\dagger c_{-\mathbf{k}, -}^\dagger]. \end{aligned} \quad (\text{A.100})$$

We make the following substitutions

$$\Delta_{++}(\mathbf{k}) = \Delta f_p(\mathbf{k}) \frac{k_y + i k_x}{k} \quad (\text{A.101})$$

$$\Delta_{--}(\mathbf{k}) = \Delta f_p(-\mathbf{k}) \frac{k_y - i k_x}{k} \quad (\text{A.102})$$

$$\Delta_{+-}(\mathbf{k}) = \Delta f_s(\mathbf{k}), \quad (\text{A.103})$$

where

$$f_s(\mathbf{k}) = (A_\uparrow(\mathbf{k})B_\downarrow(-\mathbf{k}) + B_\uparrow(\mathbf{k})A_\downarrow(-\mathbf{k})). \quad (\text{A.104})$$

The pairing potential Hamiltonian then becomes

$$\mathcal{H}_{SC} = \sum_{\mathbf{k}} \Delta_{++} c_{\mathbf{k},+}^\dagger c_{-\mathbf{k},+}^\dagger + \Delta_{--} c_{\mathbf{k},-}^\dagger c_{-\mathbf{k},-}^\dagger + \Delta_{+-} c_{\mathbf{k},+}^\dagger c_{-\mathbf{k},-}^\dagger + h.c. \quad (\text{A.105})$$

Writing the full Hamiltonian in matrix form we will use the following Nambu spinor

$$\Psi = (c_{\mathbf{k},+}, c_{\mathbf{k},-}, c_{-\mathbf{k},+}^\dagger, c_{-\mathbf{k},-}^\dagger)^T. \quad (\text{A.106})$$

Then, write the Hamiltonian using the conventional BdG approach of applying the anti-commutation relation and reindexing the momentum vector of the second term to give

$$\mathcal{H} = \frac{1}{2} \sum_{\mathbf{k}} \Psi^\dagger H_{BdG} \Psi \quad (\text{A.107})$$

with

$$H_{BdG} = \begin{bmatrix} \epsilon_+(\mathbf{k}) & 0 & 2\Delta_{++}(\mathbf{k}) & \Delta_{+-}(\mathbf{k}) \\ 0 & \epsilon_-(\mathbf{k}) & -\Delta_{+-}(-\mathbf{k}) & 2\Delta_{--}(\mathbf{k}) \\ 2\Delta_{++}^*(\mathbf{k}) & -\Delta_{+-}^*(-\mathbf{k}) & -\epsilon_+(-\mathbf{k}) & 0 \\ \Delta_{+-}^*(\mathbf{k}) & 2\Delta_{--}^*(\mathbf{k}) & 0 & -\epsilon_-(-\mathbf{k}) \end{bmatrix}, \quad (\text{A.108})$$

where

$$\epsilon_{\pm}(\mathbf{k}) = \frac{k^2}{2m} - \mu + \epsilon'_{\pm}(\mathbf{k}). \quad (\text{A.109})$$

Rearranging the matrix into a more block diagonal form of (++) and (--) gives

$$H_{BdG} = \begin{bmatrix} \epsilon_+(\mathbf{k}) & 2\Delta_{++} & 0 & \Delta_{+-}(\mathbf{k}) \\ 2\Delta_{++}^* & -\epsilon_+(-\mathbf{k}) & -\Delta_{+-}^*(-\mathbf{k}) & 0 \\ 0 & -\Delta_{+-}(-\mathbf{k}) & \epsilon_-(\mathbf{k}) & 2\Delta_{--} \\ \Delta_{+-}^*(\mathbf{k}) & 0 & 2\Delta_{--}^* & -\epsilon_-(-\mathbf{k}) \end{bmatrix}. \quad (\text{A.110})$$



## Appendix B

# Landau Level-Like Topological Floquet Hamiltonians

### B.1 Quantum harmonic oscillator

We will quickly derive this energy solution and derive ladder operators. Rewrite the quantum harmonic oscillator as (and dropping the operator hat)

$$H = \frac{1}{2m} (p_x^2 + m^2 \omega^2 x^2),$$

then complete the square by adding "zero"

$$\begin{aligned} H &= \frac{1}{2m} ([m\omega x - i p_x][m\omega x + i p_x] - i m\omega [x p_x - p_x x]) \\ &= \frac{1}{2m} ([m\omega x - i p_x][m\omega + i p_x] + m\hbar\omega) \\ &= \frac{1}{2m} (\tilde{a}^\dagger \tilde{a} + m\hbar\omega) \\ &= \hbar\omega \left( \frac{\tilde{a}^\dagger \tilde{a}}{2m\hbar\omega} + \frac{1}{2} \right) \\ &= \hbar\omega \left( a^\dagger a + \frac{1}{2} \right), \end{aligned} \tag{B.1}$$

where  $a = \frac{1}{\sqrt{2}} \left( \sqrt{\frac{m\omega}{\hbar}} x + i \frac{p_x}{\sqrt{m\hbar\omega}} \right)$ . We have simplified the Hamiltonian into new creation and annihilation operators, called ladder operators, which we will now show how they work. Also note  $[a, a^\dagger] = 1$ . Let looks at how the operator commutes with the Hamiltonian

$$\begin{aligned}
[H, a] &= Ha - aH = \hbar\omega \left( a^\dagger aa + \frac{a}{2} - aa^\dagger a - \frac{a}{2} \right) \\
&= \hbar\omega(a^\dagger a - (1 + a^\dagger a))a \\
&= -\hbar\omega a, \quad \text{and}
\end{aligned} \tag{B.2}$$

$$\begin{aligned}
[H, a^\dagger] &= Ha^\dagger - a^\dagger H = \hbar\omega \left( a^\dagger aa^\dagger + \frac{a^\dagger}{2} - a^\dagger a^\dagger a - \frac{a^\dagger}{2} \right) \\
&= \hbar\omega a^\dagger (aa^\dagger - a^\dagger a) \\
&= \hbar\omega a^\dagger.
\end{aligned} \tag{B.3}$$

Let  $H$  act on the wavefunction as

$$H|\psi_n\rangle = E_n|\psi_n\rangle.$$

$$Ha^\dagger|\psi_n\rangle = (a^\dagger H + \hbar\omega a^\dagger)|\psi_n\rangle$$

$$Ha^\dagger|\psi_n\rangle = (E_n + \hbar\omega)a^\dagger|\psi_n\rangle.$$

$$Ha|\psi_n\rangle = (E_n - \hbar\omega)a|\psi_n\rangle.$$

(B.4)

We notice

$$H|\psi_0\rangle = E_0|\psi_0\rangle$$

$$Ha|\psi_0\rangle = (E_0 - \hbar\omega)a|\psi_0\rangle, \tag{B.5}$$

however,  $E_0$  is the minimum so  $E_0 - \hbar\omega$  cannot exist and thus

$$a|\psi_0\rangle = 0 \quad (\text{B.6})$$

Again, we look at the ground state energy

$$\begin{aligned} \langle\psi_0|H|\psi_0\rangle &= \langle\psi_0|\hbar\omega(a^\dagger a + 1/2)|\psi_0\rangle \\ E_0 &= \hbar\omega\langle\psi_0|a^\dagger a|\psi_0\rangle + \frac{\hbar\omega}{2}\langle\psi_0|\psi_0\rangle \\ E_0 &= \frac{\hbar\omega}{2}. \end{aligned} \quad (\text{B.7})$$

Then for the given eigenstates

$$a^\dagger|\psi_0\rangle, \quad a^\dagger a^\dagger|\psi_0\rangle, \quad a^\dagger a^\dagger a^\dagger|\psi_0\rangle, \quad \dots$$

with eigenvalues

$$\frac{3}{2}\hbar\omega, \quad \frac{5}{2}\hbar\omega, \quad \frac{7}{2}\hbar\omega, \quad \dots$$

Can be generalized to

$$|\psi_n\rangle \propto (a^\dagger)^n|\psi_0\rangle,$$

with the eigenenergy

$$E_n = \hbar\omega\left(n + \frac{1}{2}\right).$$

With our goal complete we continue on to determine how the ladder operators evolve the state.

We can now renormalize our proportional expression

$$|\psi_{n+1}\rangle = c a^\dagger |\psi_n\rangle$$

$$1 = \langle \psi_{n+1} | \psi_{n+1} \rangle = |c|^2 (\langle \psi_n | a^\dagger) (a^\dagger |\psi_n\rangle)$$

$$= |c|^2 \langle \psi_n | a a^\dagger | \psi_n \rangle$$

$$= |c|^2 \langle \psi_n | \frac{H}{\hbar\omega} + \frac{1}{2} | \psi_n \rangle$$

$$= |c|^2 \left( \frac{E_n}{\hbar\omega} + \frac{1}{2} \right)$$

$$= |c|^2 (n+1)$$

$$|c| = \frac{1}{\sqrt{n+1}}$$

which give the following relation

$$|\psi_{n+1}\rangle = \frac{a^\dagger}{\sqrt{n+1}} |\psi_n\rangle. \quad (\text{B.8})$$

Similarly we find

$$|\psi_{n-1}\rangle = \frac{a}{\sqrt{n}} |\psi_n\rangle. \quad (\text{B.9})$$

Thus  $a^\dagger a |\psi_n\rangle = n |\psi_n\rangle$ . The energy of the system is definitively

$$E_n = \hbar\omega \left( n + \frac{1}{2} \right) \quad (\text{B.10})$$

## B.2 Dirac equation in the presence of a magnetic field

We now focus on how the presence of a magnetic field affects the Dirac equation. The Dirac Hamiltonian with vector potential

$$\mathcal{H} = v_f \boldsymbol{\sigma} \cdot (\hat{\mathbf{p}} - q\hat{\mathbf{A}}) \quad (\text{B.11})$$

Using the previous definition,  $\mathbf{A} = Bx\hat{\mathbf{y}}$ , the Hamiltonian becomes

$$\mathcal{H} = v_f \sigma_x \hat{p}_x + v_f \sigma_y (\hat{p}_y - qB\hat{x}) \quad (\text{B.12})$$

Like Schrodinger's equation we use the same ansatz wavefunction and arrive at

$$\begin{aligned} \mathcal{H} &= v_f \sigma_x \hat{p}_x - v_f \sigma_y (qB\hat{x} - \hbar k_y) \\ \mathcal{H} &= v_f \sigma_x \hat{p}_x - v_f \sigma_y qB\hat{x}, \end{aligned} \quad (\text{B.13})$$

where we recognize the x term is just shifted by a constant. In matrix form the Hamiltonian looks like

$$\begin{aligned} \mathcal{H} &= i v_f q B \begin{bmatrix} 0 & \hat{p}_x + i q B \hat{x} \\ \hat{p}_x - i q B \hat{x} & 0 \end{bmatrix} \\ \mathcal{H} &= i v_f \sqrt{2\hbar q B} \begin{bmatrix} 0 & a^\dagger \\ -a & 0 \end{bmatrix} \end{aligned}$$

The form of the Hamiltonian can be quickly solved by squaring then acting on a wavefunction

$$\mathcal{H}^2 = 2\hbar q B v_f^2 \begin{bmatrix} a^\dagger a & 0 \\ 0 & a a^\dagger \end{bmatrix}$$

We focus on the first element of the matrix

$$\begin{aligned}
\langle \psi_n | \mathcal{H}_{11}^2 | \psi_n \rangle &= \langle \psi_n | E_n^2 | \psi_n \rangle \\
&= 2\hbar q B v_f^2 \langle \psi_n | a^\dagger a | \psi_n \rangle \\
&= 2\hbar q B v_f^2 \langle \psi_n | n | \psi_n \rangle \\
E_n^2 &= 2\hbar q B n v_f^2 \\
E_n &= \pm v_f \sqrt{2\hbar q B n}
\end{aligned} \tag{B.14}$$

### B.3 General framework of Floquet theory

In this section we review the basic results of the Floquet theory and how to recast it into a matrix diagonalization problem. The discussion in this section is mostly following [77].

For a time-periodic Hamiltonian  $H(t) = H(t + T)$  with period  $T$ , the time evolution of a wavefunction governed by it is described by the Schrödinger equation

$$i\hbar \partial_t \psi(t) = H(t) \psi(t). \tag{B.15}$$

Floquet theorem states that  $\psi(t)$  must satisfy

$$\psi(t + T) = \psi(t) e^{-i \frac{\epsilon T}{\hbar}}, \tag{B.16}$$

where  $\epsilon$  is a real number of energy units, or equivalently

$$\psi(t) = e^{-i \frac{\epsilon t}{\hbar}} u_\epsilon(t), \tag{B.17}$$

where  $u_\epsilon(t) = u_\epsilon(t + T)$ .

Here we give a proof that is closely analogous to that of the Bloch theorem, based on plane wave expansion. An arbitrary wavefunction can be expanded into plane waves

$$\psi(t) = \sum_{\epsilon} c_{\epsilon} e^{-i\frac{\epsilon t}{\hbar}}, \quad (\text{B.18})$$

where  $\epsilon \in \mathbb{R}$ , while a time-periodic function  $H(t)$  can only be written as a discrete Fourier series

$$H(t) = \sum_n H_n e^{in\omega t}, \quad (\text{B.19})$$

where  $\omega = 2\pi/T$ , and  $H_n = \frac{1}{T} \int_0^T H(t) e^{-in\omega t} dt$ . Substituting the two expansions above into Eq. B.15 gives

$$\begin{aligned} 0 &= \sum_{\epsilon} \left[ \sum_n H_n e^{-i\frac{(\epsilon - n\hbar\omega)t}{\hbar}} c_{\epsilon} - \epsilon c_{\epsilon} e^{-i\frac{\epsilon t}{\hbar}} \right] \\ &= \sum_{\epsilon} \left[ \sum_n H_n c_{\epsilon + n\hbar\omega} - \epsilon c_{\epsilon} \right] e^{-i\frac{\epsilon t}{\hbar}}, \end{aligned} \quad (\text{B.20})$$

which leads to

$$\sum_n H_n c_{\epsilon + n\hbar\omega} - \epsilon c_{\epsilon} = 0. \quad (\text{B.21})$$

For an arbitrary  $\epsilon \in \mathbb{R}$  we can define  $\tilde{\epsilon} \in [-\hbar\omega/2, \hbar\omega/2)$  so that  $\epsilon = \tilde{\epsilon} + m\hbar\omega$ . It is apparent that Eq. B.21 only couples  $c_{\tilde{\epsilon} + m\hbar\omega}$  belonging to the same  $\tilde{\epsilon}$ . We thus define

$$c_{\tilde{\epsilon} + m\hbar\omega} \equiv c_{m\tilde{\epsilon}}, \quad (\text{B.22})$$

so that Eq. B.21 becomes a set of coupled equations for  $c_{m\tilde{\epsilon}}$ ,  $m \in \mathbb{Z}$ :

$$\sum_n (H_n - m\hbar\omega \delta_{n0}) c_{m+n, \tilde{\epsilon}} = \tilde{\epsilon} c_{m\tilde{\epsilon}}. \quad (\text{B.23})$$

Eq. B.21 is the eigenvalue problem of the infinite-dimensional matrix  $\bar{Q}$  with the matrix elements

$$\bar{Q}_{m,m+n} = H_n - m\hbar\omega\delta_{n0}, \quad (\text{B.24})$$

which is also the quasienergy operator in [77]. In practice the number of eigenvalues  $\tilde{\epsilon}$  is determined by the dimension of  $H(t)$ . The solutions of Eq. B.15 are therefore

$$\psi_{\tilde{\epsilon}}(t) = \sum_m c_{m\tilde{\epsilon}} e^{-i\frac{(\tilde{\epsilon}+m\hbar\omega)t}{\hbar}} = e^{-i\frac{\tilde{\epsilon}t}{\hbar}} \sum_m c_{m\tilde{\epsilon}} e^{-im\omega t} \equiv e^{-i\frac{\tilde{\epsilon}t}{\hbar}} u_{\tilde{\epsilon}}(t). \quad (\text{B.25})$$

The proof above also gives a useful device for calculating the Floquet states  $\psi_{\tilde{\epsilon}}(t)$  based on plane wave expansion. In general  $H_n$  can be a complicated operator depending on, e.g. position, spin, etc., and  $c_{m\tilde{\epsilon}}$  is a function depending on these quantum numbers. One can choose a representation that makes  $H_0$  diagonal, such as the Bloch representation, leading to the eigenvalues  $\epsilon_{n\mathbf{k}}$  of the time-averaged Hamiltonian ( $H_0$ ). When  $H_n$  is 0 for all  $n \neq 0$ , we have  $\tilde{\epsilon} = \epsilon_{n\mathbf{k}} - m\hbar\omega$ ,  $m \in \mathbb{Z}$ . When  $H_n$  is nonzero for any  $n \neq 0$  there is in general no simple relationship between  $\tilde{\epsilon}$  and  $\epsilon_{n\mathbf{k}}$ . Nonetheless, when  $H_n$ ,  $n \neq 0$  can be viewed as perturbation the spectrum of  $\tilde{\epsilon}$  is similar to that of  $\epsilon_{n\mathbf{k}} - m\hbar\omega$ , i.e., the eigenenergies  $\epsilon_{n\mathbf{k}}$  together with infinite number of its copies shifted vertically by  $m\hbar\omega$ .

The importance of  $\tilde{\epsilon}$  is that it completely determines the stroboscopic motion of an arbitrary Floquet wavefunction, i.e.,

$$\psi_{\tilde{\epsilon}}(t + mT) = e^{-i\frac{\tilde{\epsilon}mT}{\hbar}} \psi_{\tilde{\epsilon}}(t), \quad \forall m \in \mathbb{Z}. \quad (\text{B.26})$$

Since  $\{\psi_{\tilde{\epsilon}}(t)\}$  is a complete set at time  $t$ , the stroboscopic evolution of an arbitrary wavefunction governed by  $H(t)$  is

$$\Psi(t + mT) = \sum_{\tilde{\epsilon}} C_{\tilde{\epsilon}} e^{-i\frac{\tilde{\epsilon}mT}{\hbar}} \psi_{\tilde{\epsilon}}(t), \quad (\text{B.27})$$



where  $\Psi(t) = \sum_{\tilde{\epsilon}} C_{\tilde{\epsilon}} \psi_{\tilde{\epsilon}}(t)$ . The full time-evolution operator  $\hat{\mathbf{U}}(t_1, t_0)$  is therefore

$$\hat{\mathbf{U}}(t_1, t_0) = \sum_{\tilde{\epsilon}} |\psi_{\tilde{\epsilon}}(t_1)\rangle \langle \psi_{\tilde{\epsilon}}(t_0)| = \sum_{\tilde{\epsilon}} |u_{\tilde{\epsilon}}(t_1)\rangle \langle u_{\tilde{\epsilon}}(t_0)| e^{-i \frac{\tilde{\epsilon}(t_1 - t_0)}{\hbar}}. \quad (\text{B.28})$$

Now we introduce two operators

$$\hat{\mathbf{U}}^F(t_1, t_0) \equiv \sum_{\tilde{\epsilon}} |u_{\tilde{\epsilon}}(t_1)\rangle \langle u_{\tilde{\epsilon}}(t_0)|, \quad (\text{B.29})$$

and

$$\hat{\mathbf{H}}_{t_0}^F \equiv \sum_{\tilde{\epsilon}} |u_{\tilde{\epsilon}}(t_0)\rangle \tilde{\epsilon} \langle u_{\tilde{\epsilon}}(t_0)|, \quad (\text{B.30})$$

which allows us to rewrite Eq. B.28 as

$$\hat{\mathbf{U}}(t_1, t_0) = \hat{\mathbf{U}}_F(t_1, t_0) \exp \left[ -i \frac{(t_1 - t_0) \hat{\mathbf{H}}_{t_0}^F}{\hbar} \right] = \exp \left[ -i \frac{(t_1 - t_0) \hat{\mathbf{H}}_{t_1}^F}{\hbar} \right] \hat{\mathbf{U}}_F(t_1, t_0). \quad (\text{B.31})$$

Namely, the full time evolution is separated into two parts:  $\hat{\mathbf{H}}_{t_0}^F$  governs the stroboscopic evolution *with the starting time*  $t_0$ , since

$$\exp \left[ -i \frac{mT \hat{\mathbf{H}}_{t_0}^F}{\hbar} \right] \psi_{\tilde{\epsilon}}(t_0) = e^{-i \frac{mT \tilde{\epsilon}}{\hbar}} \psi_{\tilde{\epsilon}}(t_0) = \psi_{\tilde{\epsilon}}(t_0 + mT), \quad (\text{B.32})$$

while  $\hat{\mathbf{U}}_F(t_1, t_0)$  evolves the periodic part of the Floquet wavefunctions.  $\hat{\mathbf{H}}_{t_0}^F$  and  $\hat{\mathbf{U}}_F(t_1, t_0)$  are respectively called the Floquet Hamiltonian and the micromotion operator.

The most unsettling property of  $\hat{\mathbf{H}}_{t_0}^F$  is its dependence on  $t_0$ . To get rid of it we note that Eq. B.25 implies

$$|u_{\tilde{\epsilon}}(t)\rangle = \sum_{\alpha} \left( \sum_m c_{m\tilde{\epsilon}}^{\alpha} e^{-im\omega t} \right) |\alpha\rangle \equiv \sum_{\alpha} |\alpha\rangle U_{\alpha,\tilde{\epsilon}}(t), \quad (\text{B.33})$$

where the time-independent basis  $|\alpha\rangle$  spans the Hilbert space of  $H(t)$ , and  $U(t)$  is a time-dependent unitary matrix satisfying  $U(t+T) = U(t)$ . Substituting this  $|u_{\tilde{\epsilon}}(t)\rangle$  into Eq. B.15 gives

$$\text{Diag}[\{\tilde{\epsilon}\}] = U^\dagger H(t) U - i\hbar U^\dagger \partial_t U = U^\dagger \tilde{Q} U, \quad (\text{B.34})$$

where  $\text{Diag}[\{\tilde{\epsilon}\}]$  is a diagonal matrix with its eigenvalues being  $\tilde{\epsilon}$ . Comparing this with the effect of a time-dependent unitary transformation of the wavefunction  $\psi' = U^\dagger \psi$  in the Schrödinger equation:

$$i\hbar \partial_t \psi' = (U^\dagger H U - i\hbar U^\dagger \partial_t U) \psi' \equiv H' \psi', \quad (\text{B.35})$$

we can see that  $U$  essentially transforms  $H(t)$  to an effective Hamiltonian  $H' = U^\dagger \tilde{Q} U$  which is time independent. The time evolution of  $\psi$  can thus obtained as

$$\begin{aligned} \psi(t_1) &= U(t_1) \psi'(t_1) = U(t_1) \exp \left[ -i \frac{H'(t_1 - t_0)}{\hbar} \right] \psi'(t_0) \\ &= U(t_1) \exp \left[ -i \frac{H'(t_1 - t_0)}{\hbar} \right] U^\dagger(t_0) \psi(t_0) \\ &= \hat{\mathbf{U}}(t_1, t_0) \psi(t_0). \end{aligned} \quad (\text{B.36})$$

We therefore define

$$\hat{\mathbf{H}}_F \equiv U^\dagger \tilde{Q} U = H' \quad (\text{B.37})$$

as the Floquet effective Hamiltonian, which gives the time-evolution operator

$$\hat{\mathbf{U}}(t_1, t_0) = U(t_1) \exp \left[ -i \frac{\hat{\mathbf{H}}_F(t_1 - t_0)}{\hbar} \right] U^\dagger(t_0). \quad (\text{B.38})$$

Intuitively, this means that the time evolution is obtained by first doing a gauge transformation to the time-independent gauge, evolving the system, and finally gauge-transforming back to the original gauge.

Although we have been assuming that  $U(t)$  diagonalizes  $\bar{Q}$ , this is not necessary. Any time-independent unitary transformation multiplied to  $U(t)$  can still make  $\hat{\mathbf{H}}_F$  time independent. To make connection between the  $t_0$  dependent Floquet Hamiltonian  $\hat{\mathbf{H}}_{t_0}^F$  in Eq. B.30 and the effective Hamiltonian  $\hat{\mathbf{H}}_F$ , we use a minimal  $U(t)$  that is independent of the basis of  $\hat{\mathbf{H}}(t)$ :

$$U_F(t) = \sum_m c_m e^{-im\omega t}, \quad (\text{B.39})$$

which is a time-dependent scalar function. In the matrix form of  $\bar{Q}$ , this  $U_F(t)$  block-diagonalizes  $\bar{Q}$ . All the diagonal blocks have the form  $H_F - m\hbar\omega\mathbf{1}$ . Here we removed the hat of  $H_F$  to indicate that it is a matrix written in certain representation instead of an operator. In this particular representation or gauge,  $|\alpha(t)\rangle = |\alpha\rangle U_F(t)$ . We thus have

$$\hat{\mathbf{H}}_{t_0}^F = \sum_{\tilde{\epsilon}} |u_{\tilde{\epsilon}}(t_0)\rangle \tilde{\epsilon} \langle u_{\tilde{\epsilon}}(t_0)| = \sum_{\alpha\beta} U_F(t_0) |\alpha\rangle (H_F)_{\alpha\beta} \langle\beta| U_F^\dagger(t_0). \quad (\text{B.40})$$

Or loosely speaking  $\hat{\mathbf{H}}_{t_0}^F = U_F(t_0) \hat{\mathbf{H}}_F U_F^\dagger(t_0)$ . Therefore the  $t_0$  dependence in  $\hat{\mathbf{H}}_{t_0}^F$  is only due to a gauge transformation and is not physical. The complete information of time evolution can be obtained from  $H_F$  and  $U_F$  according to Eq. B.38.

In practice, to obtain the quasienergy spectrum or  $H_F$  we simply start from the eigenvalue problem Eq. B.21 for  $\bar{Q} \equiv \bar{H} + \bar{Q}_0$ , where  $\bar{H}_{m,m+n} = H_n$  and  $(\bar{Q}_0)_{m,m+n} = -m\hbar\omega\delta_{n0}$ . We can either use perturbation theory and treat  $\bar{H}$  as perturbation, which is accurate in the high-frequency limit, or directly diagonalize  $\bar{Q}$  with a large enough cutoff. The first several terms in the perturbation series of  $H_F$  are given in Eqs. 86-89 in [77] ( $m$  there should be  $-m$  in our notation).

## B.4 High Frequency (Van Vleck) expansion from degenerate perturbation theory

In order to understand the effects of coherent time-periodic modulation of quantum systems, we need an efficient method to obtain the Floquet Hamiltonian  $\hat{\mathbf{H}}^F$  for a given time-dependent Hamiltonian  $\hat{\mathbf{H}}(\tau)$ . Generally, for the Floquet systems, one would like to obtain a suitable Hamiltonian  $\hat{\mathbf{H}}(\tau)$  given a desired static Hamiltonian  $\hat{\mathbf{H}}_{\text{eff}}$ . Usually the formal approach in making use of the full eigenstates of a time-dependent model Hamiltonian is not feasible in practice. Therefore, one requires an approximate scheme that still provides a valid description at least on the time-scales and energy-scales. Such an approach is provided by high-frequency approximations [77, 84–88]. Using the Van Vleck expansion within the degenerate perturbation theory as shown in Ref. [77], we can write the explicit expressions for the first few terms with  $n = 0, 1, 2$  as required;

$$\hat{\mathbf{H}}^{F(0)} = 0, \quad (\text{B.41})$$

$$\hat{\mathbf{H}}^{F(1)} = \hat{\mathbf{H}}_0, \quad (\text{B.42})$$

$$\begin{aligned} \hat{\mathbf{H}}^{F(2)} &= \sum_{m \neq 0} \frac{[\hat{\mathbf{H}}_m, \hat{\mathbf{H}}_{-m}]}{m\hbar\omega}, \\ \hat{\mathbf{H}}^{F(3)} &= \sum_{m \neq 0} \left( \frac{[\hat{\mathbf{H}}_{-m}, [\hat{\mathbf{H}}_0, \hat{\mathbf{H}}_m]]}{2(m\hbar\omega)^2} + \sum_{m' \neq 0, m} \frac{[\hat{\mathbf{H}}_{-m'}, [\hat{\mathbf{H}}_{m'-m}, \hat{\mathbf{H}}_m]]}{3mm'(\hbar\omega)^2} \right). \end{aligned}$$

Expressions for higher orders can be found in the above equations and refs. [77, 84–88]. From a practical point of view, and in the cases which we will be considering, one often engineers the time-dependent Hamiltonian in such a way that the approximate Floquet Hamiltonian  $\hat{\mathbf{H}}_{\text{eff}} = \sum_{n=0}^m H^{F(n)}$  corresponds to the desired model Hamiltonian of the effective systems.

Some of the commutators are related by transpose or Hermitian conjugate. As an example in  $H^{F(2)}$  the transpose reduces the sum down by

$$\frac{[H_m, H_{-m}]}{m\hbar\omega} + \frac{[H_{-m}, H_m]}{-m\hbar\omega} = \frac{[H_m, H_{-m}]}{m\hbar\omega} + \frac{[H_m, H_{-m}]}{m\hbar\omega} \quad (\text{B.43})$$

$$= 2 \frac{[H_m, H_{-m}]}{m\hbar\omega} \quad (\text{B.44})$$

Additionally, an example in  $H^{F(3)}$  the Hermitian conjugate reduces the sum down by

$$\begin{aligned} [H_{-m'}, [H_{m'-m}, H_m]]^\dagger &= [[H_{m'-m}, H_m]^\dagger, H_{-m'}^\dagger] \\ &= [[H_m^\dagger, H_{m'-m}^\dagger], H_{m'}] \\ &= [[H_{-m}, H_{m-m'}], H_{m'}] \\ &= [H_{m'}, [H_{m-m'}, H_{-m}]] \end{aligned} \quad (\text{B.45})$$

or in general the following identity

$$[A, [B, C]]^\dagger = [A^\dagger, [B^\dagger, C^\dagger]]. \quad (\text{B.46})$$

With the symmetry in modes we have the following simplification

$$\frac{[H_{-m'}, [H_{m'-m}, H_m]]}{mm'(\hbar\omega)^2} + \frac{[H_{m'}, [H_{m-m'}, H_{-m}]]}{(-m)(-m')(\hbar\omega)^2} = \frac{[H_{-m'}, [H_{m'-m}, H_m]] + h.c.}{mm'(\hbar\omega)^2} \quad (\text{B.47})$$

We can reduce the second and third perturbation summation terms to

$$H^{F(2)} = \sum_{m>0} \frac{2[H_m, H_{-m}]}{m\hbar\omega} \quad (\text{B.48})$$

$$H^{F(3)} = \sum_{m>0} \left( \frac{[H_{-m}, [H_0, H_m]] + h.c.}{2(m\hbar\omega)^2} + \sum_{m' \neq m} \frac{[H_{-m'}, [H_{m'-m}, H_m]] + h.c.}{3mm'(\hbar\omega)^2} \right) \quad (\text{B.49})$$

### B.4.1 Non-uniform circularly polarized light on Dirac

We start with the Dirac equation in 2D with a gauge potential

$$\mathcal{H}(t) = v_F \boldsymbol{\sigma} \cdot (\mathbf{p} + e\mathbf{A}(t)) \quad (\text{B.50})$$

where  $\mathbf{A}(t) = \frac{E}{\omega} \langle -\sin \omega t, \frac{1}{2} \sin(Kx) \cos(2\omega t) \rangle$ . Which is made up of two electromagnetic wave sources. The time dependent Hamiltonian becomes

$$\mathcal{H}(t) = v_F \left( \sigma_x \left( p_x - \frac{eE}{\omega} \sin \omega t \right) + \sigma_y \left( p_y + \frac{eE}{2\omega} \sin(Kx) \cos(2\omega t) \right) \right), \quad (\text{B.51})$$

Performing the Fourier time-transform from

$$H_n = \frac{1}{T} \int_0^T \mathcal{H}(t) e^{-in\omega t} dt \quad (\text{B.52})$$

gives the following terms

$$H_0 = v_F \boldsymbol{\sigma} \cdot \mathbf{p} \quad (\text{B.53})$$

$$H_{\pm 1} = \pm \sigma_x \frac{i v_F e E}{2\omega} \quad (\text{B.54})$$

$$H_{\pm 2} = \sigma_y \frac{v_F e E}{4\omega} \sin(Kx). \quad (\text{B.55})$$

We compute the following Hermitian commutators for the high-frequency expansion

$$[H_1, H_{-1}] \tag{B.56}$$

$$[H_2, H_{-2}] \tag{B.57}$$

$$[H_{-1}, [H_0, H_1]] \tag{B.58}$$

$$[H_{-2}, [H_0, H_2]] \tag{B.59}$$

$$[H_1, [H_{-2}, H_1]] \tag{B.60}$$

$$[H_{-1}, [H_{-1}, H_2]]. \tag{B.61}$$

We find each term to be

$$[H_1, H_{-1}] = [H_2, H_{-2}] = 0 \tag{B.62}$$

$$H^{F(2)} = 0. \tag{B.63}$$

$$\begin{aligned}
[H_0, H_{\pm 1}] &= \pm \sigma_z \frac{v_F^2 e E}{\omega} p_y \\
[H_1, [H_0, H_{-1}]] &= -\sigma_y \frac{v_F^3 e^2 E^2}{\omega^2} p_y
\end{aligned} \tag{B.64}$$

$$\begin{aligned}
[H_0, H_{\pm 2}] &= \pm i \sigma_z \frac{v_F^2 e E}{4\omega} (p_x \sin(Kx) + \sin(Kx) p_x) \\
[H_2, [H_0, H_{-2}]] &= -\sigma_x \frac{v_F^3 e^2 E^2}{2\omega^2} (p_x \sin^2(Kx) + \sin^2(Kx) p_x)
\end{aligned} \tag{B.65}$$

$$\begin{aligned}
[H_{\pm 1}, H_2] &= \mp \sigma_z \left( \frac{v_F e E}{2\omega} \right)^2 \sin(Kx) \\
[H_1, [H_{-2}, H_{-1}]] &= -\sigma_y \frac{v_F^3 e^3 E^3}{4\omega^3} \sin(Kx)
\end{aligned} \tag{B.66}$$

$$[H_{-1}, [H_{-1}, H_2]] = \sigma_y \frac{v_F^3 e^3 E^3}{4\omega^3} \sin(Kx) \tag{B.67}$$

Piecing each term together

$$\begin{aligned}
H^{F(3)} &= \frac{[H_1, [H_0, H_{-1}]]}{2\hbar^2 \omega^2} + \frac{[H_{-2}, [H_0, H_2]]}{8\hbar^2 \omega^2} - \frac{[H_1, [H_{-2}, H_1]]}{3\hbar^2 \omega^2} + \frac{[H_{-1}, [H_{-1}, H_2]]}{6\hbar^2 \omega^2} + h.c. \\
&= -\sigma_y \frac{v_F^3 e^2 E^2}{\hbar^2 \omega^4} p_y - \sigma_x \frac{v_F^3 e^2 E^2}{8\hbar^2 \omega^4} \{p_x, \sin^2(Kx)\} + \sigma_y \frac{v_F^3 e^3 E^3}{4\hbar^2 \omega^5} \sin(Kx).
\end{aligned} \tag{B.68}$$

The full Hamiltonian to second order in  $\hbar\omega$  becomes

$$H_{\text{eff}} = v_F \boldsymbol{\sigma} \cdot \mathbf{p} - \sigma_y \frac{v_F^3 e^2 E^2}{\hbar^2 \omega^4} p_y - \sigma_x \frac{v_F^3 e^2 E^2}{8\hbar^2 \omega^4} \{p_x, \sin^2(Kx)\} + \sigma_y \frac{v_F^3 e^3 E^3}{4\hbar^2 \omega^5} \sin(Kx). \tag{B.69}$$

#### B.4.2 Non-uniform circularly polarized light on 2DEG

We start with the Schrodinger equation in 2D with a gauge potential field



$$\mathcal{H}(t) = \frac{(\mathbf{p} + e\mathbf{A}(t))^2}{2m^*} \quad (\text{B.70})$$

where  $\mathbf{A}(t) = \frac{E}{\omega} \langle -\sin \omega t, \cos(Kx) \cos \omega t \rangle$ . Which is made up of two electromagnetic wave sources.

The time dependent Hamiltonian becomes

$$\begin{aligned} \mathcal{H}(t) = \frac{1}{2m^*} & \left[ p_x^2 + p_y^2 + \frac{e^2 E^2}{2\omega^2} (1 + \cos^2(Kx)) + \frac{e^2 E^2}{2\omega^2} \sin^2(Kx) \cos 2\omega t \right. \\ & \left. + \frac{2eE}{\omega} p_y \cos(Kx) \cos \omega t - \frac{2eE}{\omega} p_x \sin \omega t \right] \end{aligned} \quad (\text{B.71})$$

Performing the Fourier time-transform from

$$H_n = \frac{1}{T} \int_0^T \mathcal{H}(t) e^{-in\omega t} dt \quad (\text{B.72})$$

gives the following terms

$$H_0 = \frac{1}{2m^*} \left( p_x^2 + p_y^2 + \frac{e^2 E^2}{2\omega^2} (1 + \cos^2(Kx)) \right) \quad (\text{B.73})$$

$$H_{\pm 1} = \frac{1}{2m^*} \frac{eE}{\omega} (\pm i p_x + p_y \cos(Kx)) \quad (\text{B.74})$$

$$H_{\pm 2} = -\frac{1}{2m^*} \frac{e^2 E^2}{4\omega^2} \sin^2(Kx) \quad (\text{B.75})$$

We compute the following Hermitian commutators for the high-frequency expansion

$$[H_1, H_{-1}] = -\frac{1}{2m^*} \frac{\hbar K e^2 E^2}{\omega^2} p_y \sin(Kx) \quad (\text{B.76})$$

$$[H_2, H_{-2}] = 0 \quad (\text{B.77})$$

then

$$H^{F(2)} = \frac{2[H_1, H_{-1}]}{\hbar\omega} = -\frac{1}{2m^*} \frac{2Ke^2E^2}{\omega^3} p_y \sin(Kx) \quad (\text{B.78})$$

The full Hamiltonian to first order in  $\hbar\omega$  becomes

$$H_{\text{eff}} = \frac{1}{2m^*} \left( p_x^2 + p_y^2 + \frac{e^2E^2}{2\omega^2} (1 + \cos^2(Kx)) - \frac{2Ke^2E^2}{\omega^3} p_y \sin(Kx) \right). \quad (\text{B.79})$$

We can further manipulate by shifting the energy by a constant and completing the square w.r.t.  $p_y$  and  $\sin(Kx)$  terms to get

$$H_{\text{eff}} = \frac{1}{2m^*} \left( p_x^2 + \left( p_y - \frac{Ke^2E^2}{m^*\omega^3} \sin(Kx) \right)^2 + \frac{e^2E^2}{2\omega^2} \cos^2(Kx) - \frac{K^2e^4E^4}{m^{*2}\omega^6} \sin^2(Kx) \right). \quad (\text{B.80})$$

## B.5 Tight-binding model Dirac

We start with a nearest-neighbor single-orbital tight-binding Hamiltonian

$$\mathcal{H} = - \sum_{jl\alpha, j'l'\beta} \hbar c_{jl\alpha}^\dagger c_{j'l'\beta} + h.c. \quad (\text{B.81})$$

The incident laser beam in vector potential forms looks like

$$\mathbf{A}(\mathbf{r}, t) = \frac{E}{\omega} \langle -\sin \omega t, \frac{1}{2} \sin(Kx) \cos 2\omega t \rangle. \quad (\text{B.82})$$

Using the following approximation for smoothly varying vector potential fields

$$\int_{\mathbf{r}_{j,l}^\alpha}^{\mathbf{r}_{j',l'}^\beta} \mathbf{A}(\mathbf{r}, t) \cdot d\mathbf{l} \approx \mathbf{A} \left( \frac{\mathbf{r}_{j',l'}^\beta + \mathbf{r}_{j,l}^\alpha}{2}, t \right) \cdot (\mathbf{r}_{j',l'}^\beta - \mathbf{r}_{j,l}^\alpha) \quad (\text{B.83})$$

where

$$\mathbf{a}_1 = \sqrt{3}a\hat{\mathbf{x}} \quad (\text{B.84})$$

$$\mathbf{a}_2 = 3a\hat{\mathbf{y}} \quad (\text{B.85})$$

$$\mathbf{r}_{jl}^{A_1} = j\mathbf{a}_1 + l\mathbf{a}_2 \quad (\text{B.86})$$

$$\mathbf{r}_{jl}^{B_1} = (j + \frac{1}{2})\mathbf{a}_1 + (l + \frac{1}{6})\mathbf{a}_2 \quad (\text{B.87})$$

$$\mathbf{r}_{jl}^{A_2} = (j + \frac{1}{2})\mathbf{a}_1 + (l + \frac{1}{2})\mathbf{a}_2 \quad (\text{B.88})$$

$$\mathbf{r}_{jl}^{B_2} = (j + 1)\mathbf{a}_1 + (l + \frac{2}{3})\mathbf{a}_2. \quad (\text{B.89})$$

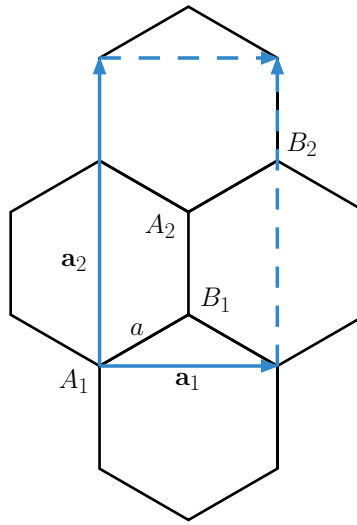


**Figure B.1:** Unit cell for dirac system with gauge potential with translation symmetry in the  $y$ -axis described by Eq. (B.82).

Applying a Peierls substitution the Hamiltonian becomes

$$\begin{aligned}
\mathcal{H}(t) = & - \sum_{jl} h_{jlA_1}^{j l B_1}(t) c_{jlA_1}^\dagger c_{jlB_1} + h_{jlB_1}^{j l A_2}(t) c_{jlB_1}^\dagger c_{jlA_2} + h_{jlA_2}^{j l B_2}(t) c_{jlA_2}^\dagger c_{jlB_2} \\
& + h_{jlB_1}^{j+1, l A_1}(t) c_{jlB_1}^\dagger c_{j+1, l A_1} + h_{jlB_2}^{j+1, l, A_2} c_{jlB_2}^\dagger c_{j+1, l A_2}(t) \\
& + h_{jlB_2}^{j+1, l+1, A_1}(t) c_{jlB_2}^\dagger c_{j+1, l+1, A_1} + h.c.
\end{aligned} \tag{B.90}$$

where in general

$$h_{jl\alpha}^{j'l'\beta}(t) \approx h \exp \left[ i\phi_0 \left( -\frac{x_{j'l'}^\beta - x_{jl}^\alpha}{a} \sin \omega t + \frac{y_{j'l'}^\beta - y_{jl}^\alpha}{2a} \cos \left( K \frac{x_{j'l'}^\beta + x_{jl}^\alpha}{2} \right) \cos 2\omega t \right) \right], \tag{B.91}$$

where  $\phi_0 = eE/(\hbar\omega)$ . More explicitly for each term

$$h_{jlA_1}^{j l B_1}(t) \approx h \exp \left[ i\phi_0 \left( -\frac{\sqrt{3}}{2} \sin \omega t + \frac{1}{4} \sin \left( \sqrt{3} K a (j + \frac{1}{4}) \right) \cos 2\omega t \right) \right] \tag{B.92}$$

$$h_{jlB_1}^{j l A_2}(t) \approx h \exp \left[ i\phi_0 \left( \frac{1}{2} \sin \left( \sqrt{3} K a (j + \frac{1}{2}) \right) \cos 2\omega t \right) \right] \tag{B.93}$$

$$h_{jlA_2}^{j l B_2}(t) \approx h \exp \left[ i\phi_0 \left( -\frac{\sqrt{3}}{2} \sin \omega t + \frac{1}{4} \sin \left( \sqrt{3} K a (j + \frac{3}{4}) \right) \cos 2\omega t \right) \right] \tag{B.94}$$

$$h_{jlB_1}^{j+1, l A_1}(t) \approx h \exp \left[ i\phi_0 \left( -\frac{\sqrt{3}}{2} \sin \omega t - \frac{1}{4} \sin \left( \sqrt{3} K a (j + \frac{3}{4}) \right) \cos 2\omega t \right) \right] \tag{B.95}$$

$$h_{jlB_2}^{j+1, l A_2}(t) \approx h \exp \left[ i\phi_0 \left( -\frac{\sqrt{3}}{2} \sin \omega t - \frac{1}{4} \sin \left( \sqrt{3} K a (j + \frac{5}{4}) \right) \cos 2\omega t \right) \right] \tag{B.96}$$

$$h_{jlB_2}^{j+1, l+1, A_1}(t) \approx h \exp \left[ i\phi_0 \left( \frac{1}{2} \sin \left( \sqrt{3} K a (j + 1) \right) \cos 2\omega t \right) \right] \tag{B.97}$$

The incident laser beam allows for translation symmetry along the y-axis, so we can reduce the dimension of the Hamiltonian with the following Fourier transform

$$c_{jl\alpha}^\dagger = \frac{1}{N_y} \sum_k c_{jk\alpha}^\dagger e^{ik\hat{\mathbf{y}} \cdot \mathbf{R}_l} = \frac{1}{N_y} \sum_k c_{jk\alpha}^\dagger e^{ik(3la)} \quad (\text{B.98})$$

The Hamiltonian then becomes

$$\begin{aligned} \mathcal{H}(t) = & - \sum_{jk} h_{jlA_1}^{jLB_1}(t) c_{jkA_1}^\dagger c_{jkB_1} + h_{jlB_1}^{jLA_2}(t) c_{jkB_1}^\dagger c_{jkA_2} + h_{jlA_2}^{jLB_2}(t) c_{jkA_2}^\dagger c_{jkB_2} \\ & + h_{jlB_1}^{j+1,LA_1}(t) c_{jkB_1}^\dagger c_{j+1,kA_1} + h_{jlB_2}^{j+1,L,A_2}(t) c_{jkB_2}^\dagger c_{j+1,kA_2} \\ & + h_{jlB_2}^{j+1,l+1,A_1}(t) e^{-i3ka} c_{jkB_2}^\dagger c_{j+1,kA_1} + h.c. \end{aligned} \quad (\text{B.99})$$

Making use of Floquet theory we can make the Hamiltonian time-independent with the following time domain Fourier transform

$$H_{ab,n,k} = \frac{1}{2\pi} \int_0^{2\pi} \mathcal{H}_{ab}(k, t) e^{-in\tau} d\tau \quad (\text{B.100})$$

where  $a, b$  represent the matrix indices of the previous Hamiltonian and  $n$  is the  $n$ -th order mode of light. Each term has the general following form

$$H_{ab,n,k} = \frac{1}{2\pi} \int_0^{2\pi} e^{iZ_1 \sin \tau + iZ_2 \cos 2\tau - in\tau} d\tau \quad (\text{B.101})$$

which looks a lot like the Hansen-Bessel integral function. However, because of the linear combination of  $\sin \tau$  and  $\cos 2\tau$ , there is no elementary solution to the integral as currently defined. We thus solve the integral numerically for each given  $n$ . After the time domain Fourier transform the Hamiltonian can be reduced to the following matrix form

$$H_n = - \sum_{jk} \left[ \Psi_{jk}^\dagger H_{jj} \Psi_{jk} + \Psi_{jk}^\dagger H'_{j,j+1,k} \Psi_{j+1,k} + h.c. \right] \quad (\text{B.102})$$

$$H_{j,j} = \begin{bmatrix} 0 & 0 & 0 & 0 \\ h_{jlB_1}^{jLA_1} & 0 & 0 & 0 \\ 0 & h_{jlA_2}^{jLB_1} & 0 & 0 \\ 0 & 0 & h_{jlB_2}^{jLA_2} & 0 \end{bmatrix}$$

and

$$H'_{j,j+,k} = \begin{bmatrix} 0 & h_{jlB_1}^{j+1,LA_1} & 0 & h_{jlB_2}^{j+1,L+1,A_1} e^{i\mathbf{k} \cdot \mathbf{a}_2} \\ 0 & 0 & 0 & 0 \\ 0 & 0 & 0 & h_{jlB_2}^{j+1,LA_2} \\ 0 & 0 & 0 & 0 \end{bmatrix},$$

with  $\mathbf{k} = k\hat{\mathbf{y}}$  and  $\Psi_{jk} = [c_{jkA_1}, c_{jkB_1}, c_{jkA_2}, c_{jkB_2}]^T$ .

The quasienergy energy matrix has elements  $Q_{m,m+n} = H_n - m\hbar\omega\delta_{n0}$ . We choose a cutoff for mode  $m$ ,  $|m| \leq m_c$ , where  $m_c$  is a positive integer. This cuts the matrix down to have  $N_m = 2m_c + 1$  diagonal blocks, where each block is of size a  $N_S = 2r_c + 1$  square matrix,  $H_n$ , and  $r_c$  is the cutoff radius of unit cells. The matrix can be solved using an eigenvalue solver, producing  $N_m N_S$  eigenenergies and eigenvectors for a given electric field strength  $E$ . It is difficult to glean any information from looking at all the energies but one can do a projection to the  $m = 0$  mode to highlight which energies belong to it. This is still not all that imformative because when using a finite system we discretize the brillouin zone uniformly and it does not necessarily mean we are picking energy values close to the folded in Dirac point, since the unperturbed brillouin zone gets folded into the perturbed smaller brillouin zone.

## B.6 Tight-binding model 2DEG

We start with a nearest-neighbor single-orbital tight-binding Hamiltonian on a square lattice

$$\mathcal{H} = \sum_{j,l} -h(c_{j,l}^\dagger c_{j+1,l} + c_{j,l}^\dagger c_{j,l+1} + h.c.) \quad (\text{B.103})$$

The incident laser beam as a vector potential is as follows

$$\mathbf{A}(\mathbf{r}, t) = \frac{E}{\omega} \langle -\sin \omega t, \cos(Kx) \cos \omega t \rangle. \quad (\text{B.104})$$

Using the following approximation for smoothly varying vector potential fields

$$\int_{\mathbf{r}_a}^{\mathbf{r}_b} \mathbf{A}(\mathbf{r}, t) \cdot d\mathbf{l} \approx \mathbf{A}\left(\frac{\mathbf{r}_b + \mathbf{r}_a}{2}, t\right) \cdot (\mathbf{r}_b - \mathbf{r}_a) \quad (\text{B.105})$$

and using Peierls substitution the Hamiltonian becomes

$$\mathcal{H}(t) = - \sum_{j,l} (h_{j,j+1}(t) c_{j,l}^\dagger c_{j+1,l} + h_{l,l+1}(t) c_{j,l}^\dagger c_{j,l+1} + h.c.), \quad (\text{B.106})$$

where

$$\begin{aligned} h_{j,j+1}(t) &\approx h \exp\left(-i \frac{eEa}{\hbar\omega} \frac{x_{j+1} - x_j}{a} \sin \omega t\right) \\ &= h \exp(-i\phi_0 \sin \omega t) \end{aligned} \quad (\text{B.107})$$

$$\begin{aligned} h_{l,l+1}(t) &\approx h \exp\left(i \frac{eEa}{\hbar\omega} \frac{y_{l+1} - y_l}{a} \cos(Kx_j) \cos \omega t\right) \\ &= h \exp(i\phi_0 \cos(Kx_j) \cos \omega t). \end{aligned} \quad (\text{B.108})$$

The incident laser beam allows for translation symmetry along the y-axis, so we can reduce the dimension of the Hamiltonian with the following Fourier transform

$$c_{j,l}^\dagger = \frac{1}{\sqrt{N_y}} \sum_k c_{j,k}^\dagger e^{ik\hat{\mathbf{y}} \cdot \mathbf{r}_l} = \frac{1}{\sqrt{N_y}} \sum_k c_{j,k}^\dagger e^{ikla}. \quad (\text{B.109})$$

The Hamiltonian then becomes

$$\mathcal{H}(t) = \sum_{j,k} (h_{l,l+1}(t)e^{-ika} + h_{l,l+1}^*(t)e^{ika})c_{j,k}^\dagger c_{j,k} + (h_{j,j+1}(t)c_{j,k}^\dagger c_{j+1,k} + h.c.) \quad (\text{B.110})$$

$$= \sum_{j,k} 2h \cos(\phi_0 \cos(Kx_j) \cos \omega t - ka) c_{j,k}^\dagger c_{j,k} + (h e^{i\phi_0 \sin \omega t} c_{j,k}^\dagger c_{j+1,k} + h.c.). \quad (\text{B.111})$$

Making use of Floquet theory we can make the Hamiltonian time-independent with the following time Fourier transform

$$\mathcal{H}_{ab,n}(k) = \frac{1}{T} \int_0^T \mathcal{H}_{ab}(k, t) e^{-in\omega t} dt \quad (\text{B.112})$$

$$= \frac{1}{2\pi} \int_0^{2\pi} \mathcal{H}_{ab}(k, t) e^{-in\tau} d\tau \quad (\text{B.113})$$

where  $a, b$  represent the matrix index of the previous Hamiltonian and  $n$  is the  $n$ -th order mode of light. We will make use of the following Hansen-Bessel integral formulas

$$J_n(z) = \frac{1}{2\pi} \int_0^{2\pi} e^{in\tau - z \sin \tau} d\tau = \frac{1}{2\pi} \int_0^{2\pi} e^{in\tau - in\pi/2 + z \cos \tau} d\tau, \quad (\text{B.114})$$

note that the integral bound can be the same due to the integrand being periodic from  $[0, 2\pi]$ .

Recall, Bessel function identities for  $n \in \mathbb{Z}$

$$J_n(-z) = (-1)^n J_n(z) \quad (\text{B.115})$$

$$J_{-n}(z) = (-1)^n J_n(z) \quad (\text{B.116})$$

The terms for given  $k$  become the following time Fourier transforms



$$\begin{aligned}
\mathcal{H}_{j,j,n}(k) &= -\frac{h}{2\pi} \int_0^{2\pi} \left( e^{i\phi_0 \cos(Kx_j) \cos \tau - ika - in\tau} + e^{-i\phi_0 \cos(Kx_j) \cos \tau + ika - in\tau} \right) d\tau \\
&= -h \left( \frac{e^{-ika}}{2\pi} \int_0^{2\pi} e^{iz \cos \tau - in\tau} d\tau + \frac{e^{ika}}{2\pi} \int_0^{2\pi} e^{-iz \cos \tau - in\tau} d\tau \right) \\
&= -h \left( \frac{e^{-ika - in\pi/2}}{2\pi} \int_0^{2\pi} e^{iz \cos \tau - in\tau + in\pi/2} d\tau + \frac{e^{ika - in\pi/2}}{2\pi} \int_0^{2\pi} e^{-iz \cos \tau - in\tau + in\pi/2} d\tau \right) \\
&= -he^{-in\pi/2} \left( J_{-n}(z) e^{-ika} + J_{-n}(-z) e^{ika} \right) \\
&= -hJ_n(z) e^{-in\pi/2} (e^{ika} + e^{-ika + in\pi}) \\
&= -hJ_n(z) (e^{i(ka - n\pi/2)} + e^{-i(ka - n\pi/2)}) \\
&= -2hJ_n(\phi_0 \cos(Kx_j)) \cos(ka - n\pi/2)
\end{aligned} \tag{B.117}$$

and

$$\begin{aligned}
\mathcal{H}_{j,j+1,n} &= -\frac{h}{2\pi} \int_0^{2\pi} e^{-i\phi_0 \sin \tau - in\tau} d\tau \\
&= -hJ_{-n}(\phi_0) \\
&= -h(-1)^n J_n(\phi_0)
\end{aligned} \tag{B.118}$$

$$\begin{aligned}
\mathcal{H}_{j+1,j,n} &= -\frac{h}{2\pi} \int_0^{2\pi} e^{i\phi_0 \sin \tau - in\tau} d\tau \\
&= -hJ_{-n}(-\phi_0) \\
&= -hJ_n(\phi_0)
\end{aligned} \tag{B.119}$$

This completes finding all the matrix terms for the quasienergy matrix  $\bar{Q}$  for a 2DEG tight binding model with incident inhomogeneous laser light.

## B.7 Chern number of Landau levels

In this section we discuss how to understand the Chern number of Landau levels. For two-dimensional periodic systems, the 2D Brillouin zone is a closed manifold, and one can define the Chern number as a topological invariant for the mapping between complex functions (ground state wavefunctions) and this manifold. However, for Landau levels the system does not have translational symmetry which causes a conceptual difficulty in defining Chern numbers.

To address this difficulty, let us start from the Chern number of typical 2D Bloch Hamiltonians. The Berry curvature of band  $n$  at crystal momentum  $\mathbf{k}$  is defined as

$$\Omega_{n\mathbf{k}} = \hat{\mathbf{z}} \cdot (\nabla_{\mathbf{k}} \times \mathbf{A}_{n\mathbf{k}}) = \hat{\mathbf{z}} \cdot (\nabla_{\mathbf{k}} \times \langle u_{n\mathbf{k}} | i \nabla_{\mathbf{k}} | u_{n\mathbf{k}} \rangle) \quad (\text{B.120})$$

The Chern number for band  $n$ , which must not touch other bands throughout the Brillouin zone, is defined as

$$C_n = \int \frac{d^2\mathbf{k}}{2\pi} \Omega_{n\mathbf{k}} \quad (\text{B.121})$$

However, according to Eq. (B.120),  $C_n$  can be rewritten into

$$\begin{aligned} C_n &= \int \frac{d^2\mathbf{k}}{2\pi} \partial_{k_x} \langle u_{n\mathbf{k}} | i \partial_{k_y} | u_{n\mathbf{k}} \rangle - \int \frac{d^2\mathbf{k}}{2\pi} \partial_{k_y} \langle u_{n\mathbf{k}} | i \partial_{k_x} | u_{n\mathbf{k}} \rangle \\ &= \frac{1}{2\pi} \int dk_x \partial_{k_x} \int dk_y \langle u_{n\mathbf{k}} | i \partial_{k_y} | u_{n\mathbf{k}} \rangle - \frac{1}{2\pi} \int dk_y \partial_{k_y} \int dk_x \langle u_{n\mathbf{k}} | i \partial_{k_x} | u_{n\mathbf{k}} \rangle \end{aligned} \quad (\text{B.122})$$

It is worth noting that the last result is related to the expectation value of polarization (or position operator) in a Bloch state:

$$\begin{aligned}
\langle n\mathbf{k}|\mathbf{r}|n'\mathbf{k}'\rangle &= \int d^2\mathbf{r} \psi_{n'\mathbf{k}'}^\dagger(\mathbf{r}) \mathbf{r} \psi_{n\mathbf{k}}(\mathbf{r}) \\
&= \int d^2\mathbf{r} u_{n\mathbf{k}}^\dagger(\mathbf{r}) e^{-i\mathbf{k}\cdot\mathbf{r}} \mathbf{r} e^{i\mathbf{k}'\cdot\mathbf{r}} u_{n'\mathbf{k}'}(\mathbf{r}) \\
&= \int d^2\mathbf{r} u_{n\mathbf{k}}^\dagger(\mathbf{r}) e^{-i\mathbf{k}\cdot\mathbf{r}} (-i\partial_{\mathbf{k}'} e^{i\mathbf{k}'\cdot\mathbf{r}}) u_{n'\mathbf{k}'}(\mathbf{r}) \\
&= -i\partial_{\mathbf{k}'} \langle n\mathbf{k}|n'\mathbf{k}'\rangle + \int d^2\mathbf{r} u_{n\mathbf{k}}^\dagger(\mathbf{r}) e^{-i\mathbf{k}\cdot\mathbf{r}} e^{i\mathbf{k}'\cdot\mathbf{r}} [i\partial_{\mathbf{k}'} u_{n'\mathbf{k}'}(\mathbf{r})] \\
&= -i\delta_{nn'} \frac{(2\pi)^2}{V_{\text{uc}}} \partial_{\mathbf{k}'} \delta(\mathbf{k}-\mathbf{k}') + \int d^2\mathbf{r} u_{n\mathbf{k}}^\dagger(\mathbf{r}) e^{-i\mathbf{k}\cdot\mathbf{r}} e^{i\mathbf{k}'\cdot\mathbf{r}} [i\partial_{\mathbf{k}'} u_{n'\mathbf{k}'}(\mathbf{r})] \\
&= -i\delta_{nn'} \frac{(2\pi)^2}{V_{\text{uc}}} \partial_{\mathbf{k}'} \delta(\mathbf{k}-\mathbf{k}') + \sum_{\mathbf{R}} \int_{\text{uc}} d^2\mathbf{r} u_{n\mathbf{k}}^\dagger(\mathbf{r}) e^{i(\mathbf{k}'-\mathbf{k})\cdot\mathbf{r}} [i\partial_{\mathbf{k}'} u_{n'\mathbf{k}'}(\mathbf{r})] e^{i(\mathbf{k}'-\mathbf{k})\cdot\mathbf{R}} \\
&= -i\delta_{nn'} \frac{(2\pi)^2}{V_{\text{uc}}} \partial_{\mathbf{k}'} \delta(\mathbf{k}-\mathbf{k}') + \frac{(2\pi)^2}{V_{\text{uc}}} \delta(\mathbf{k}-\mathbf{k}') \int_{\text{uc}} d^2\mathbf{r} u_{n\mathbf{k}}^\dagger(\mathbf{r}) [i\partial_{\mathbf{k}'} u_{n'\mathbf{k}'}(\mathbf{r})] e^{i(\mathbf{k}'-\mathbf{k})\cdot\mathbf{R}} \\
&= \frac{(2\pi)^2}{V_{\text{uc}}} [i\delta_{nn'} \partial_{\mathbf{k}} \delta(\mathbf{k}-\mathbf{k}') + \langle u_{n\mathbf{k}}|i\partial_{\mathbf{k}}|u_{n'\mathbf{k}'}\rangle \delta(\mathbf{k}-\mathbf{k}')]
\end{aligned} \tag{B.123}$$

where we have used the normalization condition of 2D Bloch states  $\langle n\mathbf{k}|n'\mathbf{k}'\rangle = \delta_{nn'} \frac{(2\pi)^2}{V_{\text{uc}}} \delta(\mathbf{k}-\mathbf{k}')$  with  $V_{\text{uc}}$  the unit cell volume or area. The above result means that

$$\begin{aligned}
\frac{a_y}{2\pi} \int dk_y \langle n\mathbf{k}|\mathbf{r}|n\mathbf{k}\rangle &\equiv N \mathbf{r}_n(k_x) = \frac{a_y}{2\pi} \int dk_y \lim_{\mathbf{k}' \rightarrow \mathbf{k}} \langle n\mathbf{k}|\mathbf{r}|n\mathbf{k}'\rangle \\
&= \frac{a_y}{2\pi} N \int dk_y \langle u_{n\mathbf{k}}|i\partial_{\mathbf{k}}|u_{n\mathbf{k}}\rangle
\end{aligned} \tag{B.124}$$

where  $a_y$  is the lattice constant along  $y$ . Namely

$$\frac{1}{2\pi} \int dk_y \langle u_{n\mathbf{k}}|i\partial_{\mathbf{k}}|u_{n\mathbf{k}}\rangle = \frac{\mathbf{r}_n(k_x)}{a_y}. \tag{B.125}$$

Therefore

$$\begin{aligned}
C_n &= \frac{1}{a_y} \int dk_x \partial_{k_x} y_n(k_x) - \frac{1}{a_x} \int dk_y \partial_{k_y} x_n(k_y) \\
&= \frac{1}{a_y} \left[ y_n|_{k_x=\frac{2\pi}{a_x}} - y_n|_{k_x=0} \right] - \frac{1}{a_x} \left[ x_n|_{k_y=\frac{2\pi}{a_x}} - x_n|_{k_y=0} \right] \\
&\equiv \frac{\Delta y_n}{a_y} - \frac{\Delta x_n}{a_x}
\end{aligned} \tag{B.126}$$

In other words, the Chern number can be understood as an effect of adiabatic pumping. The parameter defining the pump is  $k_x$  (1st term in the above equation) or  $k_y$  (2nd term in the above equation). When the pumping parameter increases by a period, the expectation value of the position operator  $y_n$  (or  $x_n$ ) for the given band does not necessarily return to itself. A nonzero change leads to the finite Chern number. A caveat that is not mentioned in many references or textbooks is that since  $\mathbf{A}_{n\mathbf{k}}$  is not a gauge invariant quantity, the two individual terms in the last line of Eq. (B.126) are not separately well defined. Instead, one can choose a gauge so that  $A_x(k_y=0) = A_x(k_y=\frac{2\pi}{a_y})$  [but  $A_y(k_x=0) \neq A_y(k_x=\frac{2\pi}{a_x})$ , since otherwise  $C_n$  always vanishes], so that

$$C_n = \frac{\Delta y_n}{a_y}, \quad A_x\left(k_y + \frac{2\pi}{a_y}\right) = A_x(k_y) \tag{B.127}$$

In this manner, the Chern number is equivalent to the change of the  $y$ -component of the center-of-mass position of the given Bloch state, when  $k_x$  changes by  $2\pi/a_x$ .

The above adiabatic pumping understanding of the Chern number can now be used to define the Chern number of Landau levels, for which the Hamiltonian can only be made translation invariant along one direction. The Landau level Hamiltonian for a uniform magnetic field  $B\hat{\mathbf{z}} = \nabla \times (Bx\hat{\mathbf{y}}) = \nabla \times \mathbf{A}$  is

$$H = \frac{p_x^2}{2m} + \frac{(p_y + eBx)^2}{2m} \tag{B.128}$$

Assuming the eigenfunctions are  $\psi(x, y)$ , we can first make use of the translation symmetry along  $y$  to define

$$\psi(x, y) = \frac{1}{2\pi} \int dk \phi(x, k) e^{iky} \quad (\text{B.129})$$

The inverse transform is

$$\psi(x, k) = \int dy \psi(x, y) e^{-iky} \quad (\text{B.130})$$

which is consistent with the direct transform since

$$\begin{aligned} \psi(x, k) &= \int dy \frac{1}{2\pi} \int dk' \phi(x, k') e^{i(k'-k)y} \\ &= \int dk' \phi(x, k') \delta(k' - k) = \phi(x, k) \end{aligned} \quad (\text{B.131})$$

Here we assume the wave functions are normalized as

$$\int d^2\mathbf{r} \psi^\dagger(x, y) \psi(x, y) = 1 \quad (\text{B.132})$$

which means

$$\begin{aligned} 1 &= \frac{1}{(2\pi)^2} \int d^2\mathbf{r} \int dk \int dk' \phi^\dagger(x, k) \phi(x, k') e^{i(k'-k)y} \\ &= \frac{1}{(2\pi)^2} \int dx \int dk \int dk' \phi^\dagger(x, k) \phi(x, k') 2\pi \delta(k' - k) \\ &= \frac{1}{2\pi} \int dx \int dk \phi^\dagger(x, k) \phi(x, k) \\ &= \int \frac{dk}{2\pi} \langle \phi(k) | \phi(k) \rangle \end{aligned} \quad (\text{B.133})$$

The  $k$ -dependent Hamiltonian is

$$\begin{aligned} H_k = e^{-iky} H e^{iky} &= \frac{p_x^2}{2m} + \frac{(\hbar k + eBx)^2}{2m} \\ &= \frac{p_x^2}{2m} + \frac{1}{2} m \left( \frac{eB}{m} \right)^2 \left( x + \frac{\hbar k}{eB} \right)^2 \end{aligned} \quad (\text{B.134})$$

which is a quantum harmonic oscillator with  $\omega = eB/m \equiv \omega_c$ . The eigensolutions are

$$\begin{aligned} H_k \phi_n(x, k) &= \hbar \omega \left( n + \frac{1}{2} \right) \phi_n(x, k), \\ \phi_n(x, k) &= \frac{1}{\sqrt{2^n n!}} \left( \frac{m\omega_c}{\hbar\pi} \right)^{\frac{1}{4}} e^{-\frac{m\omega_c(x-x_k)^2}{2\hbar}} H_n \left[ \sqrt{\frac{m\omega}{\hbar}} (x - x_k) \right] \end{aligned} \quad (\text{B.135})$$

where  $H_n$  are the Hermite polynomials and  $x_k \equiv -\frac{\hbar k}{eB}$ . However, the above  $\phi_n$  are normalized as

$$\int dx \phi_n^*(x, k) \phi_n(x, k) = 1 \quad (\text{B.136})$$

incompatible with our earlier definition in Eq. (B.133). To this end we choose a cutoff for the  $k$  integral and replace the normalization condition in Eq. (B.133) as

$$1 = \frac{1}{2\pi} \int_{-\frac{\pi}{a_y}}^{\frac{\pi}{a_y}} dk \langle \phi(k) | \phi(k) \rangle \quad (\text{B.137})$$

Since  $\phi_n(x, k)$  depends on  $k$  only through a shift of  $x$ , we have

$$\frac{1}{2\pi} \int_{-\frac{\pi}{a_y}}^{\frac{\pi}{a_y}} dk \langle \phi_n(k) | \phi_n(k) \rangle = \frac{1}{a_y} \langle \phi_n(k=0) | \phi_n(k=0) \rangle \equiv \frac{1}{a_y} \langle \phi_n | \phi_n \rangle = \frac{1}{a_y} \quad (\text{B.138})$$

This means that the  $\phi_n$  should be redefined so that Eq. (B.137) is satisfied:

$$\begin{aligned} \phi_n(x, k) &= \frac{\sqrt{a_y}}{\sqrt{2^n n!}} \left( \frac{m\omega_c}{\hbar\pi} \right)^{\frac{1}{4}} e^{-\frac{m\omega_c(x-x_k)^2}{2\hbar}} H_n \left[ \sqrt{\frac{m\omega}{\hbar}} (x - x_k) \right] \\ \langle \phi_n | \phi_n \rangle &= a_y \end{aligned} \quad (\text{B.139})$$

We can now try to use the above interpretation of the Chern number to check if Landau levels indeed have  $C = 1$ . To this end we would rewrite Eq. (B.126) assuming  $k$  as a pumping parameter. But this requires us to re-interpret Eq. (B.125)  $\mathbf{r}_n$  defined there is for Bloch waves with a different normalization condition from that in Eq. (B.137). Regarding  $|n\mathbf{k}\rangle$  as an eigenstate of the Hamiltonian playing the same role as  $|\phi_n\rangle$ , we have

$$\frac{a_x a_y}{(2\pi)^2} \int dk_x \int dk_y \langle n\mathbf{k} | n\mathbf{k} \rangle = \frac{a_x a_y}{(2\pi)^2} \int d^2\mathbf{k} \frac{(2\pi)^2}{a_x a_y} \delta(\mathbf{k}) = 1 \quad (\text{B.140})$$

In other words,

$$\frac{a_y}{2\pi} \int dk_y \langle n\mathbf{k} | \mathbf{r} | n\mathbf{k} \rangle = \frac{1}{N_y} \sum_{k_y} \langle n\mathbf{k} | \mathbf{r} | n\mathbf{k} \rangle \rightarrow \frac{1}{a_y} \langle \phi_n(k) | x | \phi_n(k) \rangle \equiv x_{nk} \quad (\text{B.141})$$

which corresponds to taking the expectation value of  $x$  in a given normalized eigenstate. Therefore Eq. (B.126) applicable to the present case should be

$$\begin{aligned} C_n &= -\frac{1}{2\pi} \int dk \partial_k \left( \frac{2\pi}{L_x} x_{nk} \right) \\ &= \frac{1}{L_x} \left( x_{nk=\frac{\pi}{a_y}} - x_{nk=-\frac{\pi}{a_y}} \right) \end{aligned} \quad (\text{B.142})$$

Due to the symmetry of  $\phi_n(x, k) = \langle x | \phi_n(k) \rangle = \phi_n(x - x_k, k = 0)$ , we have

$$\langle \phi_{nk} | x | \phi_{nk} \rangle = a_y x_k \quad (\text{B.143})$$

As a result

$$\begin{aligned} C_n &= \frac{1}{L_x} \frac{\hbar}{eB} \left( \frac{\pi}{a_y} + \frac{\pi}{a_y} \right) \\ &= \frac{\hbar}{e} \frac{1}{B a_y L_x} \equiv \frac{\Phi_0}{\Phi} N_y \end{aligned} \quad (\text{B.144})$$

where  $N_y \equiv L_y/a_y$ . However, this result is obtained by assuming that the period of  $k$  is  $2\pi/a_y$ . If one wraps the 2D system into a cylinder parallel to  $\hat{\mathbf{x}}$  so that  $k$  is quantized into

$$k = \frac{2\pi}{L_y} m \quad (\text{B.145})$$

where  $m$  can be any integer. Then imagining that one inserts a flux (or phase) through the cylinder defined by

$$\Phi_x \equiv \frac{e}{\hbar} A L_y \quad (\text{B.146})$$

so that  $\Phi_x$  enters the Landau level Hamiltonian as

$$H(\Phi_x) = \frac{p_x^2}{2m} + \frac{(p_y + \frac{\hbar}{L_y} \Phi_x + eBx)^2}{2m} \quad (\text{B.147})$$

Then apparently the Hamiltonian is symmetric under  $\Phi_x \rightarrow \Phi_x + 2\pi$ , so that  $\Phi_x$  can be viewed as a pumping parameter. In the above language, this is equivalent to choosing  $k$  as the pumping parameter but defining its period as

$$\frac{2\pi}{a_y} \rightarrow \frac{2\pi}{L_y} \quad (\text{B.148})$$

The Chern number is thus defined as

$$\begin{aligned} C_n &= -\frac{1}{2\pi} \oint d\Phi_x \partial_{\Phi_x} \left( \frac{2\pi}{L_x} x_{nk} \right) \\ &= \frac{1}{L_x} \left( x_{nk=\frac{2\pi}{L_y}} - x_{nk=0} \right) \\ &= \frac{\Phi_0}{\Phi} \end{aligned} \quad (\text{B.149})$$

The final result above is, however, not necessarily an integer. To see what is wrong with it, let us now use the above cylinder picture to understand what is really going on when the flux  $\Phi_x$



changes by  $2\pi$ . Since the cylinder has periodic boundary condition along  $y$ ,  $k$  is quantized as mentioned above, which restricts the eigenstates  $|\phi_n(k)\rangle$ . This further constrains the values of  $x_k$ , i.e., the center-of-mass of the wave functions  $\phi_n(x, k) = \langle x | \phi_n(k) \rangle$ :

$$\langle \phi_{nk} | x | \phi_{nk} \rangle = -\frac{2\pi m}{L_y} \frac{\hbar}{eB} = -\frac{\Phi_0}{BL_y} m \equiv -m\Delta x \quad (\text{B.150})$$

where we recover the original normalization of the Landau level wavefunctions Eq. (B.136). Note that from this we can also obtain the total number of electrons within a Landau level:

$$N = \frac{L_x}{\Delta x} = \frac{\Phi}{\Phi_0}. \quad (\text{B.151})$$

When  $\Phi_x$  changes by a period, which is equivalent to  $k$  changing by  $\frac{2\pi}{L_y}$  or  $m$  changes by 1, the center-of-mass of the Landau level wavefunction shifts along  $\hat{\mathbf{x}}$  for all  $k$  by the same quantity  $\Phi_0/(BL_y)$ , which is the same as their nearest neighbor spacing. Thus increasing  $\Phi_x$  by  $2\pi$  is equivalent to removing a Landau level wavefunction at the boundary of  $x = -L_x/2$  and adding another one at  $x = L_x/2$ . That one electron is transported from one edge to the other edge is the Chern number. However, Eq. (B.149) does not describe this integer directly. A modification that leads to the direct correspondence is to multiply Eq. (B.149) by the total number of electrons  $N$ :

$$\begin{aligned} C_n &= -\frac{N}{2\pi} \oint d\Phi_x \partial_{\Phi_x} \left( \frac{2\pi}{L_x} x_{nk}(\Phi_x) \right) \\ &= -\frac{1}{2\pi} \sum_k \oint d\Phi_x \partial_{\Phi_x} \left( \frac{2\pi}{L_x} x_{nk}(\Phi_x) \right) \\ &\equiv -\frac{1}{2\pi} \oint d\Phi_x \partial_{\Phi_x} \left( \frac{2\pi}{L_x} X_n(\Phi_x) \right) \\ &= \frac{1}{L_x} [X_n(2\pi) - X_n(0)] \end{aligned} \quad (\text{B.152})$$

where  $X_n \equiv \sum_k x_{nk}$  is the  $X$  coordinate of the center of mass of *all* electrons multiplied by the number of electrons within a Landau level. The above formula can be generally applied to other systems that has translation symmetry only along one direction.

More specifically, suppose we have a Hamiltonian  $H$  with eigenstates labeled by discrete band indices  $n$  and some other quantum numbers  $q$  characterizing the degenerate states within a band, and the eigenstates are simply normalized as  $\langle nq|nq \rangle = 1$ , then

$$X_n = \sum_q \langle nq|x|nq \rangle \quad (\text{B.153})$$

One can get  $C_n$  by diagonalizing the Hamiltonian so that  $H|nq \rangle = \epsilon_n|nq \rangle$ , adding the flux so that

$$H(\Phi_x)|nq(\Phi_x) \rangle = \epsilon_n(\Phi_x)|nq(\Phi_x) \rangle \quad (\text{B.154})$$

and making sure that  $\epsilon_n(\Phi_x)$  does not intersect with other bands as  $\Phi_x$  increases by  $2\pi$ . After that, calculate

$$X_n(\Phi_x = 2\pi) - X_n(\Phi_x = 0) \quad (\text{B.155})$$

and divide the above result by the finite length of the system along  $x$ . The result, if nonzero, means the system has a finite Chern number despite the absence of translation symmetry.

If, however, that  $\epsilon_n$  depends on  $q$  as well. Namely  $\epsilon_n \rightarrow \epsilon_n(q)$ , one can still define the Chern number by making sure that all eigenenergies  $\epsilon_{nq}(\Phi_x)$  do not touch other bands as  $\Phi_x$  increases by  $2\pi$ . The final step of calculating the Chern number stays unchanged.

# Bibliography

- [1] David J. Griffiths. *Introduction to Electrodynamics*. Cambridge University Press, Cambridge New York Port Melbourne New Delhi Singapore, fifth edition edition, 2024.
- [2] Alexander Altland and Ben Simons. *Condensed Matter Field Theory*. Cambridge University Press, Cambridge, United Kingdom ; New York, NY, third edition edition, 2023.
- [3] Charles Kittel. *Introduction to Solid State Physics*. Wiley, Hoboken, NJ, global edition, [9th edition] edition, 2018.
- [4] Xiangang Wan, Ari M. Turner, Ashvin Vishwanath, and Sergey Y. Savrasov. Topological semimetal and Fermi-arc surface states in the electronic structure of pyrochlore iridates. *Phys. Rev. B*, 83(20):205101, May 2011.
- [5] Su-Yang Xu, Ilya Belopolski, Nasser Alidoust, Madhab Neupane, Guang Bian, Chenglong Zhang, Raman Sankar, Guoqing Chang, Zhujun Yuan, Chi-Cheng Lee, Shin-Ming Huang, Hao Zheng, Jie Ma, Daniel S. Sanchez, BaoKai Wang, Arun Bansil, Fangcheng Chou, Pavel P. Shibayev, Hsin Lin, Shuang Jia, and M. Zahid Hasan. Discovery of a Weyl fermion semimetal and topological Fermi arcs. *Science*, 349(6248):613–617, August 2015.
- [6] Zhilin Li, Hongxiang Chen, Shifeng Jin, Di Gan, Wenjun Wang, Liwei Guo, and Xiaolong Chen. Weyl Semimetal TaAs: Crystal Growth, Morphology, and Thermodynamics. *Crystal Growth & Design*, 16(3):1172–1175, March 2016.
- [7] A. Yu Kitaev. Unpaired Majorana fermions in quantum wires. *Phys.-Usp.*, 44(10S):131, October 2001.
- [8] D. A. Ivanov. Non-Abelian Statistics of Half-Quantum Vortices in p -Wave Superconductors. *Phys. Rev. Lett.*, 86(2):268–271, January 2001.

- [9] Jason Alicea, Yuval Oreg, Gil Refael, Felix von Oppen, and Matthew P. A. Fisher. Non-Abelian statistics and topological quantum information processing in 1D wire networks. *Nature Phys*, 7(5):412–417, May 2011.
- [10] Jay D. Sau, Roman M. Lutchyn, Sumanta Tewari, and S. Das Sarma. Generic New Platform for Topological Quantum Computation Using Semiconductor Heterostructures. *Phys. Rev. Lett.*, 104(4):040502, January 2010.
- [11] A. Yu. Kitaev. Fault-tolerant quantum computation by anyons. *Annals of Physics*, 303(1):2–30, January 2003.
- [12] Chetan Nayak, Steven H. Simon, Ady Stern, Michael Freedman, and Sankar Das Sarma. Non-Abelian anyons and topological quantum computation. *Rev. Mod. Phys.*, 80(3):1083–1159, September 2008.
- [13] David Aasen, Michael Hell, Ryan V. Mishmash, Andrew Higginbotham, Jeroen Danon, Martin Leijnse, Thomas S. Jespersen, Joshua A. Folk, Charles M. Marcus, Karsten Flensberg, and Jason Alicea. Milestones Toward Majorana-Based Quantum Computing. *Phys. Rev. X*, 6(3):031016, August 2016.
- [14] N. Read and Dmitry Green. Paired states of fermions in two dimensions with breaking of parity and time-reversal symmetries and the fractional quantum Hall effect. *Phys. Rev. B*, 61(15):10267–10297, April 2000.
- [15] Jean-Pascal Brison. P-Wave Superconductivity and d-Vector Representation. In Hervé Bulou, Loïc Joly, Jean-Michel Mariot, and Fabrice Scheurer, editors, *Magnetism and Accelerator-Based Light Sources*, Springer Proceedings in Physics, pages 165–204, Cham, 2021. Springer International Publishing.
- [16] V. Mourik, K. Zuo, S. M. Frolov, S. R. Plissard, E. P. A. M. Bakkers, and L. P. Kouwenhoven. Signatures of Majorana Fermions in Hybrid Superconductor-Semiconductor Nanowire Devices. *Science*, 336(6084):1003–1007, May 2012.

- [17] Leonid P. Rokhinson, Xinyu Liu, and Jacek K. Furdyna. The fractional a.c. Josephson effect in a semiconductor–superconductor nanowire as a signature of Majorana particles. *Nature Phys*, 8(11):795–799, November 2012.
- [18] M. T. Deng, C. L. Yu, G. Y. Huang, M. Larsson, P. Caroff, and H. Q. Xu. Anomalous Zero-Bias Conductance Peak in a Nb–InSb Nanowire–Nb Hybrid Device. *Nano Lett.*, 12(12):6414–6419, December 2012.
- [19] T.-P. Choy, J. M. Edge, A. R. Akhmerov, and C. W. J. Beenakker. Majorana fermions emerging from magnetic nanoparticles on a superconductor without spin-orbit coupling. *Phys. Rev. B*, 84(19):195442, November 2011.
- [20] Bernd Braunecker and Pascal Simon. Interplay between Classical Magnetic Moments and Superconductivity in Quantum One-Dimensional Conductors: Toward a Self-Sustained Topological Majorana Phase. *Phys. Rev. Lett.*, 111(14):147202, October 2013.
- [21] Jelena Klinovaja, Peter Stano, Ali Yazdani, and Daniel Loss. Topological Superconductivity and Majorana Fermions in RKKY Systems. *Phys. Rev. Lett.*, 111(18):186805, November 2013.
- [22] S. Nadj-Perge, I. K. Drozdov, B. A. Bernevig, and Ali Yazdani. Proposal for realizing Majorana fermions in chains of magnetic atoms on a superconductor. *Phys. Rev. B*, 88(2):020407, July 2013.
- [23] Stevan Nadj-Perge, Ilya K. Drozdov, Jian Li, Hua Chen, Sangjun Jeon, Jungpil Seo, Allan H. MacDonald, B. Andrei Bernevig, and Ali Yazdani. Observation of Majorana fermions in ferromagnetic atomic chains on a superconductor. *Science*, 346(6209):602–607, October 2014.
- [24] Lucas Schneider, Philip Beck, Jannis Neuhaus-Steinmetz, Levente Rózsa, Thore Posske, Jens Wiebe, and Roland Wiesendanger. Precursors of Majorana modes and their length-

- dependent energy oscillations probed at both ends of atomic Shiba chains. *Nat. Nanotechnol.*, 17(4):384–389, April 2022.
- [25] Liang Fu and C. L. Kane. Superconducting proximity effect and Majorana fermions at the surface of a topological insulator. *Phys. Rev. Lett.*, 100(9):096407, March 2008.
  - [26] Pavan Hosur, Pouyan Ghaemi, Roger S. K. Mong, and Ashvin Vishwanath. Majorana Modes at the Ends of Superconductor Vortices in Doped Topological Insulators. *Phys. Rev. Lett.*, 107(9):097001, August 2011.
  - [27] Andrew C. Potter and Patrick A. Lee. Engineering a  $\mathbb{Z}_2$  superconductor: Comparison of topological insulator and Rashba spin-orbit-coupled materials. *Phys. Rev. B*, 83(18):184520, May 2011.
  - [28] M. Veldhorst, M. Snelder, M. Hoek, C. G. Molenaar, D. P. Leusink, A. A. Golubov, H. Hilgenkamp, and A. Brinkman. Magnetotransport and induced superconductivity in Bi based three-dimensional topological insulators. *physica status solidi (RRL) – Rapid Research Letters*, 7(1-2):26–38, 2013.
  - [29] Chui-Zhen Chen, Ying-Ming Xie, Jie Liu, Patrick A. Lee, and K. T. Law. Quasi-one-dimensional quantum anomalous Hall systems as new platforms for scalable topological quantum computation. *Phys. Rev. B*, 97(10):104504, March 2018.
  - [30] Yongxin Zeng, Chao Lei, Gaurav Chaudhary, and Allan H. MacDonald. Quantum anomalous Hall Majorana platform. *Phys. Rev. B*, 97(8):081102, February 2018.
  - [31] Ying-Ming Xie, Xue-Jian Gao, Tai-Kai Ng, and K. T. Law. Creating Localized Majorana Zero Modes in Quantum Anomalous Hall Insulator/Superconductor Heterostructures with a Scissor, June 2021.
  - [32] Yuval Oreg, Gil Refael, and Felix von Oppen. Helical Liquids and Majorana Bound States in Quantum Wires. *Phys. Rev. Lett.*, 105(17):177002, October 2010.

- [33] Roman M. Lutchyn, Tudor D. Stanescu, and S. Das Sarma. Search for Majorana Fermions in Multiband Semiconducting Nanowires. *Phys. Rev. Lett.*, 106(12):127001, March 2011.
- [34] Andrew C. Potter and Patrick A. Lee. Topological superconductivity and Majorana fermions in metallic surface states. *Phys. Rev. B*, 85(9):094516, March 2012.
- [35] Jian Li, Titus Neupert, Zhijun Wang, A. H. MacDonald, A. Yazdani, and B. Andrei Bernevig. Two-dimensional chiral topological superconductivity in Shiba lattices. *Nat Commun*, 7(1):12297, July 2016.
- [36] Chao Lei, Hua Chen, and Allan H. MacDonald. Ultrathin Films of Superconducting Metals as a Platform for Topological Superconductivity. *Phys. Rev. Lett.*, 121(22):227701, November 2018.
- [37] Annica M. Black-Schaffer and Jacob Linder. Majorana fermions in spin-orbit-coupled ferromagnetic Josephson junctions. *Phys. Rev. B*, 84(18):180509, November 2011.
- [38] Falko Pientka, Alessandro Romito, Mathias Duckheim, Yuval Oreg, and Felix von Oppen. Signatures of topological phase transitions in mesoscopic superconducting rings. *New J. Phys.*, 15(2):025001, February 2013.
- [39] Michael Hell, Martin Leijnse, and Karsten Flensberg. Two-Dimensional Platform for Networks of Majorana Bound States. *Phys. Rev. Lett.*, 118(10):107701, March 2017.
- [40] Antonio Fornieri, Alexander M. Whiticar, F. Setiawan, Elías Portolés, Asbjørn C. C. Drachmann, Anna Keselman, Sergei Gronin, Candice Thomas, Tian Wang, Ray Kallagher, Geoffrey C. Gardner, Erez Berg, Michael J. Manfra, Ady Stern, Charles M. Marcus, and Fabrizio Nichele. Evidence of topological superconductivity in planar Josephson junctions. *Nature*, 569(7754):89–92, May 2019.
- [41] Hechen Ren, Falko Pientka, Sean Hart, Andrew T. Pierce, Michael Kosowsky, Lukas Lunczer, Raimund Schlereth, Benedikt Scharf, Ewelina M. Hankiewicz, Laurens W.

- Molenkamp, Bertrand I. Halperin, and Amir Yacoby. Topological superconductivity in a phase-controlled Josephson junction. *Nature*, 569(7754):93–98, May 2019.
- [42] Benedikt Scharf, Falko Pientka, Hechen Ren, Amir Yacoby, and Ewelina M. Hankiewicz. Tuning topological superconductivity in phase-controlled Josephson junctions with Rashba and Dresselhaus spin-orbit coupling. *Phys. Rev. B*, 99(21):214503, June 2019.
- [43] Tong Zhou, Matthieu C. Dartiailh, William Mayer, Jong E. Han, Alex Matos-Abiague, Javad Shabani, and Igor Žutić. Phase Control of Majorana Bound States in a Topological  $\mathsf{X}$  Junction. *Phys. Rev. Lett.*, 124(13):137001, April 2020.
- [44] Jin-Peng Xu, Mei-Xiao Wang, Zhi Long Liu, Jian-Feng Ge, Xiaojun Yang, Canhua Liu, Zhu An Xu, Dandan Guan, Chun Lei Gao, Dong Qian, Ying Liu, Qiang-Hua Wang, Fu-Chun Zhang, Qi-Kun Xue, and Jin-Feng Jia. Experimental Detection of a Majorana Mode in the core of a Magnetic Vortex inside a Topological Insulator-Superconductor  $\text{Bi}_2\text{Te}_3$  /  $\text{NbSe}_2$  Heterostructure. *Phys. Rev. Lett.*, 114(1):017001, January 2015.
- [45] S. M. Albrecht, A. P. Higginbotham, M. Madsen, F. Kuemmeth, T. S. Jespersen, J. Nygård, P. Krogstrup, and C. M. Marcus. Exponential protection of zero modes in Majorana islands. *Nature*, 531(7593):206–209, March 2016.
- [46] Hao-Hua Sun, Kai-Wen Zhang, Lun-Hui Hu, Chuang Li, Guan-Yong Wang, Hai-Yang Ma, Zhu-An Xu, Chun-Lei Gao, Dan-Dan Guan, Yao-Yi Li, Canhua Liu, Dong Qian, Yi Zhou, Liang Fu, Shao-Chun Li, Fu-Chun Zhang, and Jin-Feng Jia. Majorana Zero Mode Detected with Spin Selective Andreev Reflection in the Vortex of a Topological Superconductor. *Phys. Rev. Lett.*, 116(25):257003, June 2016.
- [47] Dongfei Wang, Lingyuan Kong, Peng Fan, Hui Chen, Shiyu Zhu, Wen Yao Liu, Lu Cao, Yujie Sun, Shixuan Du, John Schneeloch, Ruidan Zhong, Genda Gu, Liang Fu, Hong Ding, and Hong-Jun Gao. Evidence for Majorana bound states in an iron-based superconductor. *Science*, 362(6412):333–335, October 2018.



- [48] Berthold Jäck, Yonglong Xie, Jian Li, Sangjun Jeon, B. Andrei Bernevig, and Ali Yazdani. Observation of a Majorana zero mode in a topologically protected edge channel. *Science*, 364(6447):1255–1259, June 2019.
- [49] Sujit Manna, Peng Wei, Yingming Xie, Kam Tuen Law, Patrick A. Lee, and Jagadeesh S. Moodera. Signature of a pair of Majorana zero modes in superconducting gold surface states. *Proceedings of the National Academy of Sciences*, 117(16):8775–8782, April 2020.
- [50] Geoffrey L. Fatin, Alex Matos-Abiague, Benedikt Scharf, and Igor Žutić. Wireless Majorana Bound States: From Magnetic Tunability to Braiding. *Phys. Rev. Lett.*, 117(7):077002, August 2016.
- [51] Jay D. Sau and S. Das Sarma. Realizing a robust practical Majorana chain in a quantum-dot-superconductor linear array. *Nat Commun*, 3(1):964, July 2012.
- [52] Martin Leijnse and Karsten Flensberg. Parity qubits and poor man’s Majorana bound states in double quantum dots. *Phys. Rev. B*, 86(13):134528, October 2012.
- [53] Tom Dvir, Guanzhong Wang, Nick van Loo, Chun-Xiao Liu, Grzegorz P. Mazur, Alberto Bordin, Sebastiaan L. D. ten Haaf, Ji-Yin Wang, David van Driel, Francesco Zatelli, Xiang Li, Filip K. Malinowski, Sasa Gazibegovic, Ghada Badawy, Erik P. A. M. Bakkers, Michael Wimmer, and Leo P. Kouwenhoven. Realization of a minimal Kitaev chain in coupled quantum dots. *Nature*, 614(7948):445–450, February 2023.
- [54] Torsten Karzig, Christina Knapp, Roman M. Lutchyn, Parsa Bonderson, Matthew B. Hastings, Chetan Nayak, Jason Alicea, Karsten Flensberg, Stephan Plugge, Yuval Oreg, Charles M. Marcus, and Michael H. Freedman. Scalable designs for quasiparticle-poisoning-protected topological quantum computation with Majorana zero modes. *Phys. Rev. B*, 95(23):235305, June 2017.

- [55] Andrew C. Potter and Patrick A. Lee. Multichannel Generalization of Kitaev's Majorana End States and a Practical Route to Realize Them in Thin Films. *Phys. Rev. Lett.*, 105(22):227003, November 2010.
- [56] Jian Li, Titus Neupert, B. Andrei Bernevig, and Ali Yazdani. Manipulating Majorana zero modes on atomic rings with an external magnetic field. *Nat Commun*, 7(1):10395, January 2016.
- [57] Tudor E. Pahomi, Manfred Sigrist, and Alexey A. Soluyanov. Braiding Majorana corner modes in a second-order topological superconductor. *Phys. Rev. Res.*, 2(3):032068, September 2020.
- [58] Song-Bo Zhang, Alessio Calzona, and Björn Trauzettel. All-electrically tunable networks of Majorana bound states. *Phys. Rev. B*, 102(10):100503, September 2020.
- [59] Song-Bo Zhang, W. B. Rui, Alessio Calzona, Sang-Jun Choi, Andreas P. Schnyder, and Björn Trauzettel. Topological and holonomic quantum computation based on second-order topological superconductors. *Phys. Rev. Res.*, 2(4):043025, October 2020.
- [60] O. Pietzsch, S. Okatov, A. Kubetzka, M. Bode, S. Heinze, A. Lichtenstein, and R. Wiesendanger. Spin-Resolved Electronic Structure of Nanoscale Cobalt Islands on Cu(111). *Phys. Rev. Lett.*, 96(23):237203, June 2006.
- [61] Alessandro Romito, Jason Alicea, Gil Refael, and Felix von Oppen. Manipulating Majorana fermions using supercurrents. *Phys. Rev. B*, 85(2):020502, January 2012.
- [62] Kazuaki Takasan, Shuntaro Sumita, and Youichi Yanase. Supercurrent-induced topological phase transitions. *Phys. Rev. B*, 106(1):014508, July 2022.
- [63] T. Hyart, B. van Heck, I. C. Fulga, M. Burrello, A. R. Akhmerov, and C. W. J. Beenakker. Flux-controlled quantum computation with Majorana fermions. *Phys. Rev. B*, 88(3):035121, July 2013.

- [64] Olesia Dmytruk, Manisha Thakurathi, Daniel Loss, and Jelena Klinovaja. Majorana bound states in double nanowires with reduced Zeeman thresholds due to supercurrents. *Phys. Rev. B*, 99(24):245416, June 2019.
- [65] P. G. De Gennes. *Superconductivity Of Metals And Alloys*. CRC Press, Boca Raton, March 2018.
- [66] *See Supplemental Material in Chapter 2 of this dissertation for additional technical details.*
- [67] Guan-Hao Feng and Hong-Hao Zhang. Probing robust Majorana signatures by crossed Andreev reflection with a quantum dot. *Phys. Rev. B*, 105(3):035148, January 2022.
- [68] Bradraj Pandey, Nitin Kaushal, Gonzalo Alvarez, and Elbio Dagotto. Majorana zero modes in Y-shape interacting Kitaev wires. *npj Quantum Mater.*, 8(1):1–8, September 2023.
- [69] Jian Li, Hua Chen, Ilya K. Drozdov, A. Yazdani, B. Andrei Bernevig, and A. H. MacDonald. Topological superconductivity induced by ferromagnetic metal chains. *Phys. Rev. B*, 90(23):235433, December 2014.
- [70] Ryan V. Mishmash, Bela Bauer, Felix von Oppen, and Jason Alicea. Dephasing and leakage dynamics of noisy Majorana-based qubits: Topological versus Andreev. *Phys. Rev. B*, 101(7):075404, February 2020.
- [71] Gábor Széchenyi and András Pályi. Parity-to-charge conversion for readout of topological majorana qubits. *Phys. Rev. B*, 101:235441, Jun 2020.
- [72] K. v. Klitzing, G. Dorda, and M. Pepper. New method for high-accuracy determination of the fine-structure constant based on quantized hall resistance. *Phys. Rev. Lett.*, 45(6):494–497, August 1980.
- [73] A. H. Castro Neto, F. Guinea, N. M. R. Peres, K. S. Novoselov, and A. K. Geim. The electronic properties of graphene. *Rev. Mod. Phys.*, 81(1):109–162, January 2009.

- [74] K. S. Novoselov, A. K. Geim, S. V. Morozov, D. Jiang, M. I. Katsnelson, I. V. Grigorieva, Dubonos S. V., and A. A. Firsov. Two-dimensional gas of massless Dirac fermions in graphene. *Nature Physics*, 438:197, 2005.
- [75] Yuanbo Zhang, Yan-Wen Tan, Horst L. Stormer, and Philip Kim. Experimental observation of the quantum Hall effect and Berry’s phase in graphene. *Nature Physics*, 438:201, 2005.
- [76] Netanel H. Lindner, Gil Refael, and Victor Galitski. Floquet topological insulator in semiconductor quantum wells. *Nature Physics*, 7:490, 2011.
- [77] André Eckardt and Egidijus Anisimovas. High-frequency approximation for periodically driven quantum systems from a Floquet-space perspective. *New J. Phys.*, 17:093039, 2015.
- [78] Mikael C. Rechtsman, Julia M. Zeuner, Yonatan Plotnik, Yaakov Lumer, Daniel Podolsky, Felix Dreisow, Stefan Nolte, Mordechai Segev, and Alexander Szameit. Photonic floquet topological insulators. *Nature Physics*, 496:196, 2013.
- [79] Y. H. Wang, H. Steinberg, P. Jarillo-Herrero, and N. Gedik. Observation of floquet-bloch states on the surface of a topological insulator. *Science*, 342(6157):453–457, 2013.
- [80] Hongbin Zhang, Jiandong Yao, Jianmei Shao, Hai Li, Shuwei Li, Dinghua Bao, Chengxin Wang, and Guowei Yang. Anomalous photoelectric effect of a polycrystalline topological insulator film. *Scientific Reports*, 4:5876, 2014.
- [81] J. W. McIver, B. Schulte, F.-U. Stein, T. Matsuyama, G. Jotzu, G. Meier, and A. Cavalleri. Light-induced anomalous Hall effect in graphene. *Nature Physics*, 11:123, 2019.
- [82] Marco Merboldt, Michael Schüler, David Schmitt, Jan Philipp Bange, Wiebke Bennecke, Karun Gadge, Klaus Pierz, Hans Werner Schumacher, Davood Momeni, Daniel Steil, Salvatore R. Manmana, Michael Sentef, Marcel Reutz, and Stefan Mathias. Observation of Floquet states in graphene, April 2024.

- [83] Dongsung Choi, Masataka Mogi, Umberto De Giovannini, Doron Azoury, Baiqing Lv, Yifan Su, Hannes Hübener, Angel Rubio, and Nuh Gedik. Direct observation of Floquet-Bloch states in monolayer graphene, April 2024.
- [84] Jon H. Shirley. Solution of the schrödinger equation with a hamiltonian periodic in time. *Phys. Rev.*, 138(4B):B979–B987, May 1965.
- [85] Hideo Sambe. Steady states and quasienergies of a quantum-mechanical system in an oscillating field. *Phys. Rev. A*, 7(6):2203–2213, June 1973.
- [86] Milena Grifoni and Peter Hänggi. Driven quantum tunneling. *Physics Reports*, 304:229, 1998.
- [87] M. Bukov, L. D’Alessio, and A. Polkovnikov. Universal high-frequency behavior of periodically driven systems: From dynamical stabilization to Floquet engineering. *Advances in Physics*, 64:139, 2015.
- [88] N. Goldman and J. Dalibard. Periodically driven quantum systems: Effective hamiltonians and engineered gauge fields. *Phys. Rev. X*, 4(3):031027, August 2014.
- [89] Saar Rahav, Ido Gilary, and Shmuel Fishman. Effective Hamiltonians for periodically driven systems. *Phys. Rev. A*, 68(1):013820, July 2003.
- [90] A. P. Itin and M. I. Katsnelson. Effective hamiltonians for rapidly driven many-body lattice systems: Induced exchange interactions and density-dependent hoppings. *Phys. Rev. Lett.*, 115(7):075301, August 2015.
- [91] Takahiro Mikami, Sota Kitamura, Kenji Yasuda, Naoto Tsuji, Takashi Oka, and Hideo Aoki. Brillouin-Wigner theory for high-frequency expansion in periodically driven systems: Application to Floquet topological insulators. *Phys. Rev. B*, 93(14):144307, April 2016.

- [92] E. S. Mananga and T. Charpentier. Introduction of the Floquet-Magnus expansion in solid-state nuclear magnetic resonance spectroscopy. *The Journal of Chemical Physics*, 135:044109, 2011.
- [93] T. Kuwahara, T. Mori, and K. Saito. Floquet–Magnus theory and generic transient dynamics in periodically driven many-body quantum systems. *Annals of Physics*, 367:96, 2016.
- [94] A. López, A. Scholz, Z. Z. Sun, and J. Schliemann. Graphene with time-dependent spin-orbit coupling: Truncated Magnus expansion approach. *Eur. Phys. J. B*, 86:366, 2013.
- [95] F. Casas, J. A. Oteo, and J. Ros. Floquet theory: Exponential perturbative treatment. *J. Phys. A*, 34:3379, 2001.
- [96] Takuya Kitagawa, Takashi Oka, Arne Brataas, Liang Fu, and Eugene Demler. Transport properties of nonequilibrium systems under the application of light: Photoinduced quantum Hall insulators without Landau levels. *Phys. Rev. B*, 84(23):235108, December 2011.
- [97] Andrei Kirilyuk, Alexey V. Kimel, and Theo Rasing. Ultrafast optical manipulation of magnetic order. *Rev. Mod. Phys.*, 82(3):2731–2784, September 2010.
- [98] J. H. Mentink, K. Balzer, and M. Eckstein. Ultrafast and reversible control of the exchange interaction in Mott insulators. *Nature Communications*, 6:6708, 2015.
- [99] L. Stojchevska, I. Vaskivskyi, T. Mertelj, P. Kusar, D. Svetin, S. Brazovskii, and D. Mihailovic. Ultrafast switching to a stable hidden quantum state in an electronic crystal. *Science*, 344(6180):177–180, 2014.
- [100] Adolfo G. Grushin, Álvaro Gómez-León, and Titus Neupert. Floquet fractional chern insulators. *Phys. Rev. Lett.*, 112(15):156801, April 2014.

- [101] Mark S. Rudner and Netanel H. Lindner. Band structure engineering and non-equilibrium dynamics in Floquet topological insulators. *Nat Rev Phys*, 2(5):229–244, May 2020.
- [102] Nina Bielinski, Rajas Chari, Julian May-Mann, Soyeun Kim, Jack Zwettler, Yujun Deng, Anuva Aishwarya, Subhjit Roychowdhury, Chandra Shekhar, Makoto Hashimoto, Donghui Lu, Jiaqiang Yan, Claudia Felser, Vidya Madhavan, Zhi-Xun Shen, Taylor L. Hughes, and Fahad Mahmood. Floquet–Bloch manipulation of the Dirac gap in a topological antiferromagnet. *Nat. Phys.*, pages 1–6, January 2025.
- [103] Ervand Kandelaki and Mark S. Rudner. Many-body dynamics and gap opening in interacting periodically driven systems. *Phys. Rev. Lett.*, 121(3):036801, July 2018.
- [104] G. Juzeliūnas and P. Öhberg. Slow light in degenerate fermi gases. *Phys. Rev. Lett.*, 93(3):033602, July 2004.
- [105] J. Ruseckas, G. Juzeliūnas, P. Öhberg, and M. Fleischhauer. Non-abelian gauge potentials for ultracold atoms with degenerate dark states. *Phys. Rev. Lett.*, 95(1):010404, June 2005.
- [106] Shi-Liang Zhu, Hao Fu, C.-J. Wu, S.-C. Zhang, and L.-M. Duan. Spin hall effects for cold atoms in a light-induced gauge potential. *Phys. Rev. Lett.*, 97(24):240401, December 2006.
- [107] Jean Dalibard, Fabrice Gerbier, Gediminas Juzeliūnas, and Patrik Öhberg. Colloquium: Artificial gauge potentials for neutral atoms. *Rev. Mod. Phys.*, 83(4):1523–1543, November 2011.
- [108] N Goldman, G Juzeliūnas, P Öhberg, and I B Spielman. Light-induced gauge fields for ultracold atoms. *Reports on Progress in Physics*, 77(12):126401, November 2014.
- [109] Hyunki Shim, Francesco Monticone, and Owen D. Miller. Fundamental Limits to the Refractive Index of Transparent Optical Materials. *Advanced Materials*, 33(43):2103946, 2021.

- [110] Tatiana Amotchkina, Michael Trubetskov, Daniel Hahner, and Vladimir Pervak. Characterization of e-beam evaporated Ge, YbF<sub>3</sub>, ZnS, and LaF<sub>3</sub> thin films for laser-oriented coatings. *Appl Opt*, 59(5):A40–A47, February 2020.